HOKKAIDO UNIVERSITY

Title	Development of Multimetallic Alloy Catalysts Efficient for CO2 utilization by Dry Reforming of Hydrocarbons
Author(s)	劉, 可
Citation	北海道大学. 博士(工学) 甲第15683号
Issue Date	2023-12-25
DOI	10.14943/doctoral.k15683
Doc URL	http://hdl.handle.net/2115/91203
Type	theses (doctoral)
File Information	Ke_Liu.pdf

Instructions for use

Hokkaido University Collection of Scholarly and Academic Papers : HUSCAP

Development of Multimetallic Alloy Catalysts Efficient for CO_2 utilization by Dry Reforming of Hydrocarbons

(炭化水素のドライリフォーミングによる

CO_2利用に有効な多元素合金触媒の開発)

LIU KE

Graduate School of Chemical Sciences and Engineering

Hokkaido University

2023

Contents

Chapter 1. General Introduction

1.1 Recent developments in CO_2 utilization 2

1.2 CO_2 reforming of hydrocarbon 9

1.3 CO_2 reforming over metallic catalysts 12

1.3.1 CO_2 reforming of methane 12

1.3.2 CO_2 reforming of benzene 13

1.4 Aim of this thesis 15

1.5 Outline of thesis 17

1.6 Concluding remarks 18

References 19

Chapter 2. Development of a Highly Stable Ternary Alloy Catalyst for CO_2 Reforming of Methane

2.1 Introduction 31

2.2 Experimental Section 33

2.3 Results and Discussion 38

2.3.1 Characterization of the catalysts structure 38

2.3.2 Catalytic performance 44

2.3.3 The origin of the coke resistance of $(Ni_{0.5}Co_{0.5})_3Ge/SiO_2$ in DRM 60

2.3.4 DFT calculation 63

2.4 Conclusion 68

References 69

Chapter 3. Enhanced CO_2 Utilization in Dry reforming of Benzene over Intermetallic Ni_3Ga Catalyst

3.1 Introduction 82

3.2 Experimental Section 84

3.3 Results and Discussion 88

3.3.1 Characterization of the catalysts structure 88

3.3.2 Catalytic performance in DRB 93

3.4 Conclusion 100

References 101

Chapter 4. General Conclusion 105

Acknowledgements 107

Chapter 1

General Introduction

1. General Introduction

1.1 Recent developments in CO_2 utilization

The extensive emission of CO_2 poses a major threat to humanity, the well-known situation was intensified the greenhouse effect, causing rising seas, melting glacier and ocean acidification. This has aroused human concern about the change in the ecological environment.[1] Besides, the current situation of dwindling fossil fuels has compelled people to seek corresponding alternatives. In this context, the chemical utilization of CO_2 as an abundant and nontoxic C1 block offers an effective solution to the aforementioned two issues, which is the reason why CO_2 utilization has garnered immense global attention. [2-3] Many techniques, such as thermal chemical, photo-chemical, biochemical, electrochemical, have been utilized for CO_2 utilization to convert CO_2 into useful chemicals including syngas, methanol, and formic acid, food and beverages and CO_2 enhanced oil recovery etc..[4-6]

1.1.1 Chemicals

The use of CO_2 to synthesize chemicals is a promising way to enhance the economic value of CO_2 and relieve energy crisis. The conversion of CO_2 to methanol is of particular importance because methanol could be used not only as a sustainable source of liquid fuel but also as a reactant to produce formaldehyde, olefins, dimethyl ether, and acetic acid. The equation of methanol synthesis from CO_2 as illustrated below (Equation (1)), while the reverse water gas shift reaction also occurs as side reaction (RWGS: Equation (2)), resulting in lower methanol yield. Hence, in order to enhance the methanol yield, a wide number of explorations have recently been carried out.

$$CO_2 + 3H_2 \rightarrow CH_3OH + H_2O \qquad \Delta H_{298K} = -49.5kJ \cdot mol^{-1} \qquad (1)$$

$$CO_2 + H_2 \rightarrow CO + H_2O \qquad \Delta H_{298K} = -41.2kJ \cdot mol^{-1} \qquad (2)$$

Cu based catalyst is the most studied catalyst among many kinds of metal-based catalysts. Some representative Cu-based and other metal catalysts for the synthesis of methanol by CO_2 hydrogenation are summarized in Table 1.1. Industrially, the ternary $Cu/ZnO/Al_2O_3$ catalyst used in methanol synthesis from syngas (CO/H_2) and also from CO_2 hydrogenation.[7] However, Cu nanoparticles is prone to aggregation and separate from ZnOx under reaction conditions, which is benefit to the reverse water gas reaction,

Table 1.1 some representative catalysts for the synthesis of methanol by the hydrogenation of CO_2.[8]

Catalyst	Preparation method	T/°C	CO_2 conversion (%)	Methanol selectivity (%)	Methanol activity (mol kg^{-1} cat. h)	Ref.
$Cu/Zn/Ga/SiO_2$	co-impregnation	270	5.6	99.5	10.9	[9]
Cu/Ga/ZnO	co-impregnation	270	6.0	88.0	11.8	[10]
Cu/ZrO_2	precipitation	240	6.3	48.8	11.2	[11]
$Cu/Ga/ZrO_2$	precipitation	250	13.7	75.5	1.9	[12]
$Cu/B/ZrO_2$	precipitation	250	15.8	67.2	1.8	[12]
$Cu/Zn/Ga/ZrO_2$	coprecipitation	250	n/a	75.0	10.1	[13]
$Cu/Zn/ZrO_2$	coprecipitation	250	19.4	29.3	n/a	[14]
$Cu/Zn/ZrO_2$	Urea-nitrate combustion	240	17.0	56.2	n/a	[15]
$Cu/Zn/ZrO_2$	coprecipitation	220	21.0	68.0	5.6	[16]
$Cu/Zn/ZrO_2$	glycine-nitrate combustion	220	12.0	71.1	n/a	[17]
$Cu/Zn/Al/ZrO_2$	coprecipitation	240	18.7	47.2	n/a	[18]
$Ag/Zn/ZrO_2$	coprecipitation	220	2.0	97.0	0.46	[16]
$Au/Zn/ZrO_2$	coprecipitation	220	1.5	100	0.40	[16]
$Pd/Zn/ZrO_2$	incipient wetness	250	6.3	99.6	1.1	[19]
Ga_2O_3-Pd/ZrO_2	incipient wetness	250	n/a	70.0	7.9	[20]
n/a: not available					n/a	

diminishing the methanol yield over time.[21] Li *et al.* developed Cu/ZrO_2 catalyst for CO_2 hydrogenation to methanol. It was found that the unique crystal structure of ZrO_2 induced it interact with Cu, which improved the dispersion of Cu, stabilized Cu NPs during catalytic CO_2 hydrogenation, effectively inhibited the RWGS reaction, and promoted the methanol production.[22] An *et al.* introduced MOFs to Cu/ZrO_2 and Cu/ZnO with strong metal-support catalysts for CO_2 hydrogenation. This novel catalyst confines the agglomeration of Cu NPs and phase separation between Cu and ZnOx through utilized the porous structure of MOF, which creating a specific environment for reaction proceed, effectively enhanced methanol selectivity of 100% and high stability over 100 h. [23] Similarly, Qi *et al*. obtained superior methanol selectivity through introduced a bimetallic MOF template to $Cu\text{-}ZnO/Al_2O_3$ catalyst, in which Cu NPs have higher dispersibility, thereby inhibiting the RWGS reaction.[24] In addition to Cu-based catalysts, several other materials exhibit activity in CO_2 hydrogenation. Such as, Pd/ZnO catalyst loaded on multi-walled carbon nanotubes exhibit excellent performance for the formation of methanol due to an increasing concentration of active Pd^0 species.[19] Studt. *et al.* reported a Ni_5Ga_3 catalyst that reduces CO_2 to methanol at ambient pressure, which showed the same or better methanol synthesis activity, as well as considerably lower production of CO compare to the traditional $Cu/ZnO/Al_2O_3$ catalyst.[25] Besides, Ag- and Au-based catalysts offer superior selectivity of methanol with high content of metal.[26]

Another important chemical is formic acid, which is widely used in many fields, such as the leather and rubber industries.[27] Formic acid has also been considered as hydrogen storage material by combining CO_2 hydrogenation with selective formic acid decomposition. The reaction formula for the CO_2 hydrogenation to formic acid is as shown in Equation (3). Currently, homogeneous catalysts are the most studied catalysts

for this reaction because homogeneous catalytic systems have milder conditions and higher catalytic efficiency. The homogeneous catalytic reaction mechanism of CO_2 hydrogenation to formic acid as shown in Figure 1.1.[28]

$$CO_2 + H_2 \rightarrow HCOOH \qquad (3)$$

Wilkinson catalyst, $RhCl(PPh_3)_3$ was first introduced by Inoue et al. in 1976 for CO_2 hydrogenation.[29] Then, Ezhova *et al.* studied this complex in more details, suggesting that formic acid was formed in the presence of rhodium complexes with a phosphine ligand. Reduction of the complex to metallic rhodium is inhibited by excess PPh_3, which increases the yield of formic acid significantly.[30] Ru complexes have garnered significant attention, it generally offer favorable activity and selectivity for formic acid. Tai *et al.* found that there is no correlation between the basicity of monophosphines (PR_3) and the activity of the catalysts after comparing the Ru catalysts with total of 44 different phosphines or other ligands. Interestingly, a quite unique interplay of electronic and bite angle effects was observed. Diphosphines with weak basicity exhibit highly active catalysts when their bite angles are small, significantly enhancing the formic acid yield. Conversely, diphosphine with stronger basicity demonstrated the opposite trend.[31]

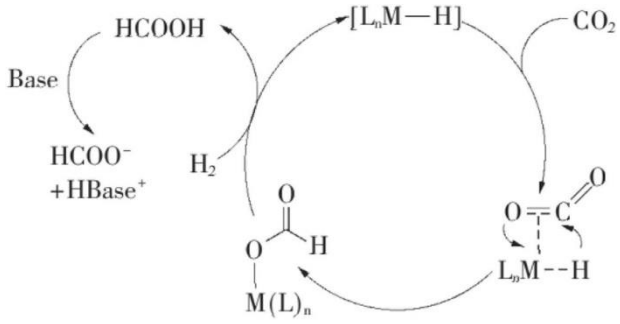

Figure 1.1 Homogeneous catalytic reaction mechanism of CO_2 hydrogenation to formic acid.[28]

Syngas, also known as synthesis gas, is another chemical that can be derived from CO_2. Syngas consists of carbon monoxide (CO), CO_2, and H_2, and its applications across various industrial sectors, including fuels, synthetic materials, solvents, and minerals.[32] CO_2 reforming represents one method for generating syngas by reacting CO_2 with hydrocarbons. Dry reforming of methane stands out as one of most classic examples, it is a highly endothermic process that requires a high operating temperature. In this context, developing a new hybrid catalyst capable of effectively resisting metal sintering caused by high temperature and enhancing activity is necessary. Ni-based catalysts has been widely studied in this reaction although its susceptibility to sintering at high temperature, virous methods have been conducted to modify the Ni-based catalysts, such as, alloying, controlling the Ni particle size by modifying the synthesis method and changing the type of support etc..[33-39] The details of dry reforming of methane will be discussed in the section 1.2 and 1.3.1.

1.1.2 Enhanced oil recovery

Underneath the Earth's surface, oil and gases are enclosed by a substantial insulating layer of shale or caprock, spanning hundreds of feet. This natural barrier functions as a protective shield, preventing the ascent of fluids and gases to the surface. This also complicates the extraction of oil.[1] CO_2 enhanced oil recovery (EOR) is a widely recognized technology that has been successfully applied to extract oil from resevoirs.[40] The cycle of CO_2-enhanced oil recovery (CO_2-EOR) and the flow of CO_2 within the cycle as illustrated in Figure 1.2. CO_2-EOR involves injecting pressurized CO_2 into oil reservoirs, displacing oil and improving its flow. This mixture is extracted at production wells, separating oil and CO_2. The captured CO_2 is recirculated for reinjection, maintaining pressure and facilitating continuous oil recovery. This process enhances oil

production and has environmental benefits by utilizing and reusing CO_2.[40] Currently, two significant endeavors employing CO_2-enhanced oil recovery are being executed in offshore oil fields: Sleipner and Snøhvit, both situated in Norway. Similarly, in the United States, prior pilot projects have been undertaken to employ CO_2-enhanced oil recovery within the Gulf of Mexico.[6] Currently, the industry facing several challenges in implementing EOR, like the non-uniform rock formation, diminishing the efficacy of CO_2 flooding. However, CO_2 EOR remains a promising method for enhanced oil and gas recovery, applicable across diverse reservoirs.[41]

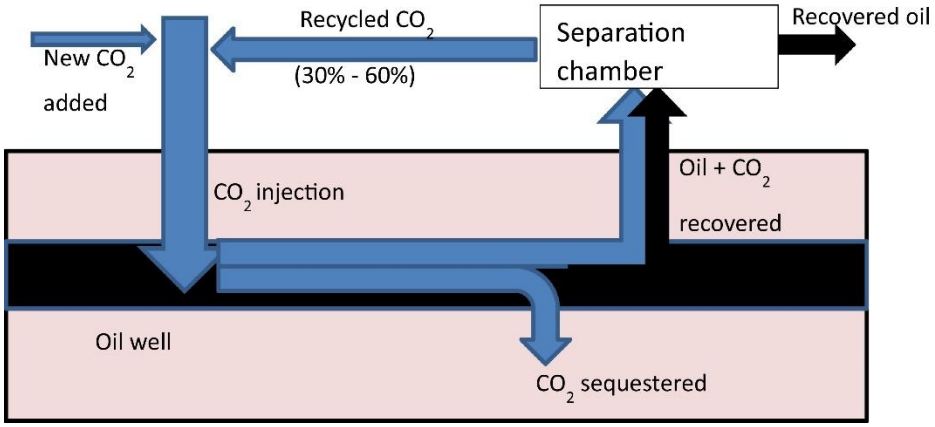

Figure 1.2 Overview of the CO_2-EOR (enhanced oil recovery) cycle.[6]

1.1.3 Food and Beverages

The food industry continually seeks advanced extraction technologies to obtain pure natural products and produce healthy, high-quality items applicable in various industries. Regrettably, modern extraction methods employing toxic and unsafe solvents face significant limitations.[8] Supercritical fluid extraction is a relatively new and promising technology for the "clean" extraction method. CO_2 is a great candidate for food extraction as a supercritical fluid because of its unique properties such as the low critical temperature of 31.06°C, the low critical pressure of 73.83 bar, and its critical density of 0.460 g/cm.[42] A diverse array of food extraction processes has been

effectively achieved using supercritical CO_2, including the extraction of anthocyanins from grape pomace[43], and grape seed oil.[44]

Moreover, there has been considerable attention on the synthesis of starch using CO_2. Ma *et al*. reported a chemical-biochemical hybrid pathway for starch synthesis from carbon dioxide and hydrogen in a cell-free system. They designed and constructed a non-natural solid carbon and starch synthesis pathway comprising 11 reaction steps (Figure 1.2). The complete synthesis of starch molecules from carbon dioxide was achieved in the laboratory for the first time. Nuclear magnetic resonance revealed that the structure and composition of artificially synthesized starch molecules matched those of natural starch molecules. Initial laboratory tests indicated that the efficiency of artificial starch synthesis is approximately 8.5 times that of traditional agricultural starch production. This novel pathway makes it feasible to transition starch production from traditional agricultural cultivation to industrial manufacturing, also paving the way for the synthesis of complex molecules from CO_2.[45]

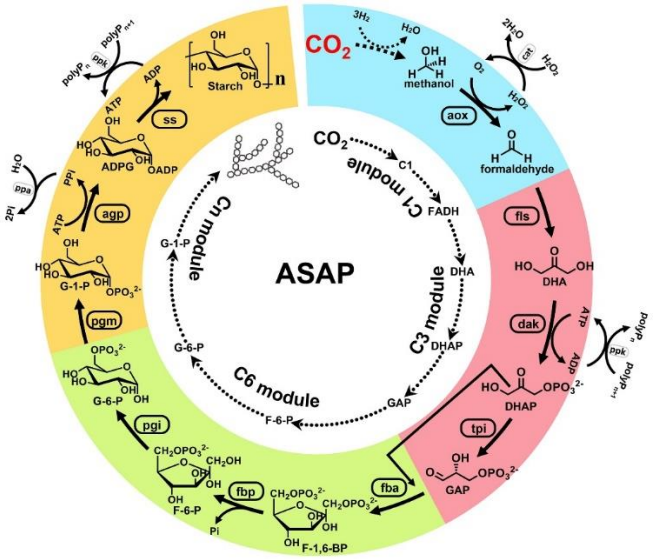

Figure 1.3 Design and modular assembly of an artificial starch anabolic pathway.[45]

In summary, CO_2 utilization technologies as the current research hotspot, are promising methods to mitigate global warming and chemical compounds derived from CO_2 would be more practical and economical.

1.2 CO_2 reforming of hydrocarbon

Although the commercialization of the CO_2 reforming of hydrocarbons process has not seen significant progress, there still attracted numerous attentions and interests on it. Since their product, syngas (hydrogen and carbon monoxide), is vital in various industries such as chemicals and fuels. Dry reforming of methane (DRM) is the most widely used reaction, the involved reactions in DRM as below. The side reactions depend on the reaction conditions and feed ratio that are applied in the reaction.[46-47] DRM has a high risk in carbon deposition, owing to its endothermic property that requires high reaction temperature. In brief, carbon is easier to be formed from reaction (6) at higher reaction temperature, while other three reactions (equation 7-9) tend to be more dominant at lower temperatures as these are the exothermic reaction.[47]

Dry reforming of methane (DRM):

$$CO_2 + CH_4 \rightarrow 2H_2 + 2CO \qquad \Delta H_{298K} = +247\ kJ \cdot mol^{-1} \qquad (4)$$

Side reactions:

$$CO_2 + H_2 \rightarrow H_2O + CO \qquad \Delta H_{298K} = +41\ kJ \cdot mol^{-1} \qquad (5)$$

$$CH_4 \rightarrow 2H_2 + C \qquad \Delta H_{298K} = +75\ kJ \cdot mol^{-1} \qquad (6)$$

$$2CO \rightarrow CO_2 + C \qquad \Delta H_{298K} = -172\ kJ \cdot mol^{-1} \qquad (7)$$

$$CO_2 + 2H_2 \rightarrow 2H_2O + C \qquad \Delta H_{298K} = -90\ kJ \cdot mol^{-1} \qquad (8)$$

$$CO + H_2 \rightarrow H_2O + C \qquad \Delta H_{298K} = -131\ kJ \cdot mol^{-1} \qquad (9)$$

As alternative to CH_4, ethane,[48-50] propane[51-52] and butane[49, 53-54] have also attracted many interests for CO_2 reforming due to the high availability of these hydrocarbons in shale gas and liquefied petroleum gas. The generalized equation of dry reforming of hydrocarbons is given as equation (10). Yan et al. conducted a thermodynamic analysis of the DRM, dry reforming of ethane (DRE), and dry reforming of butane (DRB) using the Gibbs free energy minimization algorithm. Their findings revealed that, under equilibrium conditions with a stoichiometric ratio, achieving a 50% conversion of CO_2 in lower temperatures for DRE and DRB compared to DRM. Specifically, for DRE, the conversion could be attained at 488 °C, and for DRB, it could be achieved at 444 °C. These temperatures were notably lower by approximately 100 °C and 150 °C, respectively, in comparison to DRM. This phenomenon can be attributed to the fact that the Gibbs free energies of DRE and DRB reach zero ($\Delta G° = 0$) at lower temperatures.[49]

$$nCO_2 + C_nH_{2n+2} \rightarrow (n+1)H_2 + 2nCO \qquad (10)$$

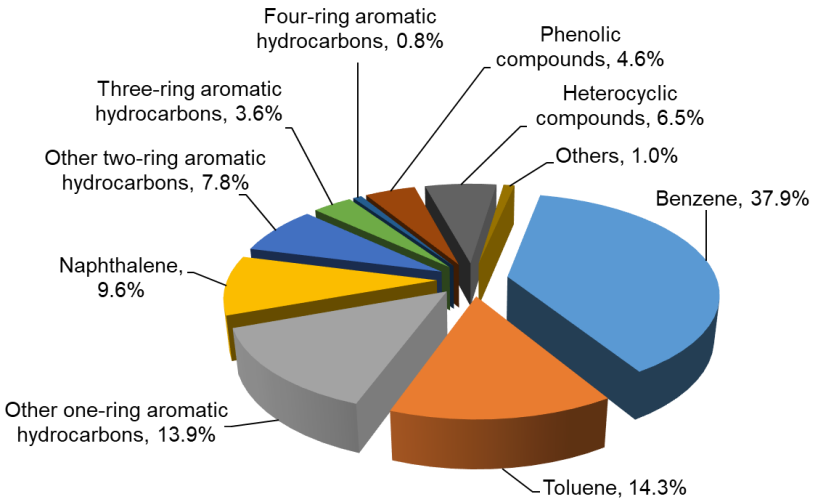

Figure 1.4 Typical composition of biomass gasification tars (wt%)[58]

Another important CO_2 reforming reaction is benzene dry reforming. On the one hand, Gasification is a promising technique to convert sustainable biomass into a useful and combustible syngas. However, bio-tar is an unavoidable byproduct originating from the incomplete cracking of organic constituents, which not only reduce the efficiency of gasification but also cause the blockage or corrosion in the downstream devices.[55-56] Benzene was selected as a model molecule due to its thermal stability and relatively high weigh percentage in the bio-tar (Figure 1.4). On the other hand, lower the CO_2 content of the produced syngas from biomass could increase its calorific value.[57] Most importantly, 1-mol of benzene can consume 6-mol of carbon dioxide, greatly enhancing CO_2 utilization. Therefore, dry reforming of benzene provides an interesting solution to reducing CO_2 and simultaneously enhancing biomass gasification efficiency.

1.3 CO_2 reforming over metallic catalysts

For the CO_2 reforming reaction, many works reported that noble metals such as Pt and Pd showed excellent activity, while the expensive price impeded its industrial application.[59-60] Ni is considered as a promising candidate due to its high activity for C-H bond cleavage, selectivity to syngas and competitively low-cost. Unfortunately, coke deposition and Ni sintering are two major issues that lead to the deactivation of catalysts.[61-62]

The coke type mainly including pyrolytic coke, whiskers and gum type.[63] Whisker carbon is the most notorious and should be avoided among them, since the formation and gasification of coke would take place at the same time during DRM, catalysts that can either inhibit the formation of coke or enhance the gasification of coke can be applied to attenuate the influence of coke on reaction activity.[60, 64]

Sintering will occur on the catalysts surface when the affinity energy between metal atoms is higher than the constraint energy of metal-support interaction at high reaction temperature.[65-66] Besides, the moisture produced from side reaction of RWGS would promote sintering.[67] Preventing small active metal particles from sintering to remain a high stable activity is essential especially for the supported catalysts.[68]

1.3.1 CO_2 reforming of methane

DRM catalysts can be classified into two types, namely supported catalysts and reduced solid solution catalysts (Figure 1.5). For a supported catalyst, the active component is anchored onto the surface of a supporting material, typically it's a metal oxide that does not include the metal element in the active species. Over the last decade, there has been significant exploration on bimetallic catalysts based on Ni catalysts,

single-atom catalysts and specifically structured metal catalysts for efficient and stable DRM.[34, 69-76]

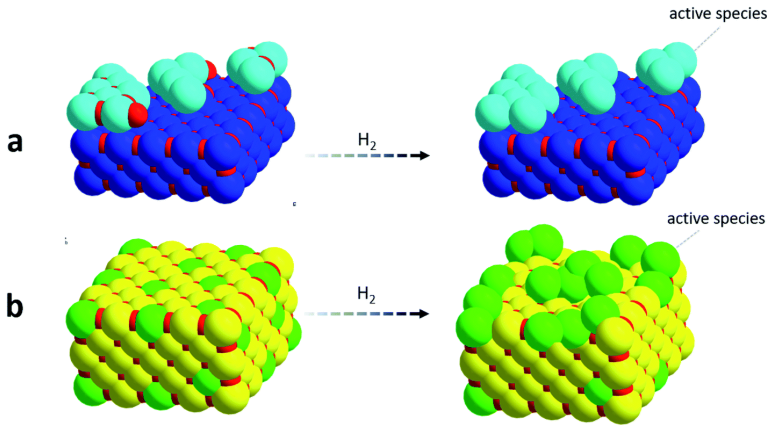

Figure 1.5 illustrations of (a) a supported catalyst and (b) a solid solution catalyst before (left) and after (right) reduction.[60]

Reduced solid solution catalysts differ from conventional supported catalysts in that their active species originate from the bulk of the solid solution, rather than an additional species. Similarities in crystal structure and lattice parameters of the oxides of the active metal species and the matrix components are the key for the formation of a solid solution.[60] For example, all MgO, NiO, and CoO possess a face-centered cubic (fcc) structure with closely matched lattice parameters: 4.2112 Å for MgO, 4.1684 Å for NiO, and 4.2667 Å for CoO. Consequently, a composite of MgO and NiO (or CoO) can readily create a stable solid solution (NiO–MgO or CoO–MgO) at a high temperature.[77] Besides, solid solution catalysts allows generate small-sized active metallic particles that have robust interactions with the solid solution matrix, leading to exceptional activity, remarkable resistance to carbon deposition and high stability during the DRM reaction.[78] At present, MgO-based reduced solid solution systems have been the most widely studied catalysts in DRM. [79-80]

1.3.2 CO_2 reforming of benzene

The catalyst of CO_2 reforming of benzene mainly focuses on Ni-based catalyst. Many strategies have been considered to activate both benzene and CO_2 molecules. Caprariis et al. reported a bimetallic NiCo catalyst promoted by Ce for benzene dry reforming, in which Ce improves the resistance to carbon deposition. In addition, the influence of two different support, γ-Al_2O_3 and activated carbon (AC), on the reaction efficiency was evaluated. As a results, the NiCo/Ce-Al_2O_3 was found to be the most active, with an enhancement of 65% and of 85% of CO and H_2 respectively during the reaction.[57] Moreover, Nam et al. developed NiFe impregnated on silicon carbide (SiC) for benzene dry reforming in a lab-scale fluidized bed reactor. A high benzene conversion rate (>90%) was observed at a higher experimental temperature (above 730ºC). However, Ni exerts a significant influence on product selectivity. NiFe/SiC catalyst resulted in higher H_2 production whereas higher CO yield was produced with Fe/SiC catalyst at an elevated temperature.[81] Although many researchers made an effort on CO_2 reforming of benzene, there still remains a room for improvement in the catalysts of this reaction.

1.4 Aim of this thesis

Reforming reactions may have one of greatest commercial potentials among many CO_2 conversion routes. However, it still has many challenges for the catalysts design as we discussed previously, such as carbon deposition and metal sintering. Hence, the aim of thesis focuses on developing a catalyst with high reactant activity, excellent stability and sintering resistance for CO_2 reforming of hydrocarbons. To meet these requirements, I propose the following directions on how to design and develop more efficient catalysts.

1.4.1 Catalyst design concept

Recently, Ni-based intermetallic compounds have been reported to improve catalytic performance and thermal stability. [34-35] However, the catalyst design based on binary intermetallic compounds has several limitations in atomic composition and elemental combination. Conversely, a wide range of composition ratios of solid-solution alloys can tune its electronic properties and catalytic performance.[82] Therefore, hybridizing the advantages of these alloy materials is highly beneficial for designing more functional catalysts. Pseudo-binary alloys, represented as $((A_{1-x}A'_x)_mB_n)$, are the promising candidate for this purpose. A part of the element A in the parent intermetallic A_mB_n was substituted by a third metal A' without changing the crystal structure of A_mB_n.[83-84] Therefore, to reduce carbon deposition while simultaneously enhancing the reactivity of reactants, a suitable combination of metals is crucial. Motivated by this concept, we designed that Ni-based pseudo-binary alloy catalyst $(Ni_{0.5}Co_{0.5})_3Ge/SiO_2$, in which Ni as the main active metal for C-H scission, the late 3d transition metal Co accelerate CO_2 adsorption and activation, and inert typical element Ge was considered to suppress the direct production of carbon. This combination has a sufficiently high

catalytic activity, coke resistance, and renewability for CO_2 reforming of methane (Scheme 1.1),

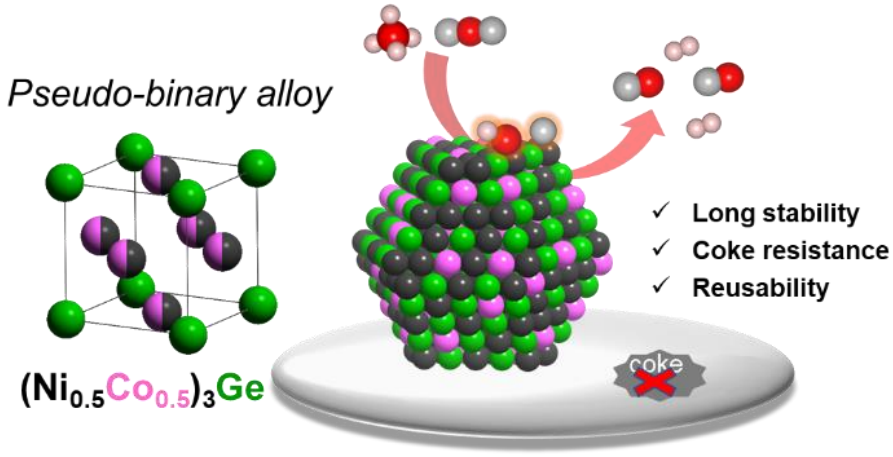

Scheme 1.1. The catalyst design concept for the $(Ni_{0.5}Co_{0.5})_3Ge/SiO_2$.

1.4.2 Fine-tuning metallic catalysts

Moreover, many other factors contributing to carbon deposition and particle agglomeration have also been taken into consideration.[85] Coking is prone to occur in the large Ni particles, since large particles typically possess lower surface energy, leading to weaker adsorption and reaction capabilities on their surface.[86] Meanwhile, if the particle agglomeration happened, the unsaturated coordination sites such as edge, corner, and vertex sites with higher catalytic activity on the Ni particles are lost, subsequently affecting their catalytic effectiveness.[87] More importantly, insufficient activation of CO_2 would break the balance between carbon formation and removal, which finally leading to the carbon deposition. [71, 88] To address these drawbacks, several strategies in this thesis have been explored as follows: (i) introducing other metals to hinder hydrocarbon complete cracking, such as alloying Ni, Co and Ge for CO_2 reforming of methane, in which Ge suppresses directly produce carbon, coking was greatly decreased compared to other corresponding binary catalysts. (ii) utilization of

redox supports to facilitate the activation of CO_2 to gasify the deposited carbon species. CeO_2 support plays an important role in our CO_2 reforming of benzene work, where the basicity and the oxygen-releasing ability of CeO_2 facilitated CO_2 adsorption and coke combustion respectively. No significant deactivation was observed within 20 h in the stability test. (iii) construction of confinement structures to immobilize Ni nanoparticles (NPs) to protect the active species from agglomeration. In the CO_2 reforming of methane, small nanoparticles with average diameter of 5.9 nm were observed on the SiO_2 support. Importantly, the STEM analysis on the spent catalyst showed that the particle size was retained even after a long-time catalytic run.

1.5 Outlines of thesis

In this research, I focused on developing a highly stable and selective alloy catalyst to enhance the CO_2 utilization in CO_2 reforming of hydrocarbons, such as dry reforming of methane, fry reforming of benzene reaction.

Chapter 2 presents a novel catalyst design based on a pseudo-binary alloy structure, $(Ni_{0.5}Co_{0.5})_3Ge/SiO_2$, in which a part of Ni atoms of intermetallic Ni_3Ge was substituted with Co without changing the parent Ni_3Ge structure, as evidenced by the combination of high-angle annular dark-field-scanning transmission electron microscopy-energy-dispersive system, X-ray diffraction, and X-ray absorption fine-structure analysis. $(Ni_{0.5}Co_{0.5})_3Ge/SiO_2$ exhibited a remarkably high coke resistance, an outstandingly long catalyst life (1000 h) at 700 °C even below the equilibrium conversion. Additionally, the used catalyst could be easily regenerated by a simple and soft oxidation procedure and the initial conversion in the second run was completely recovered in the third run. Alloying Ni with Ge not only inhibits carbon formation, but also promotes CO

formation via the CHO intermediate pathway that involves no carbon formation. The dopant Co acts as an efficient site for CO_2 adsorption and activation, which supplies more oxygen atoms to promote carbon combustion. The combination of Ge and Co allows to minimize the coke accumulation, thus achieving outstandingly high stability for long-term operation. Therefore, $(Ni_{0.5}Co_{0.5})_3Ge/SiO_2$ catalyst showed a sufficiently high catalytic activity, coke resistance, and renewability in CO_2 reforming of methane reaction.

Chapter 3 summarizes a binary intermetallic Ni_3Ga supported on CeO_2 works as an effective catalyst for CO_2-assisted dry reforming of benzene (DRB: $C_6H_6 + 6CO_2 \rightarrow 3H_2 + 12CO$). The combination of high-angle annular dark-field scanning transmission microscopy and X-ray absorption fine structure analysis confirmed the formation of the Ni_3Ga intermetallic structure. The CO_2 conversion of Ni_3Ga/CeO_2 catalyst was two-fold that of the corresponding monometallic catalyst, which might be attributed to the synergetic effect of higher CO_2 adsorption or activation of Ni–Ga alloy and CeO_2 support. Moreover, Ga plays a crucial role in improving catalytic activity and minimizing coke formation. Therefore, the Ni_3Ga/CeO_2 catalyst exhibited significantly enhanced CO_2 utilization ability and product yield.

1.6 Concluding remarks

In conclusion, our research not only demonstrates excellent catalytic performance of multi-metallic Ni-based catalysts in CO_2 conversion, but also offers a new perspective to prolong their lifespan. The findings of this study can promote the carbon-neutralization of industrial processes for CO_2 reforming of hydrocarbons

Reference

1. Gizer, S. G.; Polat, O.; Ram, M. K.; Sahiner, N., Recent developments in CO_2 capture, utilization, related materials, and challenges. *Int. J. Energy Res.* **2022,** *46*, 16241-16263.

2. Velty, A.; Corma, A., Advanced zeolite and ordered mesoporous silica-based catalysts for the conversion of CO_2 to chemicals and fuels. *Chem. Soc. Rev.,* **2023,** *52*, 1773-1946.

3. Aresta, M.; Dibenedetto, A.; Angelini, A., The changing paradigm in CO_2 utilization. *J. CO_2 Util.* **2013,** *3-4*, 65-73.

4. Aresta, M.; Dibenedetto, A.; Angelini, A., Catalysis for the Valorization of Exhaust Carbon: from CO_2 to Chemicals, Materials, and Fuels. Technological Use of CO_2. *Chem. Rev.* **2014,** *114*, 1709-1742.

5. Yaashikaa, P. R.; Senthil Kumar, P.; Varjani, S. J.; Saravanan, A., A review on photochemical, biochemical and electrochemical transformation of CO_2 into value-added products. *J. CO_2 Util.* **2019,** *33*, 131-147.

6. Valluri, S.; Claremboux, V.; Kawatra, S., Opportunities and challenges in CO_2 utilization. *J. Environ. Sci.* **2022,** *113*, 322-344.

7. Kunkes, E. L.; Studt, F.; Abild-Pedersen, F.; Schlögl, R.; Behrens, M., Hydrogenation of CO_2 to methanol and CO on $Cu/ZnO/Al_2O_3$: Is there a common intermediate or not? *J. Catal.* **2015,** *328*, 43-48.

8. Wang, W.; Wang, S.; Ma, X.; Gong, J., Recent advances in catalytic hydrogenation of carbon dioxide. *Chem. Soc. Rev.,* **2011,** *40*, 3703-27.

9. Toyir, J.; de la Piscina, P. R. r.; Fierro, J. L. G.; Homs, N. s., Highly effective conversion of CO_2 to methanol over supported and promoted copper-based catalysts: influence of support and promoter. *Appl. Catal. B: Environ.* **2001,** *29*, 207-215.

10. Toyir, J.; de la Piscina, P. R. r.; Fierro, J. L. G.; Homs, N. s., Catalytic performance for CO_2 conversion to methanol of gallium-promoted copper-based catalysts: influence of metallic precursors. *Appl. Catal. B: Environ.,* **2001,** *34*, 255-266.

11. Liu, J.; Shi, J.; He, D.; Zhang, Q.; Wu, X.; Liang, Y.; Zhu, Q., Surface active structure of ultra-fine Cu/ZrO_2 catalysts used for the CO_2+ H_2 to methanol reaction. *Appl. Catal. A: Gen.,* **2001,** *218*, 113-119.

12. Liu, X.-M.; Lu, G.; Yan, Z.-F., Nanocrystalline zirconia as catalyst support in methanol synthesis. *Appl. Catal. A: Gen.,* **2005,** *279*, 241-245.

13. Słoczyński, J.; Grabowski, R.; Olszewski, P.; Kozłowska, A.; Stoch, J.; Lachowska, M.; Skrzypek, J., Effect of metal oxide additives on the activity and stability of Cu/ZnO/ZrO_2 catalysts in the synthesis of methanol from CO_2 and H_2. *Appl. Catal. A: Gen.,* **2006,** *310*, 127-137.

14. Raudaskoski, R.; Niemelä, M. V.; Keiski, R. L., The effect of ageing time on co-precipitated Cu/ZnO/ZrO_2 catalysts used in methanol synthesis from CO_2 and H_2. *Top. Catal.* **2007,** *45*, 57-60.

15. Guo, X.; Mao, D.; Wang, S.; Wu, G.; Lu, G., Combustion synthesis of CuO–ZnO–ZrO_2 catalysts for the hydrogenation of carbon dioxide to methanol. *Catal. Commun.* **2009,** *10*, 1661-1664.

16. Słoczyński, J.; Grabowski, R.; Kozłowska, A.; Olszewski, P.; Stoch, J.; Skrzypek, J.; Lachowska, M., Catalytic activity of the M/(3ZnO· ZrO_2) system (M= Cu, Ag, Au) in the hydrogenation of CO_2 to methanol. *Appl. Catal. A: Gen.,* **2004,** *278*, 11-23.

17. Guo, X.; Mao, D.; Lu, G.; Wang, S.; Wu, G., Glycine–nitrate combustion synthesis of CuO–ZnO–ZrO_2 catalysts for methanol synthesis from CO_2 hydrogenation. *J. Catal.* **2010,** *271*, 178-185.

18. An, X.; Li, J.; Zuo, Y.; Zhang, Q.; Wang, D.; Wang, J., A Cu/Zn/Al/Zr fibrous catalyst that is an improved CO_2 hydrogenation to methanol catalyst. *Catal. lett.* **2007,** *118*, 264-269.

19. Liang, X.-L.; Dong, X.; Lin, G.-D.; Zhang, H.-B., Carbon nanotube-supported Pd–ZnO catalyst for hydrogenation of CO_2 to methanol. *Appl. Catal. B: Environ.,* **2009,** *88*, 315-322.

20. Collins, S. E.; Chiavassa, D. L.; Bonivardi, A. L.; Baltanas, M. A., Hydrogen spillover in Ga_2O_3–Pd/SiO_2 catalysts for methanol synthesis from CO_2/H_2. *Catal. lett.* **2005,** *103*, 83-88.

21. Fichtl, M. B.; Schlereth, D.; Jacobsen, N.; Kasatkin, I.; Schumann, J.; Behrens, M.; Schlogl, R.; Hinrichsen, O., Kinetics of deactivation on $Cu/ZnO/Al_2O_3$ methanol synthesis catalysts. *Appl. Catal. A: Gen.,* **2015,** *502*, 262-270.

22. Li, K.; Chen, J. G., CO_2 Hydrogenation to Methanol over ZrO_2-Containing Catalysts: Insights into ZrO_2 Induced Synergy. *ACS Catal.,* **2019**, 7840-7861.

23. An, B.; Zhang, J.; Cheng, K.; Ji, P.; Wang, C.; Lin, W., Confinement of Ultrasmall Cu/ZnOx Nanoparticles in Metal–Organic Frameworks for Selective Methanol Synthesis from Catalytic Hydrogenation of CO_2. *J. Am. Chem. Soc.* **2017,** *139*, 3834-3840.

24. Qi, T.; Zhao, Y.; Chen, S.; Li, W.; Guo, X.; Zhang, Y.; Song, C., Bimetallic metal organic framework-templated synthesis of a $Cu\text{-}ZnO/Al_2O_3$ catalyst with superior methanol selectivity for CO_2 hydrogenation. *Mol. Catal.* **2021,** *514*, 111870.

25. Studt, F.; Sharafutdinov, I.; Abild-Pedersen, F.; Elkjaer, C. F.; Hummelshoj, J. S.; Dahl, S.; Chorkendorff, I.; Norskov, J. K., Discovery of a Ni-Ga catalyst for carbon dioxide reduction to methanol. *Nat Chem* **2014,** *6*, 320-4.

26. Słoczyński, J.; Grabowski, R.; Kozłowska, A.; Olszewski, P.; Stoch, J.; Skrzypek, J.; Lachowska, M., Catalytic activity of the M/(3ZnO·ZrO_2) system (M=Cu, Ag, Au) in the hydrogenation of CO_2 to methanol. *Appl. Catal. A: Gen.* **2004,** *278*, 11-23.

27. Zhang, Z.; Hu, S.; Song, J.; Li, W.; Yang, G.; Han, B., Hydrogenation of CO2 to Formic Acid Promoted by a Diamine-Functionalized Ionic Liquid. *ChemSusChem* **2009,** *2*, 234-238.

28. Fu, L. P.; Ren, Z. K.; Si, W. Z.; Ma, Q. L.; Huang, W. Q.; Liao, K. L.; Huang, Z. L.; Wang, Y.; Li, J. H.; Xu, P., Research progress on CO_2 capture and utilization technology. *J. CO_2 Util.* **2022,** *66*.

29. Inoue, Y.; Izumida, H.; Sasaki, Y.; Hashimoto, H., Catalytic fixation of carbon dioxide to formic acid by transition-metal complexes under mild conditions. *Chem. Lett.,s* **1976,** *5*, 863-864.

30. Ezhova, N. N.; Kolesnichenko, N. V.; Bulygin, A. V.; Slivinskii, E. V.; Han, S., Hydrogenation of CO_2 to formic acid in the presence of the Wilkinson complex. *Russ. Chem. Bull.,* **2002,** *51*, 2165-2169.

31. Tai, C.-C.; Pitts, J.; Linehan, J. C.; Main, A. D.; Munshi, P.; Jessop, P. G., In Situ Formation of Ruthenium Catalysts for the Homogeneous Hydrogenation of Carbon Dioxide. *Inorg. Chem.* **2002,** *41*, 1606-1614.

32. Hanna, J.; Lee, W. Y.; Shi, Y.; Ghoniem, A. F., Fundamentals of electro-and thermochemistry in the anode of solid-oxide fuel cells with hydrocarbon and syngas fuels. *Prog. Energy Combust. Sci.,* **2014,** *40*, 74-111.

33. Liu, K.; Xing, F.; Xiao, Y.; Yan, N.; Shimizu, K.-i.; Furukawa, S., Development of a Highly Stable Ternary Alloy Catalyst for Dry Reforming of Methane. *ACS Catal.,* **2023**, 3541-3548.

34. Liu, W.; Li, L.; Lin, S.; Luo, Y.; Bao, Z.; Mao, Y.; Li, K.; Wu, D.; Peng, H., Confined Ni-In intermetallic alloy nanocatalyst with excellent coking resistance for methane dry reforming. *J. Energy Chem.,* **2022,** *65*, 34-47.

35. Kim, K. Y.; Lee, J. H.; Lee, H.; Noh, W. Y.; Kim, E. H.; Ra, E. C.; Kim, S. K.; An, K.; Lee, J. S., Layered Double Hydroxide-Derived Intermetallic $Ni_3GaC_{0.25}$ Catalysts for Dry Reforming of Methane. *ACS Catal.* **2021,** *11*, 11091-11102.

36. Joo, S.; Kim, K.; Kwon, O.; Oh, J.; Kim, H. J.; Zhang, L.; Zhou, J.; Wang, J. Q.; Jeong, H. Y.; Han, J. W.; Kim, G., Enhancing Thermocatalytic Activities by Upshifting the d-Band Center of Exsolved Co-Ni-Fe Ternary Alloy Nanoparticles for the Dry Reforming of Methane. *Angew. Chem., Int. Ed.,* **2021,** *60*, 15912-15919.

37. Zhu, Q.; Zhou, H.; Wang, L.; Wang, L.; Wang, C.; Wang, H.; Fang, W.; He, M.; Wu, Q.; Xiao, F.-S., Enhanced CO_2 utilization in dry reforming of methane achieved through nickel-mediated hydrogen spillover in zeolite crystals. *Nat. Catal.* **2022,** *5*, 1030-1037.

38. Wang, Y.; Zhang, R.; Yan, B., $Ni/Ce_{0.9}Eu_{0.1}O_{1.95}$ with enhanced coke resistance for dry reforming of methane. *J. Catal.* **2022,** *407*, 77-89.

39. Xie, K.; Cheng, F.; Duan, X., Dry reforming of CH_4/CO_2 by stable Ni nanocrystal on porous single-crystalline MgO monoliths at reduced temperatures. *Angew. Chem., Int. Ed.,* **2021,** *133*, 18940-18947.

40. Farajzadeh, R.; Eftekhari, A. A.; Dafnomilis, G.; Lake, L.; Bruining, J., On the sustainability of CO_2 storage through CO_2–Enhanced oil recovery. *Appl. Energy* **2020,** *261*, 114467.

41. Godin, J.; Liu, W.; Ren, S.; Xu, C. C., Advances in recovery and utilization of carbon dioxide: A brief review. *J. Environ. Chem. Eng.* **2021,** *9*, 105644.

42. Kupper, T.; Häni, C.; Neftel, A.; Kincaid, C.; Bühler, M.; Amon, B.; VanderZaag, A., Ammonia and greenhouse gas emissions from slurry storage - A review. *Agric. Ecosyst. Environ.* **2020,** *300*, 106963.

43. Pazir, F.; Koçak, E.; Turan, F.; Ova, G., Extraction of anthocyanins from grape pomace by using supercritical carbon dioxide. *J. Food Processing and Preser.* **2021,** *45*, e14950.

44. Duba, K.; Fiori, L., Supercritical CO_2 extraction of grape seeds oil: scale-up and economic analysis. *Int. J. Food Sci. Technol.* **2019,** *54*, 1306-1312.

45. Cai, T.; Sun, H.; Qiao, J.; Zhu, L.; Zhang, F.; Zhang, J.; Tang, Z.; Wei, X.; Yang, J.; Yuan, Q.; Wang, W.; Yang, X.; Chu, H.; Wang, Q.; You, C.; Ma, H.; Sun, Y.; Li, Y.; Li, C.; Jiang, H.; Wang, Q.; Ma, Y., Cell-free chemoenzymatic starch synthesis from carbon dioxide. *Science* **2021,** *373*, 1523-1527.

46. Shah, Y. T.; Gardner, T. H., Dry Reforming of Hydrocarbon Feedstocks. *Catal. Revi. Sci. Eng.* **2014,** *56*, 476-536.

47. Aziz, M. A. A.; Setiabudi, H. D.; Teh, L. P.; Annuar, N. H. R.; Jalil, A. A., A review of heterogeneous catalysts for syngas production via dry reforming. *J. Taiwan Inst. Chem. Eng.* **2019,** *101*, 139-158.

48. Wang, Y. N.; Sun, X. H.; Yu, X. H.; Zhang, R. J.; Yan, B. H., Coke-resistant $NdFe_{0.7}Ni_{0.3}O_3$ perovskite catalyst with superior stability for dry reforming of ethane. *Appl. Catal. B: Environ.* **2023,** *337,* 123010.

49. Yan, B. H.; Yang, X. F.; Yao, S. Y.; Wan, J.; Myint, M.; Gomez, E.; Xie, Z. H.; Kattel, S.; Xu, W. Q.; Chen, J. G. G., Dry Reforming of Ethane and Butane with CO_2 over $PtNi/CeO_2$ Bimetallic Catalysts. *ACS Catal.* **2016,** *6*, 7283-7292.

50. Zhang, T.; Liu, Z. C.; Ye, Y. C.; Wang, Y.; Yang, H. Q.; Gao, H. X.; Yang, W. M., Dry Reforming of Ethane over FeNi/Al-Ce-O Catalysts: Composition-Induced Strong Metal-Support Interactions. *Eng.* **2022,** *18*, 173-185.

51. Solymosi, F.; Tolmacsov, P.; Zakar, T. S., Dry reforming of propane over supported Re catalyst. *J. Catal.* **2005,** *233*, 51-59.

52. Al-Shafei, E.; Aljishi, M.; Albahar, M.; Alahmed, A.; Sanhoob, M., Effect of CO_2/propane ratio and trimetallic oxide catalysts on maximizing dry reforming of propane. *Mol. Catal.* **2023,** *537*.

53. Ronda-Lloret, M.; Marakatti, V. S.; Sloof, W. G.; Delgado, J. J.; Sepulveda-Escribano, A.; Ramos-Fernandez, E. V.; Rothenberg, G.; Shiju, N. R., Butane Dry Reforming Catalyzed by Cobalt Oxide Supported on Ti_2AlC MAX Phase. *Chemsuchem* **2020,** *13*, 6401-6408.

54. Li, X. D.; Yan, B. H.; Yao, S. Y.; Kattel, S.; Chen, J. G. G.; Wang, T. F., Oxidative dehydrogenation and dry reforming of n-butane with CO_2 over NiFe bimetallic catalysts. *Appl. Catal. B: Environ.,* **2018,** *231*, 213-223.

55. Shen, Y.; Zhao, P.; Shao, Q.; Ma, D.; Takahashi, F.; Yoshikawa, K., In-situ catalytic conversion of tar using rice husk char-supported nickel-iron catalysts for biomass pyrolysis/gasification. *Appl. Catal. B: Environ.,* **2014,** *152-153*, 140-151.

56. Ruiz, J. A.; Juárez, M. C.; Morales, M. P.; Muñoz, P.; Mendívil, M. A., Biomass gasification for electricity generation: Review of current technology barriers. *Renew. Sust. Energ. Rev.* **2013,** *18*, 174-183.

57. DE CAPRARIIS, B., Bassano, C., Deiana, P., Palma, V., Petrullo, A., Scarsella, M., & DE FILIPPIS, P. Carbon dioxide reforming of Tar during biomass gasification. *Chem. Eng. Trans.* **2014**, *37*, 97-102

58. Coll, R.; Salvadó, J.; Farriol, X.; Montané, D., Steam reforming model compounds of biomass gasification tars: conversion at different operating conditions and tendency towards coke formation. *Fuel Process. Technol.* **2001,** *74*, 19-31.

59. Yusuf, M.; Farooqi, A. S.; Keong, L. K.; Hellgardt, K.; Abdullah, B., Contemporary trends in composite Ni-based catalysts for CO_2 reforming of methane. *Chem. Eng. Sci.* **2021,** *229,* 116072.

60. Li, M. J.; Sun, Z. X.; Hu, Y. H., Catalysts for CO_2 reforming of CH_4: a review. *J. Mater. Chem. A,* **2021,** *9*, 12495-12520.

61. Abdulrasheed, A.; Jalil, A. A.; Gambo, Y.; Ibrahim, M.; Hambali, H. U.; Hamill, M. Y. S., A review on catalyst development for dry reforming of methane to syngas: Recent advances. *Renew. Sust. Energ. Rev.,* **2019,** *108*, 175-193.

62. Bian, Z. F.; Das, S.; Wai, M. H.; Hongmanorom, P.; Kawi, S., A Review on Bimetallic Nickel-Based Catalysts for CO_2 Reforming of Methane. *Chemphyschem* **2017,** *18*, 3117-3134.

63. Arora, S.; Prasad, R., An overview on dry reforming of methane: strategies to reduce carbonaceous deactivation of catalysts. *RSC Adv.* **2016,** *6*, 108668-108688.

64. Wittich, K.; Krämer, M.; Bottke, N.; Schunk, S. A., Catalytic dry reforming of methane: insights from model systems. *ChemCatChem* **2020,** *12*, 2130-2147.

65. Qin, Z.; Chen, J.; Xie, X.; Luo, X.; Su, T.; Ji, H., CO_2 reforming of CH_4 to syngas over nickel-based catalysts. *Environ. Chem. Lett.* **2020,** *18*, 997-1017.

66. Farmer, J. A.; Campbell, C. T., Ceria maintains smaller metal catalyst particles by strong metal-support bonding. *Science* **2010,** *329*, 933-936.

67. Pacchioni, G.; Freund, H.-J., Controlling the charge state of supported nanoparticles in catalysis: lessons from model systems. *Chem. Soc. Rev.* **2018,** *47*, 8474-8502.

68. Das, S.; Jangam, A.; Xi, S.; Borgna, A.; Hidajat, K.; Kawi, S., Highly dispersed Ni/silica by carbonization–calcination of a chelated precursor for coke-free dry reforming of methane. *ACS Appl. Energy Materials* **2020,** *3*, 7719-7735.

69. Wu, J.; Gao, J.; Lian, S.; Li, J.; Sun, K.; Zhao, S.; Kim, Y. D.; Ren, Y.; Zhang, M.; Liu, Q.; Liu, Z.; Peng, Z., Engineering the Oxygen Vacancies Enables Ni single-atom Catalyst For Stable and Efficient C-H Activation. *Appl. Catal. B: Environ.* **2022**, 121516.

70. Li, L.; Chen, J.; Zhang, Y.; Sun, J.; Zou, G., Ni-Co bimetallic catalysts on coconut shell activated carbon prepared using solid-phase method for highly efficient dry reforming of methane. *Environ. Sci. Pollut. Re.s Int.,* **2022,** *29*, 37685-37699.

71. Zhang, X.; Deng, J.; Pupucevski, M.; Impeng, S.; Yang, B.; Chen, G.; Kuboon, S.; Zhong, Q.; Faungnawakij, K.; Zheng, L.; Wu, G.; Zhang, D., High-Performance Binary Mo–Ni Catalysts for Efficient Carbon Removal during Carbon Dioxide Reforming of Methane. *ACS Catal.* **2021**, 12087-12095.

72. Turap, Y.; Wang, I.; Fu, T.; Wu, Y.; Wang, Y.; Wang, W., Co–Ni alloy supported on CeO_2 as a bimetallic catalyst for dry reforming of methane. *Int. J. Hydrogen Energ.* **2020,** *45*, 6538-6548.

73. Song, Y.; Ozdemir, E.; Ramesh, S.; Adishev, A.; Subramanian, S.; Harale, A.; Albuali, M.; Fadhel, B. A.; Jamal, A.; Moon, D.; Choi, S. H.; Yavuz, C. T., Dry reforming of methane by stable Ni-Mo nanocatalysts on single-crystalline MgO. *Science,* **2020,** *367*, 777-781.

74. Dong, J.; Fu, Q.; Li, H.; Xiao, J.; Yang, B.; Zhang, B.; Bai, Y.; Song, T.; Zhang, R.; Gao, L.; Cai, J.; Zhang, H.; Liu, Z.; Bao, X., Reaction-Induced Strong Metal-Support Interactions between Metals and Inert Boron Nitride Nanosheets. *J. Am. Chem. Soc.,* **2020,** *142*, 17167-17174.

75. Akri, M.; Zhao, S.; Li, X.; Zang, K.; Lee, A. F.; Isaacs, M. A.; Xi, W.; Gangarajula, Y.; Luo, J.; Ren, Y.; Cui, Y. T.; Li, L.; Su, Y.; Pan, X.; Wen, W.; Pan, Y.; Wilson, K.; Li, L.; Qiao, B.; Ishii, H.; Liao, Y. F.; Wang, A.; Wang, X.; Zhang, T., Atomically dispersed nickel as coke-resistant active sites for methane dry reforming. *Nat. Commun.* **2019,** *10*, 5181.

76. Li, Z. W.; Wang, Z. G.; Kawi, S., Sintering and Coke Resistant Core/Yolk Shell Catalyst for Hydrocarbon Reforming. *Chemcatchem,* **2019,** *11*, 202-224.

77. Wang, H.; Ruckenstein, E., CO_2 reforming of CH_4 over Co/MgO solid solution catalysts—effect of calcination temperature and Co loading. *Appl. Catal. A: Gen.l* **2001,** *209* , 207-215.

78. Hu, Y. H., Solid-solution catalysts for CO_2 reforming of methane. *Catal. Today* **2009,** *148*, 206-211.

79. Danghyan, V.; Kumar, A.; Mukasyan, A.; Wolf, E. E., An active and stable NiO-MgO solid solution based catalysts prepared by paper assisted combustion synthesis for the dry reforming of methane. *Appl. Catal. B: Environ.,* **2020,** *273*, 119056.

80. Lu, Y.; Jiang, S.; Wang, S.; Zhao, Y.; Ma, X., Effect of the addition of Ce and Zr over a flower-like NiO-MgO (111) solid solution for CO_2 reforming of methane. *J. CO_2 Util.,* **2018,** *26*, 123-132.

81. Nam, H.; Wang, Z.; Shanmugam, S. R.; Adhikari, S.; Abdoulmoumine, N., Chemical looping dry reforming of benzene as a gasification tar model compound with Ni- and Fe-based oxygen carriers in a fluidized bed reactor. *Int. J. Hydrogen Energ.* **2018,** *43*, 18790-18800.

82. Furukawa, S.; Komatsu, T.; Shimizu, K.-i., Catalyst design concept based on a variety of alloy materials: a personal account and relevant studies. *J. Mater. Chem. A,* **2020,** *8*, 15620-15645.

83. Xing, F. L.; Nakaya, Y.; Yasumura, S.; Shimizu, K.; Furukawa, S., Ternary platinum-cobalt-indium nanoalloy on ceria as a highly efficient catalyst for the oxidative dehydrogenation of propane using CO_2. *Nat. Catal.,* **2022,** *5*, 55-65.

84. Nakaya, Y.; Miyazaki, M.; Yamazoe, S.; Shimizu, K.-i.; Furukawa, S., Active, Selective, and Durable Catalyst for Alkane Dehydrogenation Based on a Well-Designed Trimetallic Alloy. *ACS Catal.* **2020,** *10*, 5163-5172.

85. Zhang, X.; Deng, J.; Lan, T.; Shen, Y.; Zhong, Q.; Ren, W.; Zhang, D., Promoting Methane Dry Reforming over Ni Catalysts via Modulating Surface Electronic Structures of BN Supports by Doping Carbon. *ACS Catal.* **2022**, 14152-14161.

86. Kim, J.-H.; Suh, D. J.; Park, T.-J.; Kim, K.-L., Effect of metal particle size on coking during CO_2 reforming of CH_4 over Ni–alumina aerogel catalysts. *Appl. Catal. A: Gen.,* **2000,** *19*, 191-200.

87. Goodman, E. D.; Schwalbe, J. A.; Cargnello, M., Mechanistic Understanding and the Rational Design of Sinter-Resistant Heterogeneous Catalysts. *ACS Catal.* **2017,** *7*, 7156-7173.

88. Kim, S. M.; Abdala, P. M.; Margossian, T.; Hosseini, D.; Foppa, L.; Armutlulu, A.; van Beek, W.; Comas-Vives, A.; Copéret, C.; Müller, C., Cooperativity and Dynamics Increase the Performance of NiFe Dry Reforming Catalysts. *J. Am. Chem. Soc.,* **2017,** *139*, 1937-1949.

Chapter 2

Development of a Highly Stable Ternary Alloy Catalyst for CO_2 Reforming of Methane

2. Development of a Highly Stable Ternary Alloy Catalyst for CO_2 Reforming of Methane

2.1 Introduction

Global warming and climate change have raised increasing attention recently. The development of related research to conduct the obligation for mitigating the emission of greenhouse gases has become a hotspot in academia and industry.[1-2] Dry reforming of methane (DRM: $CH_4 + CO_2 \rightarrow 2H_2 + 2CO$: $\Delta H° = 274$ kJ mol^{-1}) has been a promising strategy to convert two major greenhouse gases into highly valuable chemical feedstocks to realize a carbon-neutral energy cycle.[3] Despite DRM's advantages in both environmental and economic situations, its commercial application still suffers from a bottleneck due to the lack of highly active and coke-resistant catalysts.[4-5]

Various catalysts have been developed to effectively address this challenge.[6-8] The cost of precious metals makes them inefficient for use on a broad scale. Ni-based catalysts are considered as suitable alternatives because of the low cost and high C–H bond activation ability. However, Ni-based catalysts face critical drawbacks of carbon deposition and nickel sintering, which are correlated with the high reaction temperature required by the strong endothermic properties of DRM.[9-12] The carbon deposition mainly originates from complete dehydrogenation of CH_4 ($CH_4 \rightarrow 2H_2 + C$: $\Delta H° = 75$ kJ mol^{-1}) at high temperatures, which leads to rapid catalyst deactivation[13] In this context, a unique multifunctional active metal environment that minimizes coke formation while retaining sufficient methane activation ability must be developed for efficient, practical application.

Recently, Ni-based intermetallic compounds have been widely studied as active and stable catalysts for DRM.[14-16] However, the catalyst design based on binary intermetallic compounds has several limitations in atomic composition and elemental combination. However, a wide range of composition ratios of solid-solution alloys can tune its electronic properties and

catalytic performance.[17] Therefore, hybridizing the advantages of these alloy materials is highly beneficial for designing more functional catalysts. Pseudo-binary alloys, represented as ($(A_{1-x}A'_x)_mB_n$), are the promising candidate for this purpose. A part of the element A in the parent intermetallic A_mB_n was substituted by a third metal A' without changing the crystal structure of A_mB_n.[18-19] Here, the introduction of the third element A', provides additional functionality to the catalytic system. Additionally, the A' context *x* can be widely changed to optimize the promotional effect. Therefore, to minimize carbon accumulation for high thermal stability, an appropriate combination of the multimetallic system would optimize the adsorption energy of the CH_x reaction intermediates through the ligand and ensemble effects of alloying.[20] We developed a novel type of Ni-based pseudo-binary alloy catalyst using Ni_3Ge intermetallic compound, substituting some of Ni with Co, as directed by the above-mentioned catalyst design concept. Catalytic evaluations at 700°C exhibited an outstandingly high catalytic stability for 1000 h. Co plays an important role in inhibiting coke formation by optimizing the C–H activation ability. Additionally, the used catalyst could be easily regenerated by a simple and soft oxidation procedure and the initial conversion in the second run was completely recovered in the third run. Thus, we developed the $(Ni_{0.5}Co_{0.5})_3Ge/SiO_2$ catalyst for DRM, which showed a sufficiently high catalytic activity, coke resistance, and renewability.

2.2 Experimental Section

2.2.1 Catalyst preparation

Ni–Co–Ge/SiO_2 and Ni–Co/SiO_2 (Ni: 3 wt%) were prepared by the pore-filling co-impregnation method using $Ni(NO_3)_2 \cdot 6H_2O$ (Kanto Chemical, 98.0%), $Co(NO_3)_2 \cdot 6H_2O$ (Fujifilm Wako, 98.0%) and $(NH_4)_2GeF_6$ (Furuya Metal Co. Ltd.) as metal precursors (Ni:Co:Ge = 1.5:1.5:1, Ni:Co = 1:1). A mixture of an aqueous solution of metal precursors was added dropwise to dried SiO_2 (CARiACT G–6, Fuji Silysia, specific surface area; 500 $m^2\ g^{-1}$, pore volume; 0.7 mL g^{-1}, pore diameter; 6 nm) and then sealed and static overnight at room temperature so that the solutions flowed into the pores of SiO_2. Subsequently, the mixture was transferred to a round-bottom flask and quickly freeze with liquid nitrogen. The frozen sample was dried in a vacuum at −5°C. Next, the resulting powder was dried in an oven at 90°C overnight, calcined in air at 400°C for 1 h, and finally reduced by H_2 (0.1 MPa, 50 $mL \cdot min^{-1}$) at 700°C for 2 h with a ramping rate of 10°C $\cdot min^{-1}$. Ni–Ge/SiO_2 (Ni:Ge = 3:1, Ni: 6 wt%), Co–Ge/SiO_2 (Co:Ge = 3:1, Co: 6 wt%) and Ni–Co/SiO_2 (Ni:Co = 1:1, Ni: 3 wt%) were prepared by a similar method, where the amounts of Ni and Co were adjusted to ensure the same active component amount as Ni–Co–Ge/SiO_2. Monometallic Ni/SiO_2, Co/SiO_2 and Ge/SiO_2 were also synthesized by the same method mentioned above, in which the metal amount was comparable to those included in Ni–Co–Ge/SiO_2. Furthermore, Ni–Co–Ge/SiO_2 with different Ni/Co atomic ratios (Ni/Co = 2, Ni: 4%; Ni/Co = 0.5, Ni: 2 wt%) and other silica-supported trimetallic catalysts Ni–M–Ge/SiO_2 (M = Fe and Cu, Ni:M:Ge = 1.5:1.5:1, Ni: 3 wt%) were also prepared in a similar manner. We also tried to prepare Ni–Co–Ge/SiO_2 with high loading amount (Ni: 6 wt%) for greater activity. However, phase separation to Ni, Ni_3Ge and CoGe occurred to some extent (Figure 2.1) probably because of insufficiently homogeneous dispersion of metal precursors. Therefore, choosing an appropriate amount of metal loading is also important for high phase purity of pseudo-binary alloys.

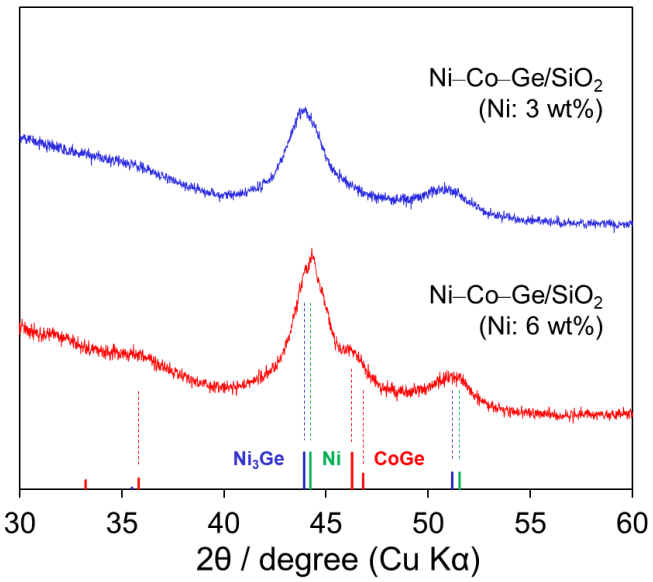

Figure 2.1. XRD patterns of Ni–Co–Ge/SiO_2 with Ni loadings of 3 wt% and 6 wt%.

2.2.2 Characterization

The catalysts' phase formation and facet orientation were determined using XRD, equipped with a Rigaku MiniFlex II/AP diffractometer with Cu Kα radiation. The particle size distribution and the crystal structure of the catalysts were analyzed by high-angle annular dark-field scanning transmission electron microscopy (HAADF–STEM) using a JEOL JEM-ARM200 Microscope EDX analyzer. An accelerating voltage of 200 kV was used for STEM analysis. All samples were ground and sonicated in ethanol before being loaded on the Mo grid. The particle size was estimated based on more than 100 particles in high-resolution STEM images. XAFS spectra of the prepared catalysts were collected at the BL01B1 and BL14B2 beamlines of SPring-8, Japan Synchrotron Radiation Research Institute (JASRI), using Si (111) double-crystals as monochromator at room temperature. The catalyst was pelletized and pretreated with H_2 at 700°C for 0.5 h in a quartz tube to prepare the XAFS specimen, then taken to an Argon glove box (O_2 < 0.01 ppm) without exposure to air after cooling to room temperature with N_2 purge. The pellet and an oxygen absorber (ISO A500-HS: Fe powder) were sealed in a plastic film bag (Barrier Nylon) to check for air leakage. The obtained XAFS spectra were fitted by Athena and Artemis software ver.0.9.25 implemented in the Demeter package. FEFF8 was applied for the calculation of the back-scattering amplitude and phase shift functions [21]. Laser Raman spectroscopy experiments were carried out using an XploRA

PLUS spectrometer (HORIBA Scientific) at room temperature to investigate the carbonaceous deposits over the spent catalysts, with 1.4 cm^{-1} resolution of the apparatus and a 638 nm excitation source. The amount of coke on the used catalysts after 20 h of DRM at 700°C was quantified by Temperature-programmed oxidation (TPO) using a BELCAT II (Microtrac BEL) instrument. First, 50 mg spent catalyst placed in a quartz tube was treated at 150°C for 30 min under a flow of He (30 $mL \cdot min^{-1}$). After cooling to 50°C, 2% O_2/He (50 $mL \cdot min^{-1}$) was passed through for baseline stabilization. Then, the catalyst was heated from 50°C to 900°C (ramping rate: $5°C \cdot min^{-1}$). An online mass spectrometer equipped downstream recorded the CO_2 amount (m/z = 44) in the outlet gas. The formation of carbon from methane and CO_2 is exothermic and downhill: $CH_4 + CO_2 \rightarrow 2C + 2H_2O$: $\Delta H° = -15.2$ $kJmol^{-1}$, $\Delta G° = -20.7$ $kJmol^{-1}$).

2.2.3 Catalytic test

The catalyst performance was examined in a fixed-bed quartz reactor with 6 mm of internal diameter at atmospheric pressure. Typically, the fresh catalyst of 100 mg was firmly fixed by quartz wool in the reactor tube. Before the DRM test, the sample was pretreated under flowing H_2 (10 $mL \cdot min^{-1}$, 700°C) for 0.5 h, followed by the residual H_2 gas purged with Ar gas (20 $mL \cdot min^{-1}$) for 0.5 h. Subsequently, the reactant gas consisting of CH_4:CO_2:Ar = 1:1:2 with a total gas flow rate of 40 $mL \cdot min^{-1}$ (GHSV = 24,000 $mL \cdot h^{-1} \cdot g_{cat}^{-1}$) was introduced into the reactor at 700°C. Compositional analysis of the effluent gas via an online gas chromatograph (Shimadzu GC-2014s), equipped with a Shincarbon-ST column and thermal conductivity detector. A long-term stability test was performed under the same conditions. The CH_4 conversion and CO_2 conversion of TOS tests were performed below thermodynamic equilibrium conversions, which reflect the intrinsic activity of catalysts. For all catalysts, the CH_4 and CO_2 conversions were defined as the following equations:

$$CH_4\ conversion: X_{CH_4}\ (\%) = \frac{F_{CH_4}^{in} - F_{CH_4}^{out}}{F_{CH_4}^{in}} \times 100$$

$$CO_2\ conversion: X_{CO_2}\ (\%) = \frac{F_{CO_2}^{in} - F_{CO_2}^{out}}{F_{CO_2}^{in}} \times 100$$

$$\frac{H_2}{CO} = \frac{F_{H_2}^{out}}{F_{CO}^{out}}$$

$$Carbon\ balance: C_b = \frac{F_{CO}^{out} + F_{CH_4}^{out} + F_{CO_2}^{out}}{F_{CH_4}^{in} + F_{CO_2}^{in}} \times 100$$

where, $F_{CH_4}^{in}$, $F_{CO_2}^{in}$ and$F_{CH_4}^{out}$ $F_{CO_2}^{out}$, $F_{H_2}^{out}$, F_{CO}^{out}, indicate the inlet flow rate of CH_4, CO_2, and outlet flow rates of CH_4, CO_2, H_2, and CO, respectively.

The deactivation constant and mean catalyst life was defined as follows:

$$Deactivation\ constant: k_d = \left\{\ln\left(\frac{1 - X_{CH_4}^f}{X_{CH_4}^f}\right) - \ln\left(\frac{1 - X_{CH_4}^i}{X_{CH_4}^i}\right)\right\}(t^f - t^i)^{-1}$$

$$Mean\ catlyst\ life: \tau = \frac{1}{k_d}$$

where, $X_{CH_4}^i$ and $X_{CH_4}^f$ indicate the initial (t^i: 0), and final (t^f: 1000 h) X_{CH_4}.

2.2.4 Computational details

Periodic DFT calculations were performed using the CASTEP code[22] with Vanderbilt-type ultrasoft pseudopotentials and the revised version of Perdew−Burke−Ernzerhof exchange−correlation functional based on the generalized gradient approximation.[23] The plane-wave basis set was truncated at a kinetic energy of 360 eV. A Fermi smearing of 0.1 eV was used with a spin-polarization condition. Dispersion correlations were considered using the Tkatchenko–Scheffler method with a scaling coefficient of s_R = 0.94 and a damping parameter of d = 20.[24] The reciprocal space was sampled using a k-point mesh with a typical spacing of 0.04 $Å^{-1}$, as generated by the Monkhorst−Pack scheme.[25] Supercell structures were subjected to geometry optimizations using the periodic boundary conditions. The unit cell size of the bulk

Ni and Ni_3Ge crystal was first optimized. Then, for calculation of paths (A) and (B), slab structures were prepared using Ni(111)–(2×2) and Ni_3Ge(111)–(1×1) supercells (thickness of four atomic layers) with 13 Å as vacuum space on the c-axis, followed by the geometry optimization with the cell size fixed for surface relaxation. For CO_2 adsorption and activation, Ni_3Ge(111)–(2×2) supercell and its Co-doped model were used. For the doped model, a half of Ni atoms in the supercell were randomly chosen using random numbers and substituted with Co atoms to reproduce $(Ni_{0.5}Co_{0.5})_3Ge$(111) surface, followed by geometry optimization. The convergence criteria for structure optimization and energy calculation were set to (a) an SCF tolerance of 1.0×10^{-6} eV per atom, (b) an energy tolerance of 1.0×10^{-5} eV per atom, (c) a maximum force tolerance of 0.05 eV $Å^{-1}$, and (d) a maximum displacement tolerance of 1.0×10^{-3} Å. The net charge was set to zero for all calculations, and spin polarization was considered. A transition state search was performed based on the complete linear synchronous transit/quadratic synchronous transit method[26-27] with the tolerance for all root-mean-square forces on an atom of 0.10 eV $Å^{-1}$.

2.3 Results and Discussion

2.3.1 Characterization of the catalysts structure

The silica-supported Ni–Co–Ge catalyst was synthesized using a pore-filling co-impregnation method. The elemental maps obtained by energy-dispersive X-ray (EDX) spectroscopy and the high-angle annular dark-field scanning transmission electron microscopy (HAADF–STEM) images of Ni–Co–Ge/SiO_2 are shown in Figures 2.2a–d. The nanoparticles consisting of Ni, Co, and Ge were evenly dispersed on the SiO_2 support and constituted ternary alloy nanoparticles. Small nanoparticles with diameters ranging mainly from 3 to 8 nm (average of 5.9 nm) were observed on the SiO_2 support (Figure 2.2e). The high-resolution HAADF–STEM image of a single Ni–Co–Ge nanoparticle shown an atomic arrangement with interplanar distances of 1.83 and 1.85 Å, which were similar but slightly larger than (200) and (020) planes (1.79 Å) of intermetallic Ni_3Ge (Figure 2.2g). A possible interpretation is that the Ni sites of Ni_3Ge lattice were partially substituted with Co, whose atomic size was slightly larger than Ni (2.8% lattice expansion). The X-ray diffraction (XRD) patterns of Ni–Co–Ge/SiO_2 showed slight lower-angle shifts of the 111 and 200 diffractions (Figure 2.2g), which supports the lattice expansion caused by the introduction of Co. The inset in Figure 2.2f shows the fast Fourier transform of the HAADF-STEM image, in which superlattice diffraction spots (100 and 110) were clearly observed in addition to the main diffractions of 200 and 220. The corresponding diffraction was also observed as a small peak at ca. 35.2° in XRD (Figure 2.3). These results support the formation of the Ni_3Ge-type $L1_2$ ordered structure. Thus, he $(Ni_{0.5}Co_{0.5})_3Ge$ pseudo-binary alloy structure was successfully formed on the SiO_2 support.

We also performed an X-ray absorption fine structure (XAFS) analysis to obtain further structural information. The X-ray absorption near-edge spectra (Figures 2.4-2.6) showed that Ni, Co, and Ge were in a metallic state and that the Ni and Ge K-edge features of Ni–Co–

Ge/SiO_2 were similar to those of Ni–Ge/SiO_2, suggesting that Co showed no electronic effect on the electronic states of Ni and Ge. Curve fitting analysis of the EXAFS oscillations (Table 2.1 and Figures 2.7–2.8) revealed that Ni–Ge and Ni–Ni scatterings in intermetallic Ni_3Ge can be distinguished by EXAFS, and the ratio of their coordination numbers (CNs) was 2.0 ($CN_{Ni–Ni}$: 7.2, $CN_{Ni–Ge}$: 3.6), which is consistent with the $L1_2$ Ni_3Ge structure. Similar trends were also observed for Ni–Co–Ge, where the $CN_{Ni–Ni(Co)}/CN_{Ni–Ge}$ and $CN_{Co–Co(Ni)}/CN_{Co–Ge}$ ratios were 2.0 (8.3/4.1 and 6.5/3.2, respectively). Besides, the sum of $CN_{Ni–Ge}$ (4.1) and $CN_{Co–Ge}$ (3.2) agreed with $CN_{Ge–Ni(Co)}$ (7.7) within the error bars. These results strongly support that Co atoms occupy the Ni sites of Ni_3Ge but not the Ge sites, demonstrating the pseudo-binary alloy structure. Considering that $CN_{Co–Co(Ni)}$(6.5) is lower than $CN_{Ni–Ni(Co)}$ (8.3), the distribution of Co atoms in the Ni sites may be slightly biased to the surface region. Furthermore, the Ni–Ge interatomic distance in the Ni–Co–Ge/SiO_2 catalyst (2.65 Å) was slightly longer than that of Ni_3Ge/SiO_2 (2.57 Å), which is consistent with the lattice expansion due to the Co doping. This excludes the possibility that Ni–Co–Ge/SiO_2 comprises a physical mixture of intermetallic Ni_3Ge and Co_3Ge nanoparticles.

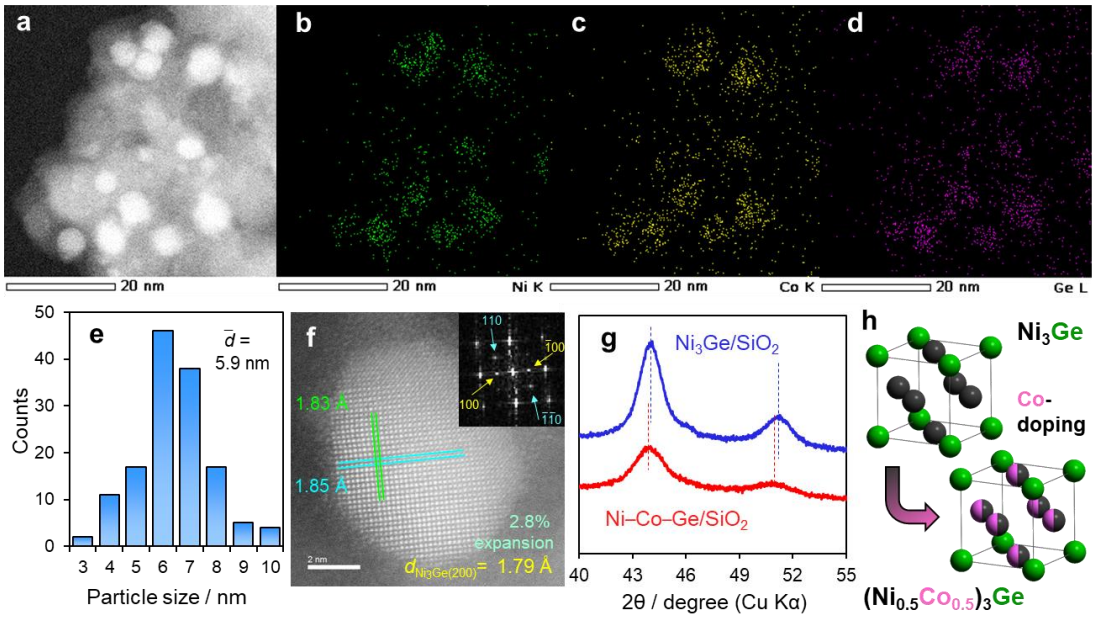

Figure 2.2. Characterization of Ni–Co–Ge/SiO_2 catalyst. **a** HAADF–STEM image of Ni–Co–Ge/SiO_2 (Ni:Co:Ge=1.5:1.5:1), **b-d** corresponding elemental maps for (**b**) Ni, (**c**) Co, and (**d**) Ge, acquired by EDX. **e** Particle size distribution. **f** HAADF–STEM image of a single nanoparticle on Ni–Co–Ge/SiO_2. **g** XRD patterns of Ni–Co–Ge/SiO_2 and Ni–Ge/SiO_2 catalysts. **h** Model of the $(Ni_{1-x}Co_x)_3Ge$ pseudo-binary alloy structure with the crystal structure unit.

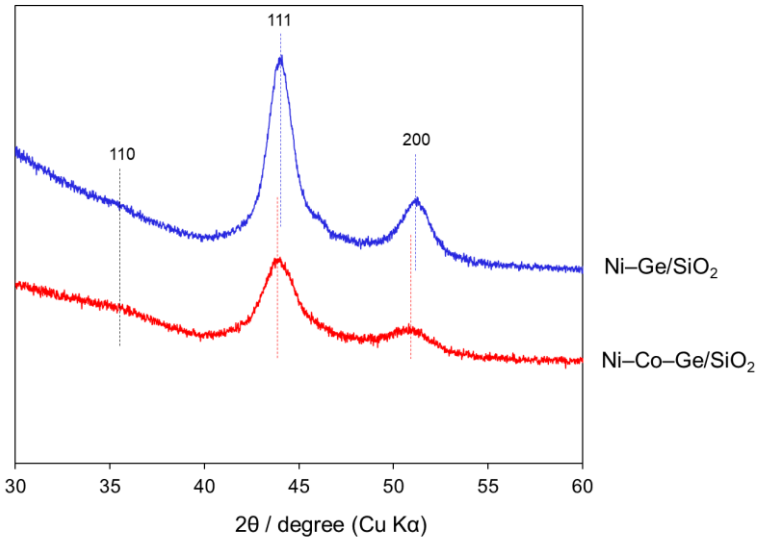

Figure 2.3. XRD patterns of Ni–Co–Ge/SiO_2 and Ni–Ge/SiO_2 catalysts.

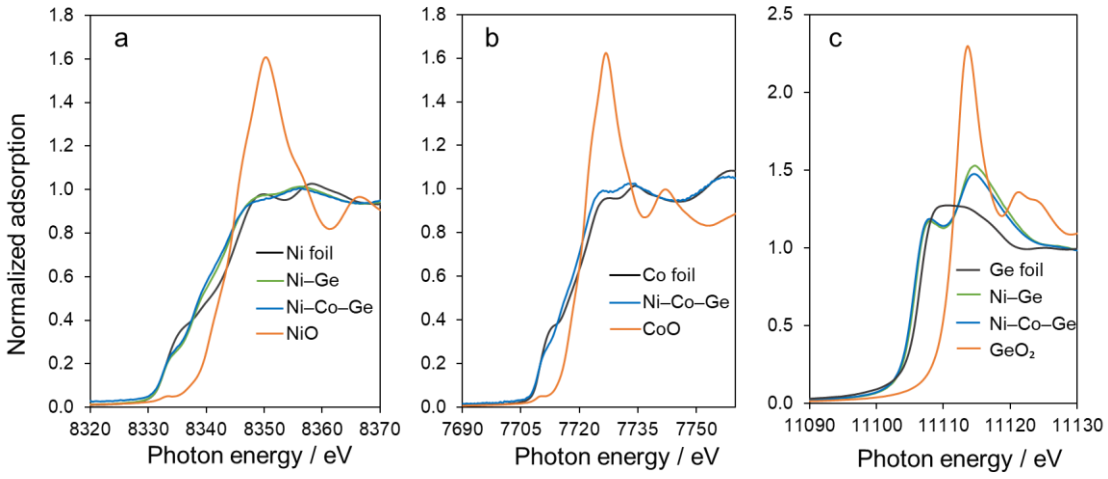

Figure 2.4. (a) Ni, (b) Co and (c) Ge K-edge X-ray absorption near edge structure (XANES) spectra of the Ni–Co–Ge/SiO_2 and Ni–Ge/SiO_2 catalysts and reference compounds.

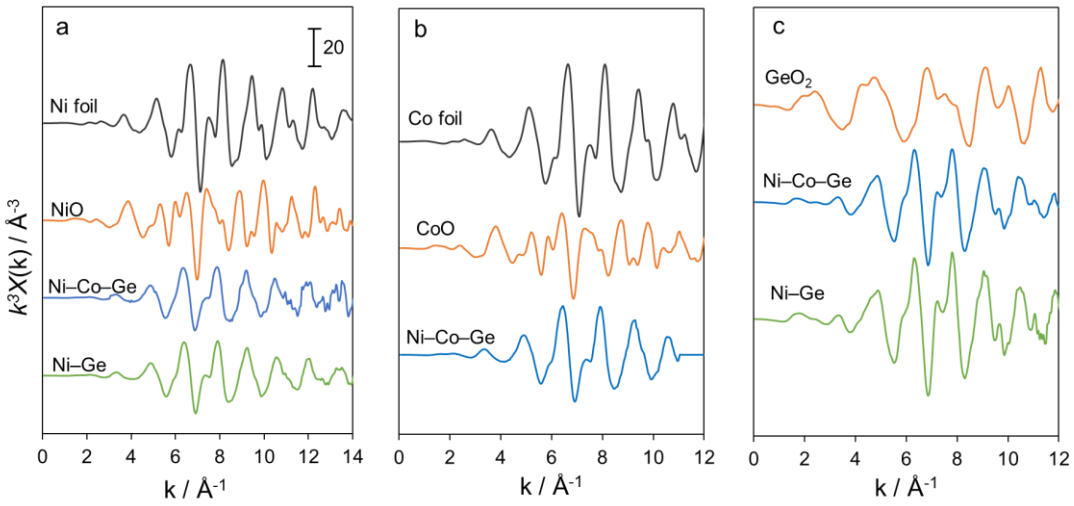

Figure 2.5. (a) Ni, (b) Co and (c) Ge K-edge extended X-ray absorption fine structure (EXAFS) spectra of the Ni–Co–Ge/SiO_2 and Ni–Ge/SiO_2 catalysts and reference compound.

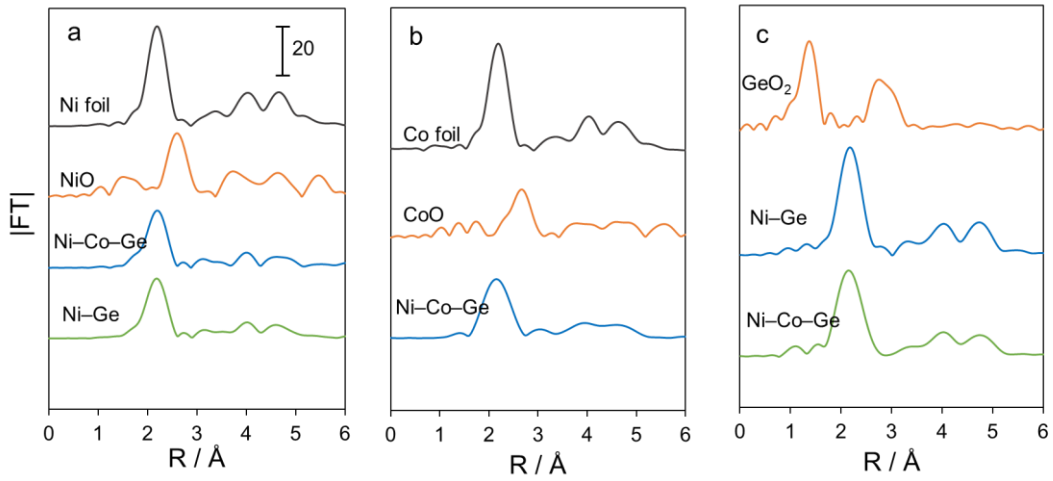

Figure 2.6. Fourier-transforms of EXAFS in (a) Ni, (b) Co and (c) Ge K-edge of the Ni–Co–Ge/SiO_2 and Ni–Ge/SiO_2 catalysts and reference compounds.

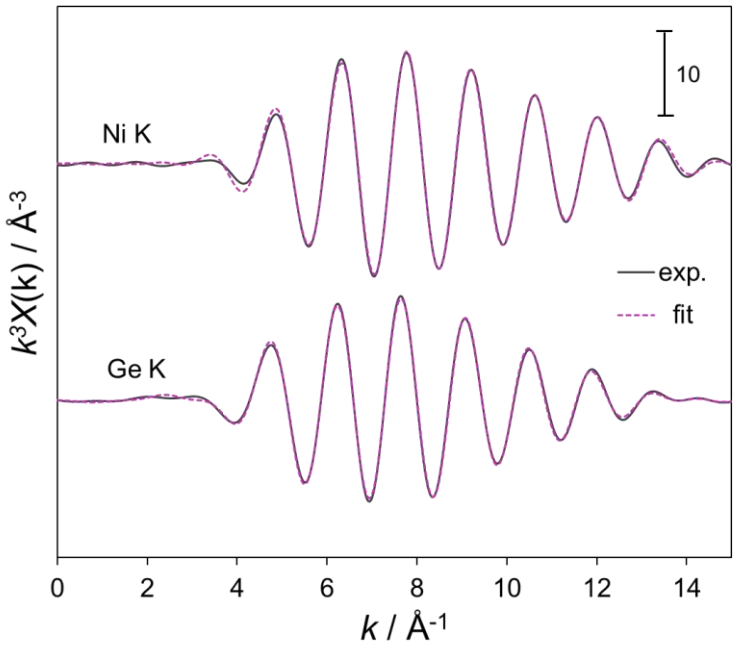

Figure 2.7. Curve-fitting results of Ni K and Ge K-edge k^3-weighted EXAFS of Ni–Ge/SiO_2. Solid and dashed lines indicate the results of simulation and experiment, respectively.

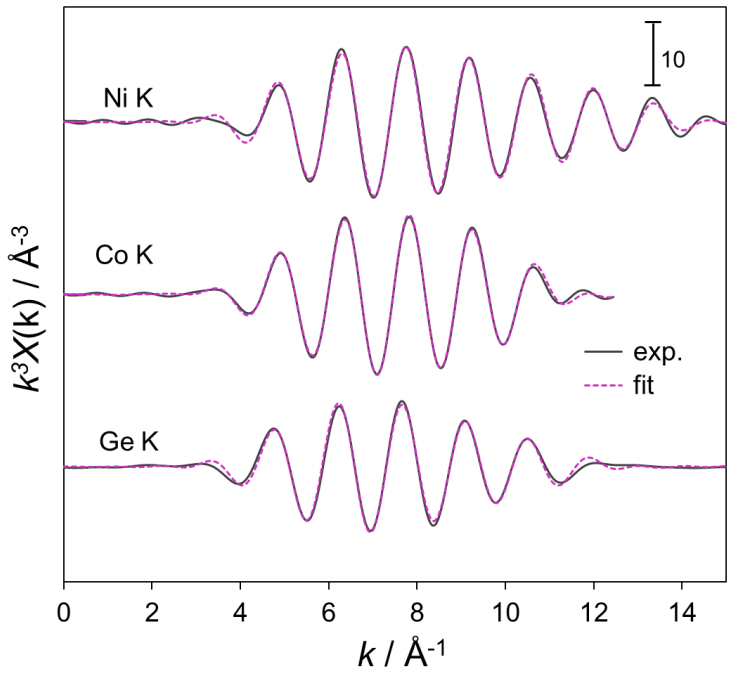

Figure 2.8. Curve-fitting results of Ni K, Co K and Ge K-edge k^3-weighted EXAFS of Ni–Co–Ge/SiO_2. Solid and dashed lines indicate the results of simulation and experiment, respectively. The k^3-weighted EXAFS oscillation was Fourier-transformed in the k range of 3-14 $Å^{-1}$, 3-11 $Å^{-1}$ and 3-12 $Å^{-1}$ for Ni K, Co K and Ge K-edge separately. Curve-fitting was performed using the back Fourier-transforms of the coordination peaks ranging between 1.0−3.1 Å, 1.0−3.0 Å, and 1.3−3.0 Å for Ni K, Co K and Ge K-edge, respectively.

Table 2.1. Results of EXAFS curve-fitting analysis for Ni–Co–Ge/SiO_2 and Ni–Ge/SiO_2 catalysts.

Sample	Edge	Shell	S_o^2	CN	r (Å)	ΔE_o (eV)	σ^2 ($Å^2$)	R-factor
Co foil	Co K	Co–Co	0.84	12 (fix)	2.49 ± 0.0014	7.4 ± 0.8	0.007	0.016
		Co–Co		6 (fix)	3.52 ± 0.013		0.010	
		Co–Co		24 (fix)	4.36 ± 0.008		0.011	
Ni foil	Ni K	Ni–Ni	0.95	12 (fix)	2.48 ± 0.004	7.03 ± 0.8	0.007	0.019
		Ni–Ni		6 (fix)	3.50 ± 0.014		0.010	
		Ni–Ni		24 (fix)	4.33 ± 0.008		0.009	
GeO_2	Ge K	Ge–O	1.04	4 (fix)	1.74 ± 0.005	5.3 ± 1.6	0.003	0.006
		Ge–Ge		4 (fix)	3.16 ± 0.007		0.004	
		Ge–O		4 (fix)	3.34 ± 0.02		0.001	
Ni–Ge/SiO_2	Ni K	Ni–Ni	0.95	7.2 ± 0.9	2.51 ± 0.006	1.0 ± 1.7	0.006	0.003
		Ni–Ge		3.6 ± 0.9	2.57 ± 0.116		0.018	
	Ge K	Ge–Ni	1.04	8.5 ± 0.5	2.51 ± 0.004	8.4 ± 0.7	0.009	0.003
		Ge–O		1.5 ± 1.4	1.78 ± 0.04		0.015	
Ni–Co–Ge/SiO_2	Ni K	Ni–Ni/Co	0.95	8.3 ± 0.9	2.52 ± 0.009	2.5 ± 1.6	0.007	0.011
		Ni-Ge		4.1 ± 0.9	2.65 ± 0.05		0.014	
	Co K	Co–Co/Ni	0.84	6.5 ± 0.6	2.56 ± 0.02	3.6 ± 1.4	0.004	0.002
		Co–Ge		3.2 ± 0.6	2.43 ± 0.04		0.003	
	Ge K	Ge–Ni (Co)	1.04	7.7 ± 0.7	2.51 ± 0.006	8.5 ± 1.0	0.009	0.008

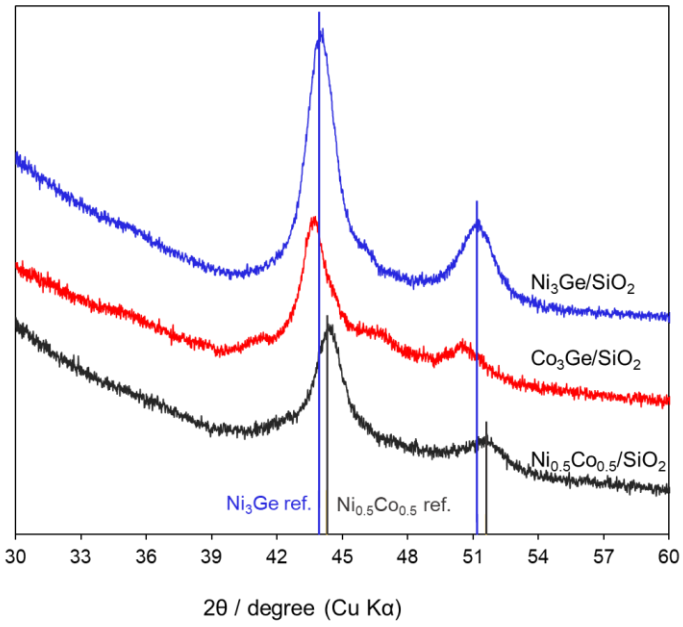

Figure 2.9. XRD patterns of Ni_3Ge/SiO_2, Co_3Ge/SiO_2, and $Ni_{0.5}Co_{0.5}/SiO_2$ catalysts.

2.3.2 Catalytic performance

Next, we tested the prepared $(Ni_{0.5}Co_{0.5})_3Ge/SiO_2$ catalyst in DRM at 700°C and compared it with the control catalysts (Ni_3Ge/SiO_2, Co_3Ge/SiO_2, and $Ni_{0.5}Co_{0.5}/SiO_2$; see Figure 2.9 for their XRD patterns). Note that the mole of Ni, Co, or Ni + Co was equalized for each catalyst (Table 2.2). The time course of CH_4 and CO_2 conversions is shown in Figures. 2.10a–b (see Figure 2.11 for details of equilibrium conversion). Although $Ni_{0.5}Co_{0.5}$ showed high initial conversions of CH_4 and CO_2 (72%–80%), it was rapidly deactivated within 5 h due to coke accumulation. High conversion and good stability were observed in Ni_3Ge, indicating that alloying with Ge is necessary for high stability. Co_3Ge was much less active than the Ni-based catalysts, which could be ascribed to Co's lower C–H activation ability than Ni.[28] For at least 140 h, $(Ni_{0.5}Co_{0.5})_3Ge$ showed high initial conversions and retained them with negligible

deactivation (CH_4: 67%–62%, CO_2 75%–71%). Thus, the Co doping further promoted the catalyst stability of Ni_3Ge in DRM. CO_2 conversion was always higher than CH_4 conversion, and the H_2/CO ratio was approximately 0.8 (Figure 2.12), which indicates the occurrence of reverse water-gas shift reaction (RWGS: $CO_2 + H_2 \rightarrow CO + H_2O$) to some extent. We also tested other Ni/Co ratios of $(Ni_{1-x}Co_x)_3Ge/SiO_2$ (see Figure 2.13 for XRD patterns) and Fe- or Cu-doping instead of Co (Figure 2.14 and Figure 2.15, respectively). Deviating from the equimolar ratio of Ni:Co resulted in slightly lower conversions, indicating the optimum Ni/Co ratio of unity. Ni–Cu–Ge and Ni–Fe–Ge showed much lower catalytic activity than Ni–Co–Ge, which is probably due to their lower ability for C–H activation and shows the validity of Co as the third metal. Thereafter, monometallic Ni/SiO_2, Co/SiO_2 and Ge/SiO_2 catalysts were also tested for the DRM reaction as control experiments (Figure 2.16). Although Ni/SiO_2 showed high initial conversion for both CH_4 and CO_2 conversion, it rapidly deactivated within 70 h. Co/SiO_2 retained the low CH_4 conversion (15%), which is probably due to the weak C–H activation ability of Co metal. Ge/SiO_2 was almost inactive for DRM reaction. We conducted further control experiments using physical mixtures of the bimetallic and monometallic catalysts (Ni/SiO_2+Co–Ge/SiO_2, Ni–Ge/SiO_2+Co/SiO_2 and Ni–Co/SiO_2 + Ge/SiO_2). The activity and stability of these mixtures were obviously lower than those of Ni–Co–Ge/SiO_2 (Figure 2.17), demonstrating that the ternary alloy structure is essential for the outstanding catalytic performance.

Then, we investigated the long-term stability of the developed catalyst at 700°C for 1000 h, which is also an important factor for the industrial application of DRM. Although a slight decrease in conversion was observed, approximately 70%–80% of the initial conversions of CH_4 and CO_2 were retained even at 1000 h on stream (Figure 2.10c, see Figure 2.18 for H_2/CO ratio and carbon balance), where the deactivation constant k_d was 0.00077 h^{-1}. The reciprocal deactivation constant ($\tau = k_d^{-1}$), which is often used as a scale of stability, was 1300 h (Figure

2.10d). Although some moderately high τ values (400–800 h) have been reported, they were estimated from experiments

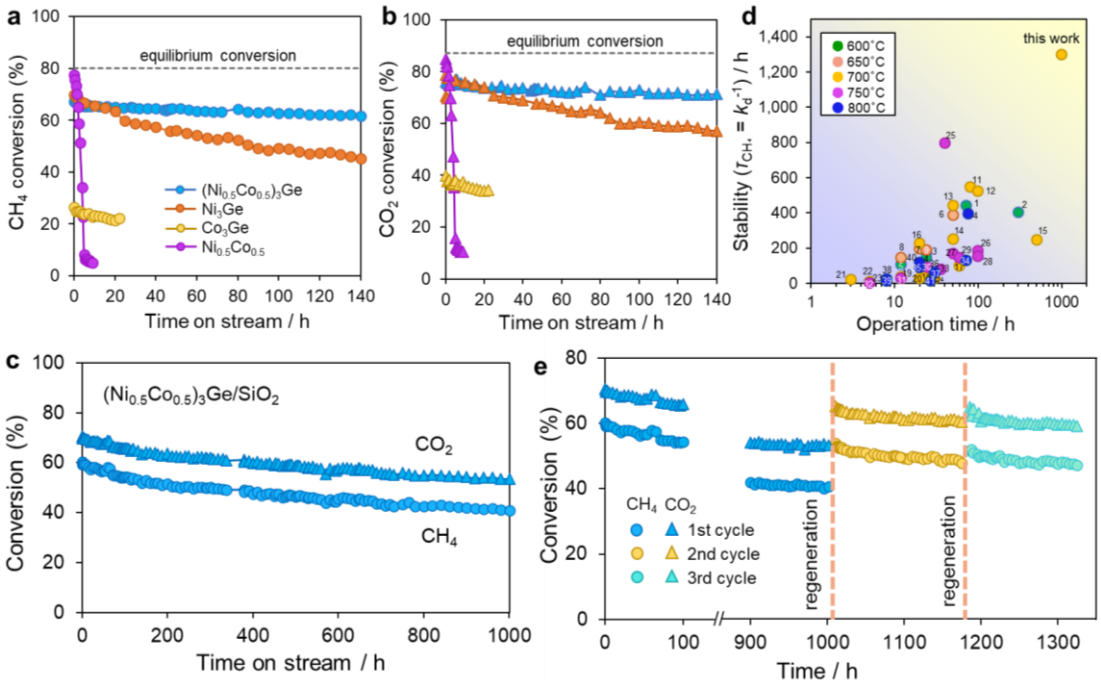

Figure 2.10. Catalytic performance of Ni-based catalysts in DRM. Reaction conditions: catalyst amount of 100 mg, CH_4:CO_2:Ar = 10:10:20 mL·min^{-1}, 700°C, 1 bar. **a, b** Time course of **(a)** CH_4 Conversions and **(b)** CO_2 Conversions. **c** Long-term stability of CH_4 conversion and CO_2 conversion over $(Ni_{0.5}Co_{0.5})_3Ge/SiO_2$. **d** Comparison of the stability with reported Ni-based DRM catalysts under equilibrium conversion. Numbers correspond to the entries in Table 2.3. **e** Regeneration test using $(Ni_{0.5}Co_{0.5})_3Ge/SiO_2$ during three catalytic cycles. Regeneration conditions: CO_2:Ar = 10:10 mL·min^{-1} for 7 h, followed by H_2 of 10 mL·min^{-1} for 1 h at 700°C.

with much shorter periods (<100 h, Figure 2.10d; see Table 2.3 and Figure 2.19 for details; note that the *x*-axis is shown in a log scale for clarity). However, we obtained much higher τ values from an actual long catalytic run. For a fair comparison, Figure 2.10d does not include reported systems in which the CH_4 conversion reached (or exceeded) the thermodynamic equilibrium and/or increased during the reaction. This is because the deactivation trend cannot

be accurately evaluated when the conversion is saturated or when some induction period is included, i.e., there is a possibility that catalyst deactivation has not been reflected in the conversion trend due to the use of an excess catalyst or due to some structural change (see Table 2.4 and Table 2.5 and Figure 2.20 for the full comparison with those not included in Figure 2.10d and Table 2.3).

We also examined the reusability of $(Ni_{0.5}Co_{0.5})_3Ge/SiO_2$ after a simple regeneration process. Generally, deposited carbon on deactivated catalysts is combusted in the presence of oxygen or air in a regeneration process. In this study, however, CO_2 was used as a soft oxidant to combust carbon via the reverse Boudouard reaction ($CO_2 + C \rightarrow 2CO$). Another merit for easier handling of this is that switching the catalytic run to the regeneration process only requires shutting off the supply of methane in the feed gas at the same temperature. Before the second catalytic run, the catalyst was reduced by flowing H_2 reduction for 1 h at the same temperature after feeding CO_2/Ar for 7 h. The initial conversion of CH_4 and CO_2 were only slightly lower than those in the first runs (Figure 2.10e). They reached a steady-state after 1170 h, probably because CO_2 could combust not all the carbonaceous species at that temperature. The initial conversions in the second run were fully recovered in the third catalytic run after the second regeneration process, demonstrating the continuous reusability of $(Ni_{0.5}Co_{0.5})_3Ge/SiO_2$. A similar trend was also observed in the H_2/CO ratio change and carbon balance (Figure 2.21). The full recovery of the initial activity after regeneration and the repeated reusability is very rare in reported systems for DRM (Tables 2.3–2.5). Thus, the $(Ni_{0.5}Co_{0.5})_3Ge$ catalyst displayed multifunctional functionalities of high catalytic activity, outstanding long-term stability, and repeated reusability. The STEM analysis on the spent $(Ni_{0.5}Co_{0.5})_3Ge$ catalyst showed that the particle size was retained even after a long time catalytic run (5.9 nm → 5.9 nm, Figure 2.22), which evidenced the high thermal stability of the $(Ni_{0.5}Co_{0.5})_3Ge$ pseudo-binary alloy structure. [29] Moreover, we performed a stability test

using $(Ni_{0.5}Co_{0.5})_3Ge$ under a neat condition (CH_4:CO_2 = 10:10 mL min^{-1}) as a more praction condition. No deactivation was observed up to 200 h (Figure 2.23), demonstrates the outstanding durability for practical application.

Table 2.2. The active metal loading of the catalysts.

Catalyst	metal loading (wt%)		Active metal mole amount / mmol (per 100 mg catalyst)
	Ni	Co	
$(Ni_{0.5}Co_{0.5})_3Ge/SiO_2$	3	3	0.1020
Ni_3Ge/SiO_2	6	0	0.1022
Co_3Ge/SiO_2	6	0	0.1019
$Ni_{0.5}Co_{0.5}/SiO_2$	3	3	0.1020

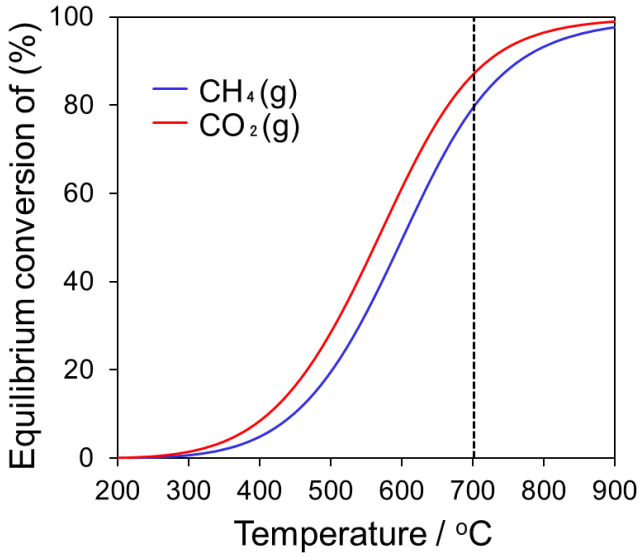

Figure 2.11. Calculated equilibrium conversion of CH_4 and CO_2 in DRM (CH_4:CO_2:Ar = 1:1:2) as a function of temperature. Calculation was finished by a Gibbs free energy minimization algorithm implemented in HSC Chemistry 8.

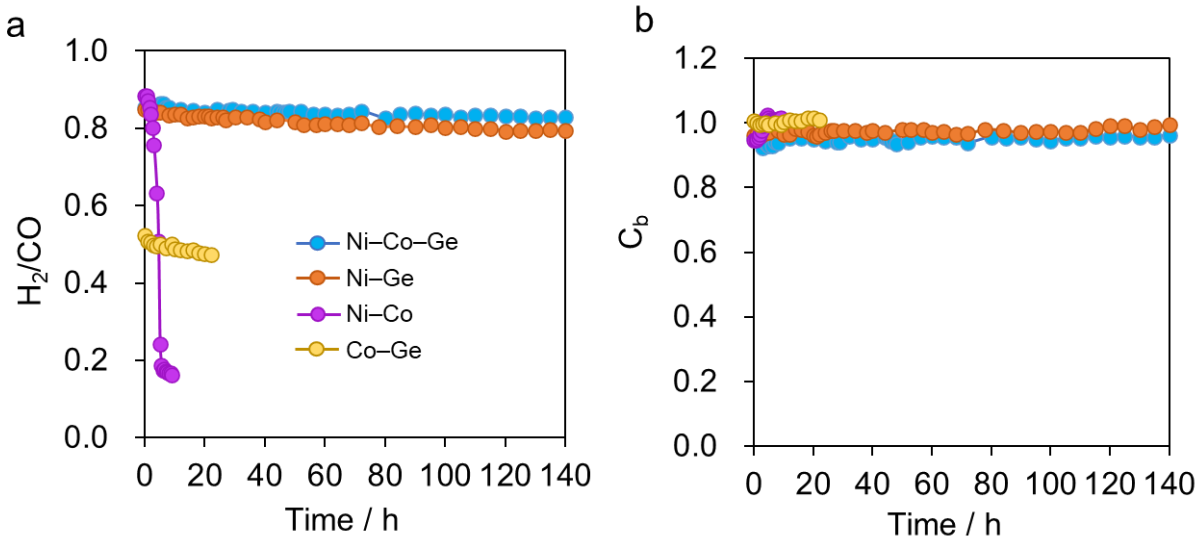

Figure 2.12. (a) Product H_2/CO ratio, (b) Carbon balance of $(Ni_{0.5}Co_{0.5})_3Ge/SiO_2$ and other binary catalysts.

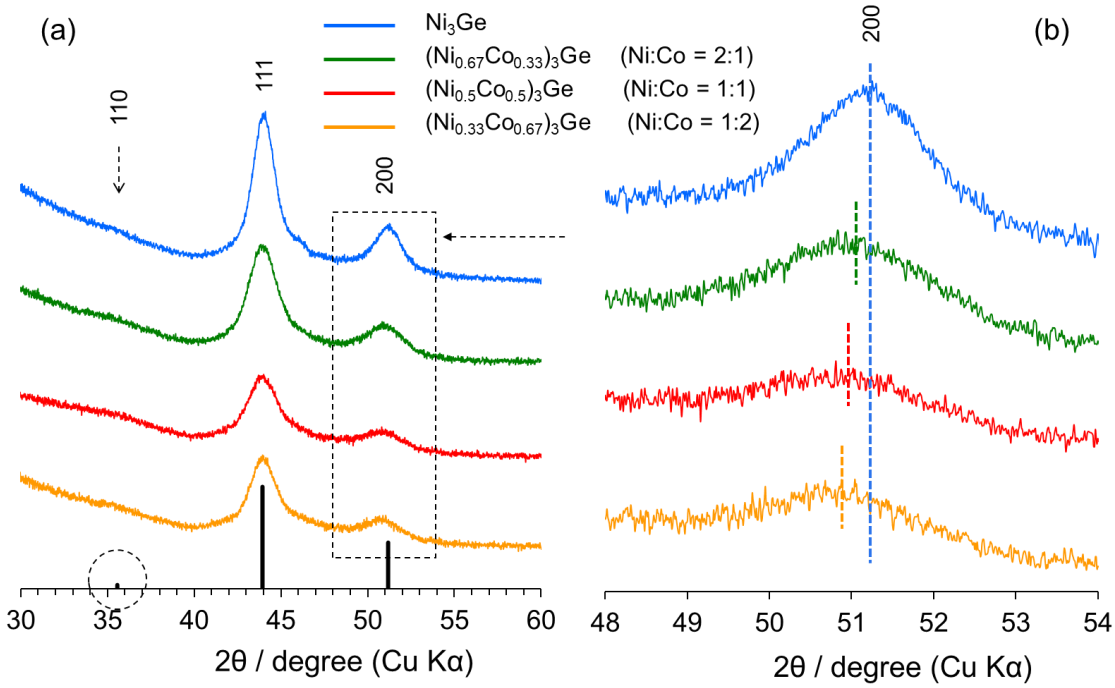

Figure 2.13. (a) XRD patterns of $(Ni_{1-x}Co_x)_3Ge/SiO_2$ (x = 0, 0.33, 0.5, and 0.67) and (b) their magnification of the region designated as a dotted square. Vertical dashed lines indicate the center of these diffractions. $(Ni_{1-x}Co_x)_3Ge/SiO_2$ showed diffraction peaks similar to that of

Ni_3Ge/SiO_2 with a small feature of 110 diffraction, which indicates the formation. Moreover, the peak position of the 200 diffraction slightly shifted in the order of $x = 0 > 0.33 > 0.5 > 0.67$. These results support that pseudo-binary alloys with various Ni:Co ratio were successfully formed with high phase purities.

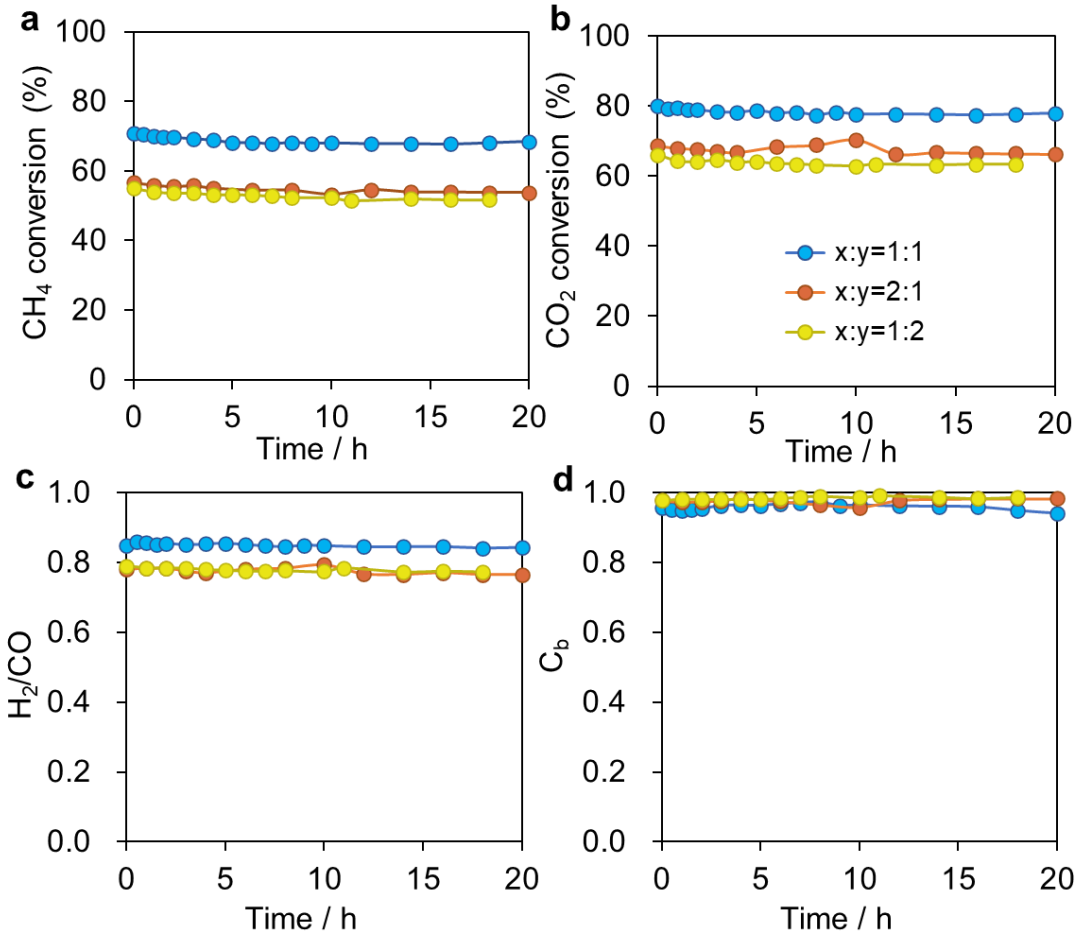

Figure 2.14. Catalytic activity of different Ni/Co ratio in $(Ni_xCo_y)_3Ge/SiO_2$. (a) CH_4 conversion, (b) CO_2 conversion, (c) H_2/CO ratio, and (d) carbon balance. Reaction conditions: catalyst amount of 100 mg, $CH_4:CO_2:Ar = 10:10:20$ mL·min^{-1}, 700 °C, 1 bar.

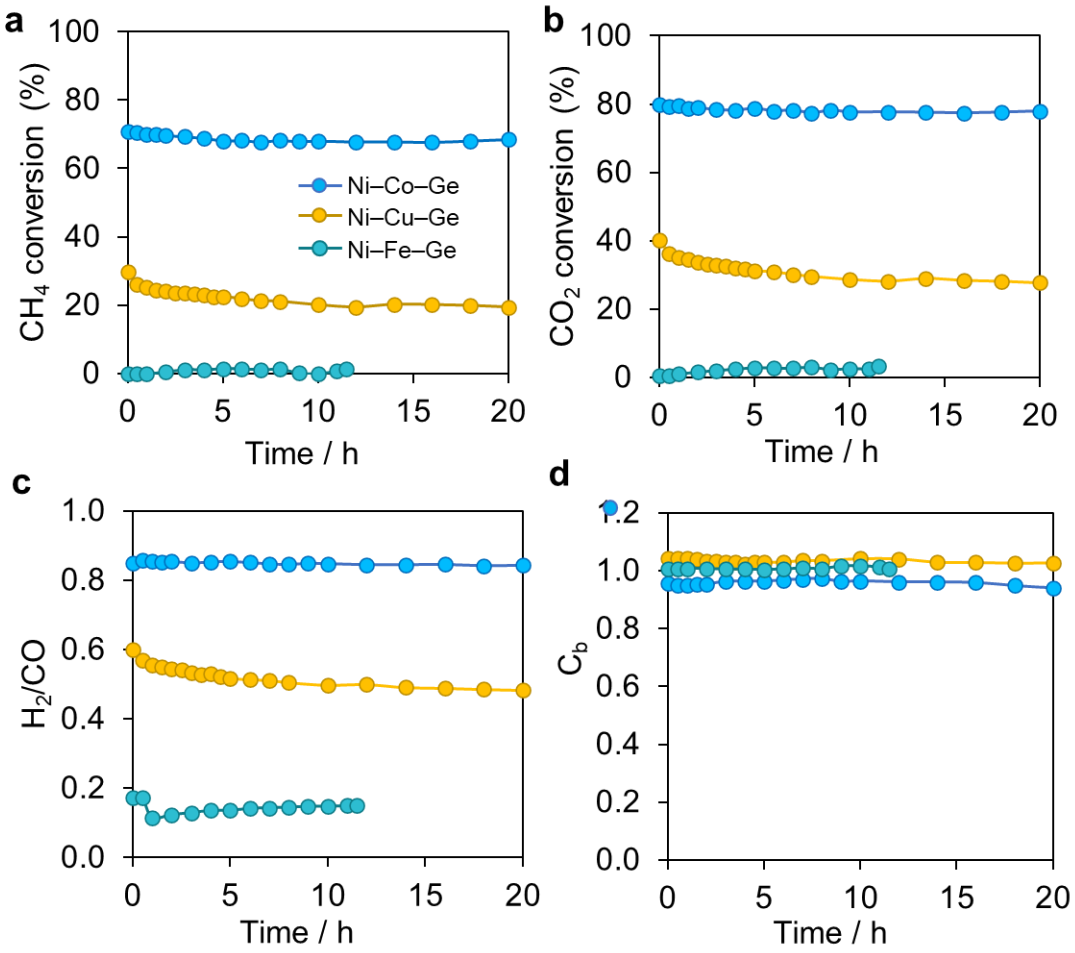

Figure 2.15. Catalytic performance of Ni–M–Ge/SiO_2 (M = Co, Cu and Fe) catalysts. (a) CH_4 conversion, (b) CO_2 conversion, (c) H_2/CO ratio, and (d) carbon balance. Reaction conditions: catalyst amount of 100 mg, CH_4:CO_2:Ar = 10:10:20 mL·min^{-1}, 700 ºC, 1 bar.

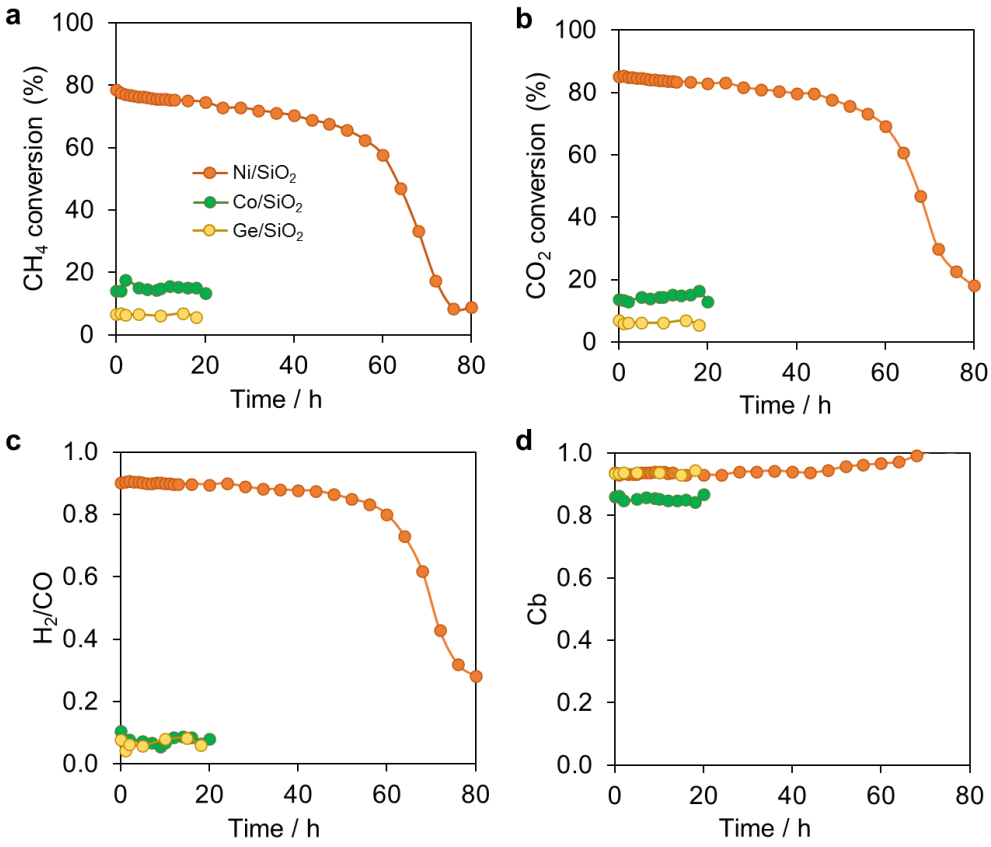

Figure 2.16. Catalytic activity of monometallic Ni/SiO_2, Co/SiO_2 and Ge/SiO_2 in DRM. (a) CH_4 conversion, (b) CO_2 conversion, (c) H_2/CO ratio, and (d) carbon balance. Reaction conditions: catalyst amount of 100 mg, CH_4:CO_2:Ar = 10:10:20 mL·min^{-1}, 700 °C, 1 bar.

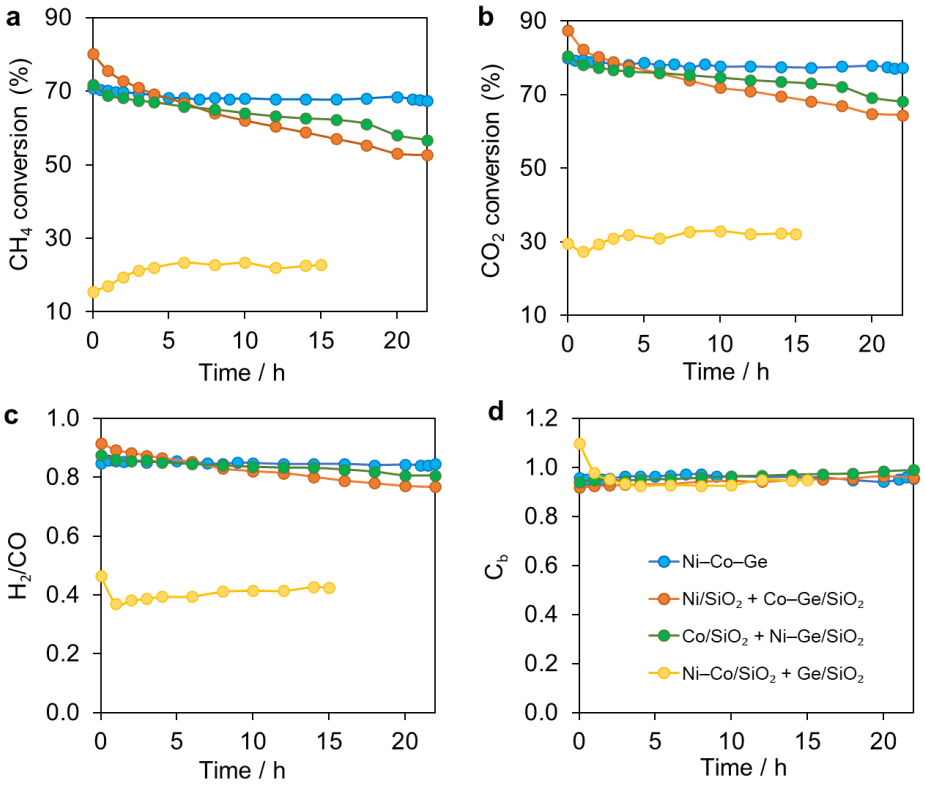

Figure 2.17. Catalytic performance of physical mixtures of Ni/SiO_2 + Co–Ge/ SiO_2, Ni–Ge/SiO_2 + Co/SiO_2, and Ni–Co/SiO_2 + Ge/SiO_2 compared with that of Ni–Co–Ge/SiO_2 in DRM. (a) CH_4 conversion, (b) CO_2 conversion (c) H_2/CO ratio and (d) carbon balance.

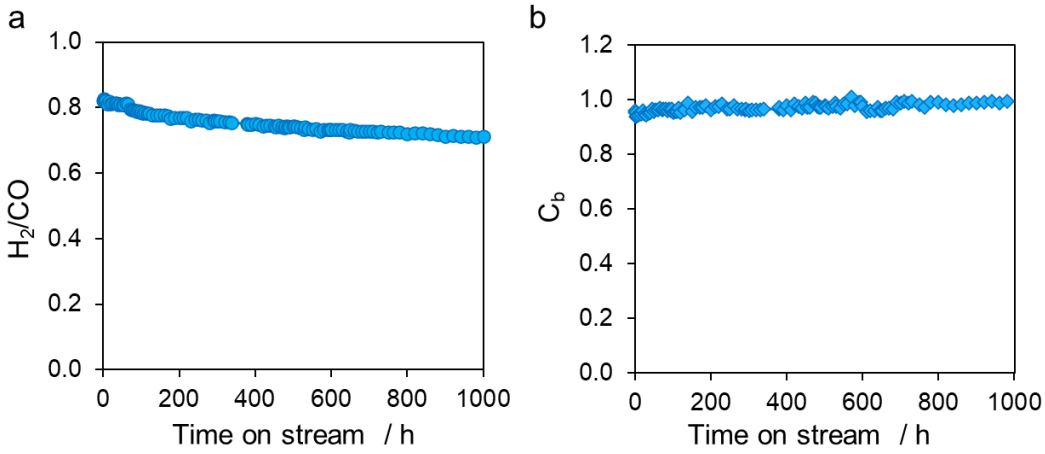

Figure 2.18. Long-term stability test of (a) H_2/CO ratio and (b) carbon balance over $(Ni_{0.5}Co_{0.5})_3Ge/SiO_2$ (Ni: 3 wt%). Reaction conditions: catalyst amount of 100 mg, CH_4:CO_2:Ar = 10:10:20 mL·min^{-1}, 700 °C, 1 bar.

Table 2.3. Summary of the catalytic performance of Ni–Co–Ge/SiO_2 and other reported Ni-based catalysts for DRM under equilibrium conversion.

No.	Catalyst	Temp. (°C)	GHSV L g^{-1} h^{-1}	Gas feed ratio	Equilibrium Conv. (%)		Stability	CH_4 Conv. (%)	CO_2 Conv. (%)	k_d (h^{-1}): CH_4	τ (h): CH_4	Regenerability	Ref.
					CH_4	CO_2							
1	Ni_3Ga/MgO	600	54	CH_4:CO_2:N_2 =1:1:1	45	58	72	50-46	52-48	0.002	442.8	–	[15]
2	Ni/MgO-Al_2O_3	600	30	CH_4:CO_2:N_2 =1:1:3	53	64	300	30-17	40-21	0.002	405.0	–	[30]
3	$NiCo/Al_2O_3$	600	144	CH_4:CO_2:N_2 =1:1:1	45	58	24	34-31	-	0.006	175.4	–	[31]
4	Na–Ni/ZrO_2	600	120	CH_4:CO_2:Ar = 68 : 31 :1	26	68	24	17-15	51-43	0.007	147.7	–	[32]
5	Ni/$Ce_{0.9}$ $Eu_{0.1}O_{1.95}$	600	60	CH_4:CO_2:N_2 =1:1:2	50	62	12	24-22	36-33	0.009	106.2	–	[33]
6	Ni/La_2O_3	650	240	CH_4:CO_2:N_2 =15:15:70	73	81	50	65-62	71-68	0.003	386.1	–	[34]
7	$Ni_3Fe_1Cu_1$-$Mg_xAl_yO_z$	650	120	CH_4:CO_2:N_2 =12:12:1	58	70	20	28-26	33-32	0.005	197.0	–	[35]
8	Ni@SBA-15	650	960	CH_4:CO_2:A_r =0.5:0.5:9	86	90	12	45-43	45-42	0.007	147.8	–	[36]
9	$NiFe/Al_2O_3$	650	600	CH_4:CO_2:N_2 =1:1:2	66	76	24	41-38	-	0.005	191.1	+	[37]
10	$(Ni_{0.5}Co_{0.5})_3Ge$ /SiO_2	700	24	CH_4:CO_2 =1:1	80	87	1000	60-41	71-54	0.00077	1299.7	+	This work
11	Ni–Ce–Al oxides	700	36	CH_4:CO_2 =1:1	72	82	80	70-67	-	0.002	546.3	–	[38]
12	NiCe@SBA–16	700	45	CH_4:CO_2:He =1:1:1	76	85	100	72-68	77-69	0.002	524.4	–	[39]
13	Ni/CeO_2-SiO_2	700	48	CH_4:CO_2:A_r= 1:1:2	80	87	50	78-76	88-87	0.002	442.5	–	[40]
14	Ni/La_2O_3	700	60	CH_4:CO_2:N_2 =15:15:70	84	90	50	74-70	82-75	0.004	251.7	–	[41]
15	Ni/MgO	700	-	CH_4:CO_2:A_r= 1:1:8	100	100	500	99-93	95-96	0.004	249.0	–	[12]
16	$NiMnMg/Al_2O_3$	700	12	CH_4:CO_2 =1:1	72	82	20	66-64	70-69	0.004	227.5	–	[42]
17	Ni/CeO_2/Al_2O_3	700	90	CH_4:CO_2:N_2 =1:1:1	78	85	60	55-40	62-43	0.010	99.0	–	[43]
18	Ni/CeO_2–ZrO_2	700	30	CH_4:CO_2 =1:1	72	82	24	51-38	52	0.022	45.3	–	[44]
19	Ni-TiN/SBA-15	700	1.558	CH_4:CO_2 =1:1	72	82	12	72-70	77-73	0.041	38.4	+	[45]
20	$NiSn/Al_2O_3$	700	60	CH_4:CO_2:N_2 =1:1:6	100	100	20	42-30	75-65	0.035	28.6	–	[46]

21	NiCo/γ–Al_2O_3–HY	700	-	CH_4:CO_2 =1:1	72	82	3	61-58	65-65	0.045	22.1	–	[47]
22	NiLa/ZrO_2	700	24	CH_4:CO_2 =1:1	72	82	5	70-59	74-70	0.097	10.3	–	[48]
23	NiCo/CeO_2	700	-	CH_4:CO_2:A_r= 1:1:3	82	88	5	78-65	79-72	0.129	7.7	–	[49]
24	Ni/Ca-HA1_S	700	15.8	CH_4:CO_2:N_2 =1:1:3	82	88	30	70-46	76-57	0.034	29.8	+	[50]
25	Ni/h-BN	750	60	CH_4:CO_2:N_2 =2:2:1	85	92	40	73-72	81-80	0.001	797.4	–	[51]
26	2Ni/HAP–Ce	750	60	CH_4:CO_2:He =1:1:3	90	94	100	90-84	97-94	0.005	183.7	–	[6]
27	NiMg/Al_2O_3	750	12	CH_4:CO_2:A_r= 1:1:3	90	94	50	90-87	95-93	0.006	168.8	–	[52]
28	Ni/Ce–La(Sm) –Cu–O	750	30	CH_4:CO_2:He =2:2:1	85	92	100	75-61	76-68	0.007	153.5	–	[53]
29	Ni nanotube @($T_{2.5}A_{1.5}$)m	750	144	CH_4:CO_2:N_2 =1:1:2	88	93	60	85-79	89-82	0.007	146.5	–	[54]
30	Ni@SiO_2	750	48	CH_4:CO_2:N_2 =1:1:2	88	93	24.5	60-54	73-66	0.011	91.8	–	[55]
31	Ni/$MgFe_x$ $Al_{2-x}O_4$	750	-	CH_4:CO_2:Ar =1:1:3	90	94	12	48-44	-	0.035	28.4	+	[56]
32	NiCoCe/Al_2O_3	750	24	CH_4:CO_2=1:1	83	90	5	68-37	-	0.257	3.9	+	[57]
33	Ni/ZrO_2	750	24	CH_4:CO_2=1:1	83	90	36	83-76	92-90	0.012	80.8	+	[58]
34	Ni/CeO_2–Al_2O_3	800	-	CH_4:CO_2 =1:1	90	95	72	79-69	89-81	0.008	129.6	–	[59]
35	NiCa/MCM–41	800	143	CH_4:CO_2:A_r= 1:1:1	92	96	20	62-57	50-43	0.011	91.5	–	[60]
36	NiGa/MCM–41	800	39	CH_4:CO_2:N_2 =30:30:5	91	95	30	88-82	91-86	0.016	63.0	–	[16]
37	NiW/SiO_2	800	96	CH_4:CO_2 =1:1	90	95	30	70-59	76-69	0.016	62.1	–	[61]
38	Ni/Al_2O_3–La_2O_3	800	180	CH_4:CO_2:N_2 =1:1:1	92	96	8	75-69	86-80	0.037	26.8	–	[62]
39	Ni/Al_2O_3–CeO_2	800	180	CH_4:CO_2:N_2 =1:1:1	92	96	8	90-84	93-89	0.067	14.8	–	[62]
40	Ni/$MgAlO_x$	800	1440	CH_4:CO_2:Ar =8:10:7	98	88	20	52-48	-	0.008	118.7	+	[63]
41	AlSB/MgO@Ni	800	97 000 h^{-1}	CH_4:CO_2:N_2 =3:6:1	99	69	27	35-9	33-7.8	0.068	14.6	Δ	[64]
42	NiCeLa/MgO-Al_2O_3	800	1700 h^{-1}	CH_4:CO_2 =1:1	90	95	76	95-94	92-85	0.003	394.0	Δ	[65]

– (no data) Δ (not recovered or stable) + (recovered & stable)

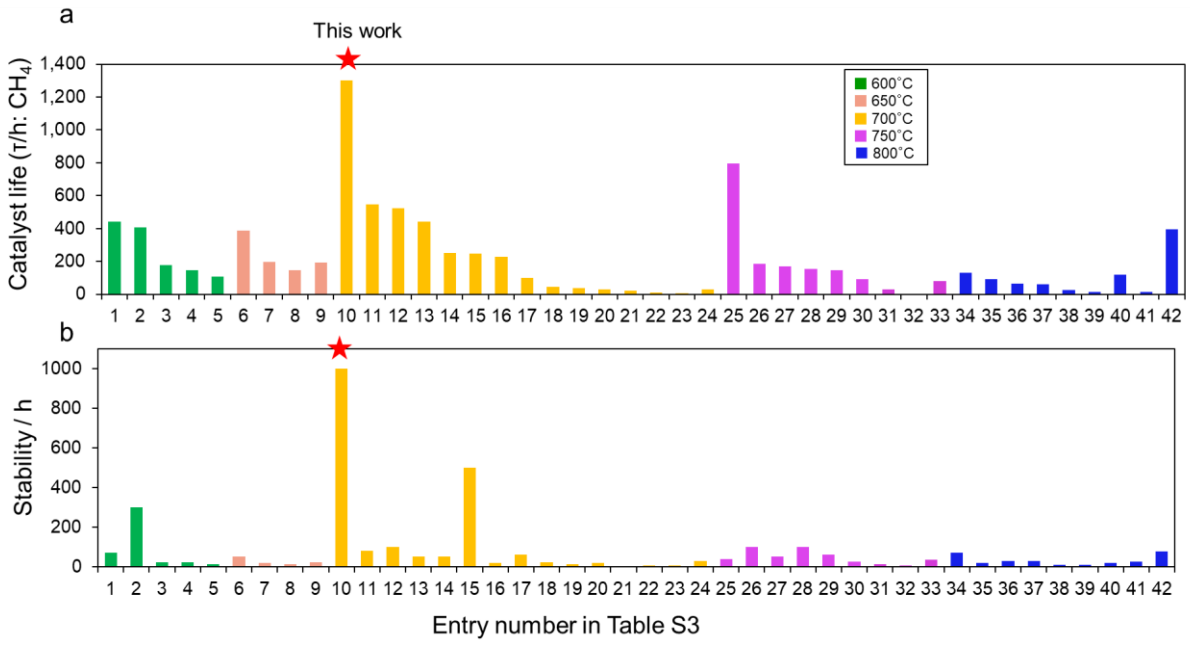

Figure 2.19. Catalytic performance of $(Ni_{0.5}Co_{0.5})_3Ge/SiO_2$ and reported Ni-based systems for DRM under equilibrium conversion. (a) Mean catalyst life ($\tau = k_d^{-1}$), (b) Stability time.

Table 2.4. Comparison of catalytic performance in DRM with those of reported Ni-based catalysts obtained at thermodynamic equilibrium and showing a positive k_d value.

No.	Catalyst	Temp. (°C)	GHSV (F/M) L g^{-1} h^{-1}	Feed gas ratio	equilibrium Conv. (%)		operation time (h)	CH4 Conv. (%)	CO2 Conv. (%)	equilibrium	kd (h^{-1}) (CH_4)	τ (h) (CH_4)	Regenerability	Ref.
					CH_4	**CO_2**								
1	$(Ni_{0.5}Co_{0.5})_3Ge/SiO_2$	700	24	CH_4:CO_2: A_r=1:1:2	80	87	1000	60-41	71-54	< eq	0.00077	1299.7	+	this work
2	Ni/silica	600	60	CH_4:CO_2: He=1:1:1	46	58	100	54-47	58-50	@ eq	0.00280	356.5	-	[66]
3	LaSrNiCuO	650	-	CH_4:CO_2: N_2=1:1:1	62	74	24	83-67	82-57	@ eq	0.03656	27.4	-	[67]
4	$Co/Ni/Al_2O_3$	650	12	CH_4:CO_2= 1:1	58	70	72	71-63	75-66	@ eq	0.00504	198.3	-	[68]
5	NiCu /SBA-15	650	10000 h^{-1}	CH_4:CO_2= 1:1	58	70	6	75-74	77-76	@ eq	0.01053	95.0	-	[69]
6	Ni/MCM-41	700	45	CH_4:CO_2= 1:1	72	82	200	72-68	82-78	@ eq	0.00095	1048.8	-	[70]
7	NiCoSr/γ-Al_2O_3	700	3.6	CH_4:CO_2: N_2=17:17: 2	73	83	7.5	85-83	82.3-80.6	@ eq	0.02128	47.0	-	[71]
8	Ni/Ce-SBA-15	700	36	CH_4:CO_2= 1:1	72	82	40	77-73	77-74	@ eq	0.00594	168.5	-	[72]
9	Ni-Ce/W-Zr	700	42	CH_4:CO_2: N_2=3:3:1	74	83	100	82-72	88-83	@ eq	0.00578	173.1	-	[73]
10	Ni/silica	750	60	CH_4:CO_2: He=1:1:1	86	92	100	91-89	85-83	@ eq	0.00223	448.6	-	[66]
11	NiMgAlCe	750	15	CH_4:CO_2= 1:1	83	90	20	88-86	95-95	@ eq	0.00886	112.9	-	[74]
12	$NiCo/CeO_2$	800	12	CH_4:CO_2: N_2=3:3:4	93	96	10	99-80	99-81	@ eq	0.32088	3.1	-	[75]
13	$NiCe/SiO_2$	800	12	CH_4:CO_2= 1:1	90	95	30	91.3-89.5	95.6-94.6	@ eq	0.00717	139.4	-	[76]
14	$In0.5Ni@SiO_2$	800	18	CH_4:CO_2= 1:1	90	95	430	90-88	95-92	@ eq	0.00048	2099.7	-	[14]
15	Ni−yolk@Ni @SiO_2	800	40	CH_4:CO_2: N_2=1:1:1	92	96	90	96-89	97-95	@ eq	0.01208	82.8	-	[77]

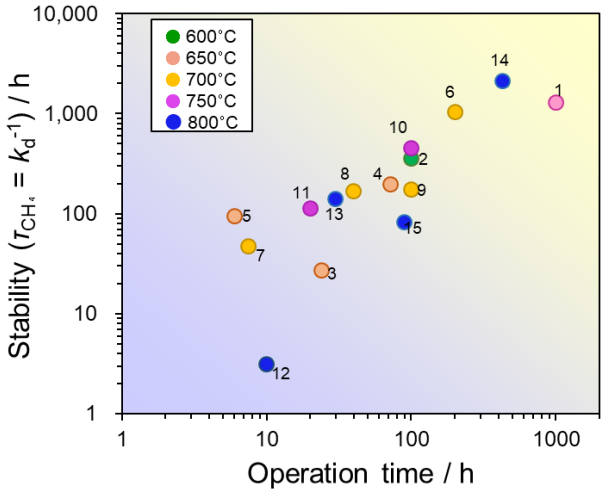

Figure 2.20 Comparison of the stability with those of reported Ni-based DRM catalysts reach/exceed equilibrium conversion. Numbers correspond to the entries in Table S4.

Table 2.5. Comparison of catalytic performance in DRM with those of reported Ni-based catalysts showing a negative k_d value and/or no deactivation at thermodynamic equilibrium.

No.	Catalyst	Temp. (ºC)	GHSV (F/M) L g^{-1} h^{-1}	Feed gas ratio	equilibrium Conv. (%)		total time (h)	CH_4 Conv. (%)	CO_2 Conv. (%)	equili-brium	kd (h^{-1}) (CH4)	Regene rability	Ref
					CH_4	CO_2							
1	$(Ni_{0.5}Co_{0.5})_3Ge/SiO_2$	700	24	CH_4:CO_2: Ar=1:1:2	80	87	1000	60-41	71-54	< eq	0.00077	+	this work
2	NiCu/Mg(Al)O	600	60	CH_4:CO_2: N_2=1:1:2	50	62	25	50-51	58-57	@ eq	< 0	-	[7]
3	$Ni_{0.2}Co0.3$@S-2	650	100	CH_4:CO_2: N_2=2:2:1	60	82	100	-	-	-	-	-	[10]
4	Ni/Al_2O_3	700	22000 h^{-1}	CH_4:CO_2 =1:1	72	82	9	91-98	70-50	@ eq	< 0	-	[78]
5	NiCoCu/γ-Al_2O_3	700	12	CH_4:CO_2 =1:1	72	82	5	25-30	35-43	< eq	< 0	-	[79]
6	NiMo/ZSM-5	750	50	CH_4:CO_2 =1:1	83	90	20	-	-	-	-	-	[80]
7	Ni/ZrO_2@BN	750	25	CH_4:CO_2 =1:1	83	90	200	68-71	77-80	< eq	< 0	-	[81]
8	$NiCo/SiO_2$	750	60	CH_4:CO_2: He=1:1:1	86	92	100	84-84	87-87	@ eq	0	-	[82]
9	Ni–Mg–Al LDH	750	60	CH_4:CO_2: N_2 = 1:1:2	88	93	30	86-86	92-92	@ eq	0	-	[83]
10	NiCo	750	110	CH_4:CO_2: N_2=1:1:1	86	92	2000	90-90	-	@ eq	0	-	[84]

11	Ni–Co/MgO–ZrO_2	750	126	CH_4:CO_2:N_2=1:1:1	86	92	40	75-80	80-84	< eq	< 0	+	[85]
12	NiO/MgO	800	20	CH_4:CO_2 =1:1	90	95	5	85-93	90-94	< eq	< 0	-	[86]
13	Ni/MgO-Al_2O_3	800	20	CH_4:CO_2:N_2=1:1:3	94	97	300	71-80	72-81	< eq	< 0	-	[30]
14	NiMo/MgO	800	60	CH_4:CO_2:He=1:1:8	97	98	850	100-100	100-100	@ eq	0	-	[87]
15	NiMo/SBA-15	800	4	CH_4:CO_2 =1:1	90	95	600	94-94	-	@ eq	0	-	[88]
16	NiCoMnCe/ZrO_2	800	243000 h^{-1}	CH_4:CO_2:O_2=1: 0.8: 0.2	96	88	24	100-100	95.5-95.5	@ eq	0	-	[89]
17	NiCoMgAl oxide	800	32000 h-1	CH_4/CO_2/Ar=1:1:3	94	97	20	96-96	92.5-92.5	@ eq	0	-	[90]
18	$LaNi_{0.34}Co_{0.33}Mn_{0.33}O_3$	800	12	CH_4:CO_2:N_2 = 1:1.05:1	94	94	14	94-94	89-90	@ eq	0	-	[91]

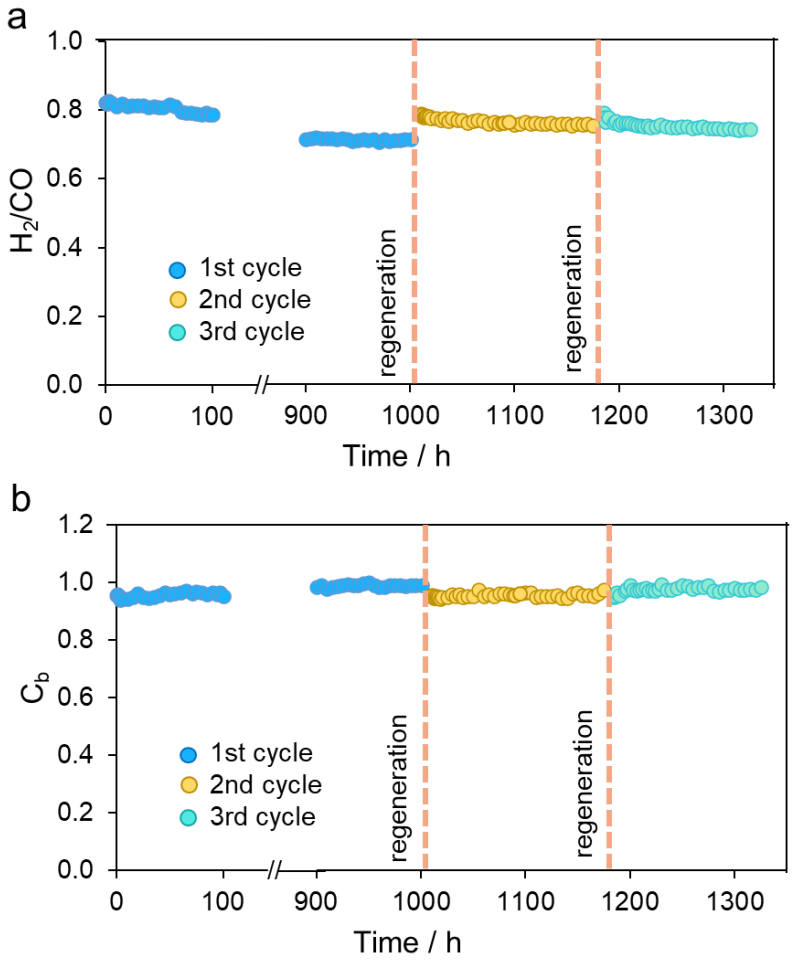

Figure 2.21. Time course of (a) H_2/CO ratio and (b) carbon balance over $(Ni_{0.5}Co_{0.5})_3Ge/SiO_2$ for DRM with catalyst regeneration.

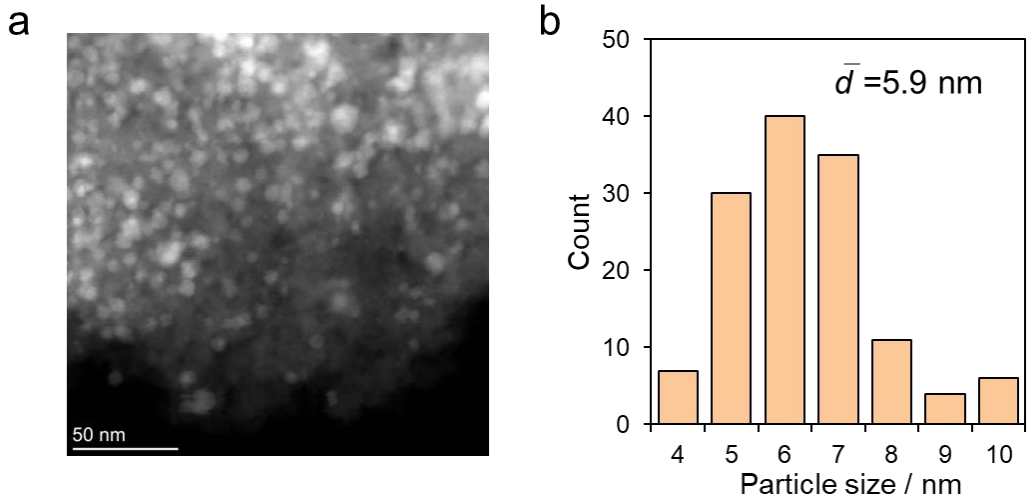

Figure 2.22. (a) STEM image and (b) particle size distribution of spent $(Ni_{0.5}Co_{0.5})_3Ge/SiO_2$ after 88 h catalytic run.

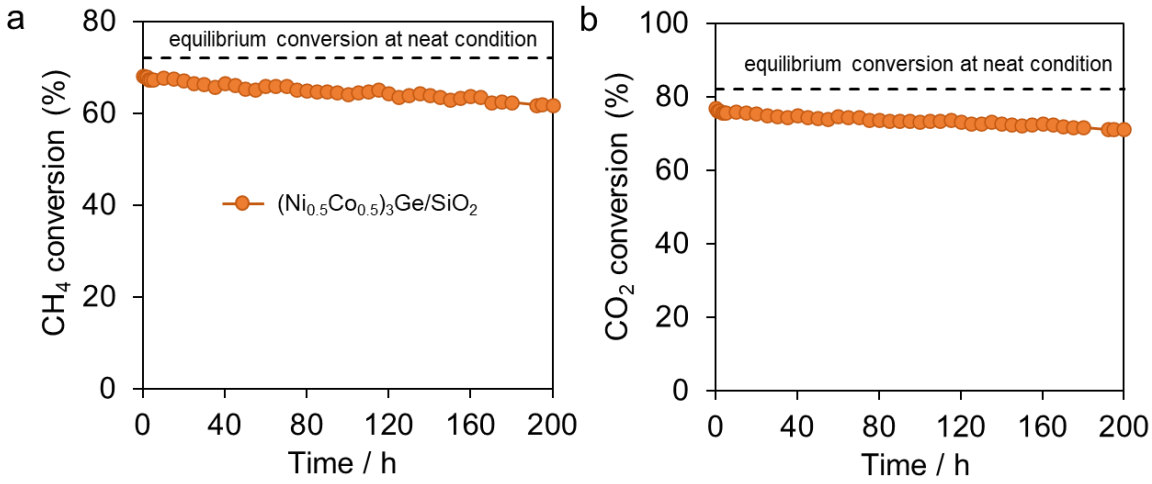

Figure 2.23. Long-term stability of (a) CH_4 conversion, (b) CO_2 conversion over $(Ni_{0.5}Co_{0.5})_3Ge/SiO_2$ at neat condition. Reaction condition: catalyst amount of 100 mg, CH_4:CO_2 = 10:10 mL min^{-1}, 700 °C, 1 bar.

2.3.3 The origin of the coke resistance of $(Ni_{0.5}Co_{0.5})_3Ge/SiO_2$ in DRM

Next, we conducted mechanistic studies to understand the activity trend and the origin of the excellent stability of $(Ni_{0.5}Co_{0.5})_3Ge/SiO_2$. First, we investigated the behavior of coke on

the spent catalyst. After 20 h of the catalytic run, the spent catalysts were analyzed by temperature-programmed oxidation (O_2-TPO, Figure 2.24a) and Raman spectroscopy. The spent Ni_3Ge showed an intense evolution of CO_2 at 744°C, which is assignable to combustion of graphitic carbon. On the contrary, $(Ni_{0.5}Co_{0.5})_3Ge$ showed little coke combustion, which reflects the significantly improved coke resistance by Co-doping and is consistent with the much greater stability of $(Ni_{0.5}Co_{0.5})_3Ge$ in DRM. The Raman analysis revealed that the spent Ni_3Ge showed the two peaks assignable to G and D band of coke with the intensity ratio of approximately 0.5 (Figure 2.25). The ratio lower than unity suggests the formation of only soft coke;[24] therefore, the growth of hard coke has been prevented due to the ensemble effect of Ge. The accumulation of soft coke is also consistent with gradual deactivation. Conversely, no signal was observed for $(Ni_{0.5}Co_{0.5})_3Ge$, indicating that even the formation of soft coke was inhibited by Co doping. These are also consistent with the results of O_2–TPO and the stability trend. Besides, the XRD patterns (peak position and width) and the XAFS spectra (XANES and EXAFS features) of the two catalysts did not little change after the long-term DRM reaction (Figure 2.26 and Figure 2.27), confirming that the alloy and Co-doped structures were retained even after the reaction and deactivation. These results indicate that the deactivation of Ni_3Ge/SiO_2 was induced simply by coke accumulation on the catalyst, but not by sintering or segregation of the alloy phase. Then, we determined the reaction orders with respect to the partial pressures of CH_4 and CO_2 (P_{CH4} and P_{CO2}, respectively), revealing the first-order dependence on P_{CH4}, while much lower reaction orders were obtained for P_{CO2} (Figure 2.24b and 3c). This result indicates that the C−H activation of CH_4 is the rate-determining step. For P_{CO2}, Ni_3Ge showed a negative reaction order of –0.3, suggesting that CO_2 adsorption on Ni sites competes with CH_4 adsorption. Conversely, $(Ni_{0.5}Co_{0.5})_3Ge$ showed a positive order of 0.4, which implies that the competitive adsorption was eliminated by Co doping. A possible interpretation of this change is that the doped Co acts as an effective CO_2 adsorption site. This

may also have enhanced CO_2 activation, thus serving more oxygen atoms for facile coke combustion. Apparent activation energies (E_a) in DRM were also estimated for each catalyst using Arrhenius-type plots (Figure 2.28). E_a of CH_4 activation on Ni_3Ge was 51 kJ mol^{-1}, whereas that on Co_3Ge was 108 kJ mol^{-1}, which indicates the intrinsic lower ability of Co than Ni for C–H activation and is consistent finely with the experimental activity trend. $(Ni_{0.5}Co_{0.5})_3Ge/SiO_2$ showed an intermediate E_a of 89 kJ mol^{-1}, suggesting that the C–H activating ability was moderately tuned.

Based on the experimental results, the effects of alloying/doping on the enhanced coke tolerance may be summarized as follows: (1) alloying with Ge significantly suppresses coke formation (Ni_3Ge vs. Ni and $Ni_{0.5}Co_{0.5}$) and (2) Co-doping enhances coke removal by accelerating CO_2 adsorption/activation and the resulting oxygen supply.[68, 75] Figure 2.24d shows the reaction pathway of DRM, in which three reaction pathways from CH_4 to CO have been known, i.e., those through the (A) CHO, (B) C, and (C) COH intermediates. Since only the pass (A) does not form carbon atoms among them, facilitating this step should suppress coke formation and accumulation. Besides, enhancing oxygen supply further accelerates path (A) and (B), thus suppressing coke accumulation.

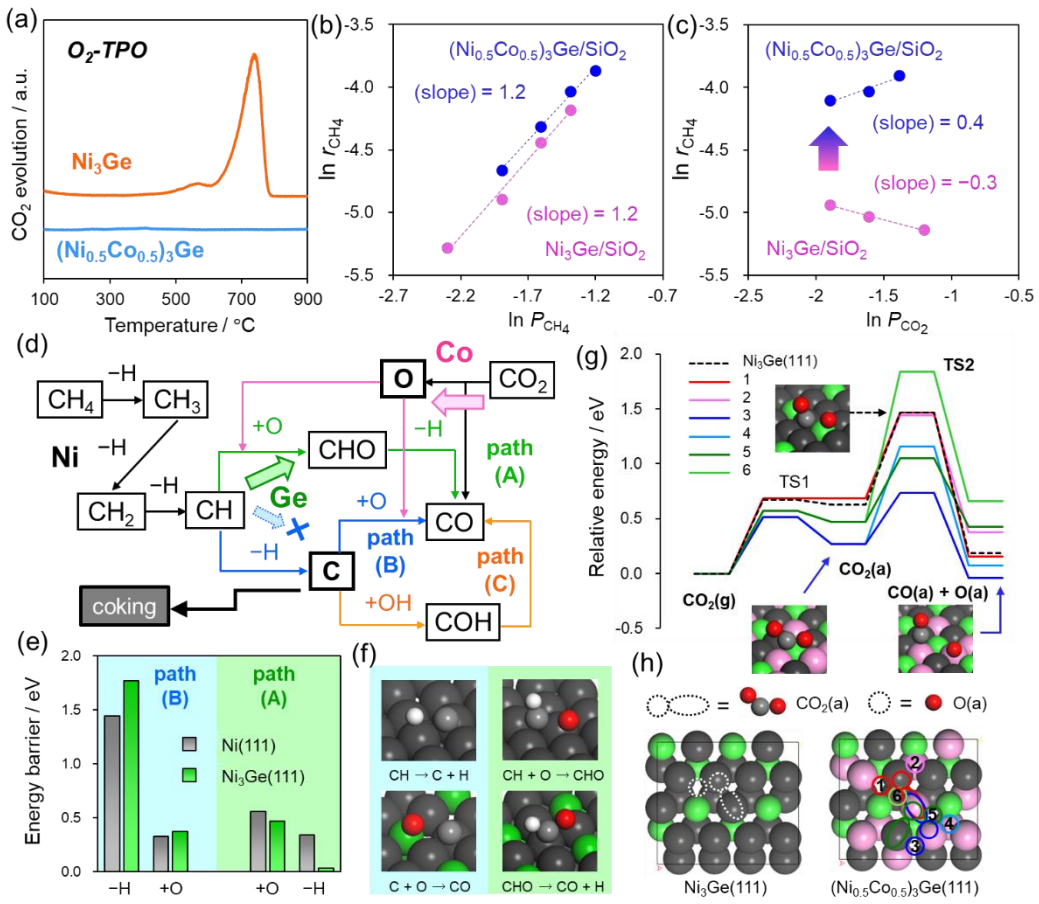

Figure 2.24. Mechanistic study. (a) O_2–TPD profiles for Ni_3Ge/SiO_2 and $(Ni_{0.5}Co_{0.5})_3Ge/SiO_2$ used in DRM for 20 h. Reaction orders on the partial pressure of (b) CH_4 and (c) CO_2. (d) Reaction routes from methane and CO_2 to CO in DRM. (e) DFT-calculated E_a of CH decomposition and CH+O reactions over $Ni_3Ge(211)$ step sites and the Co-doped analogs. The inset figures depict the transition states (gray: Ni, pink: Co, green: Ge, light gray: C, red: O, and white: H).

2.3.4 DFT calculation

Finally, we performed density functional theory (DFT) calculations to understand more deeply the roles of Ge and Co on the reaction pathways (A) and (B). The C–H scission of CH to form C and H atoms (CH → C + H) and the subsequent oxygenation to form CO (C + O →

CO) were considered on Ni(111) and Ni_3Ge(111) surfaces for path (B) (Figure 2.24e, f). Conversely, oxygenation of CH to form CHO (CH + O → CHO) followed by the H elimination to CO (CHO → CO + H) were considered for path (A). The C–H scission of CH had much higher energy barriers than other steps, indicating that path (A) is minor in this reaction system. This suggests that although carbon formation is a rare event, its growth for coke accumulation eventually deactivates the catalyst. –When comparing Ni(111) and Ni_3Ge(111), the latter showed higher barrier of the C–H scission of CH, whereas lower barriers of path (A), indicating that Ge suppresses path (B), while facilitates path (A). Therefore, carbon formation is further prevented by alloying with Ge. Then, we focused on the role of Co for CO_2 adsorption and activation. We randomly replaced half of Ni atoms in the Ni_3Ge(111) slab to construct $(Ni_{0.5}Co_{0.5})_3Ge$(111) surface. Since this surface has various metal–metal ensemble sites (i.e., $Ni_xCo_yGe_z$, $x, y, z = 0–2$), several possible adsorption/activation configurations were considered (Figure 2.24g, h; 1–6, see Figure 2.29 and Figure 2.30 for details). Bidentate CO_2 with an sp^2-like bended structure was considered as an adsorbate (CO_2(a)) because this has been known as a chemisorbed species on transition metal surfaces.[18, 92] The order of adsorption energy was as follows: Ni_3Ge (Ni–C–O–Ni) ~ 1,2 (Co–C–O–Ni) > 5,6 (Ni–C–O–Co) >> 3,4 (Co–C–O–Co). Notably, the adsorption with Co–O bonding resulted in lower adsorption energy, demonstrating that Co acts as an efficient adsorption site of CO_2, probably due to the intrinsic oxophilicity of Co. For the subsequent C–O cleavage, the reactions occurring at the Co sites provided much lower energy barriers and transition state (TS) energies (Figure 2.24g; 3, 4, and 5). Therefore, the doped Co not only stabilizes CO_2 adsorption, but also promotes its activation process to release oxygen atoms. For the optimized catalyst, the EXAFS analysis suggested that the surface was slightly Co-rich. Therefore, the probability of oxygen supply from CO_2 for coke removal seems to be also high. Thus, our DFT calculation well supported the reaction

mechanism derived from the experimental suggestions and clarified the roles of Ge and Co alloying on catalysis.

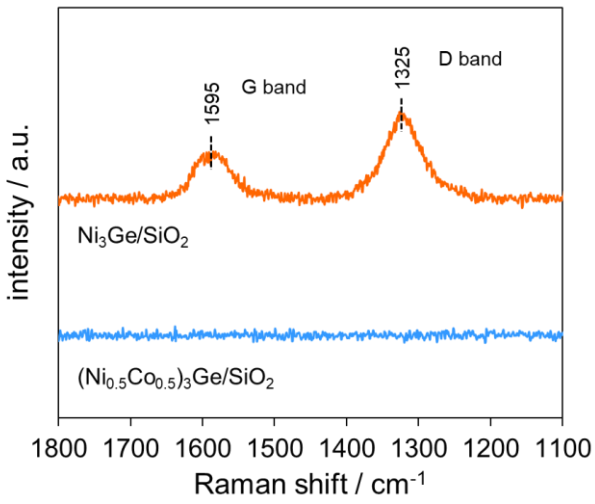

Figure 2.25. Raman spectra of the spent Ni_3Ge/SiO_2 and $(Ni_{0.5}Co_{0.5})_3Ge/SiO_2$ used in DRM for 20 h.

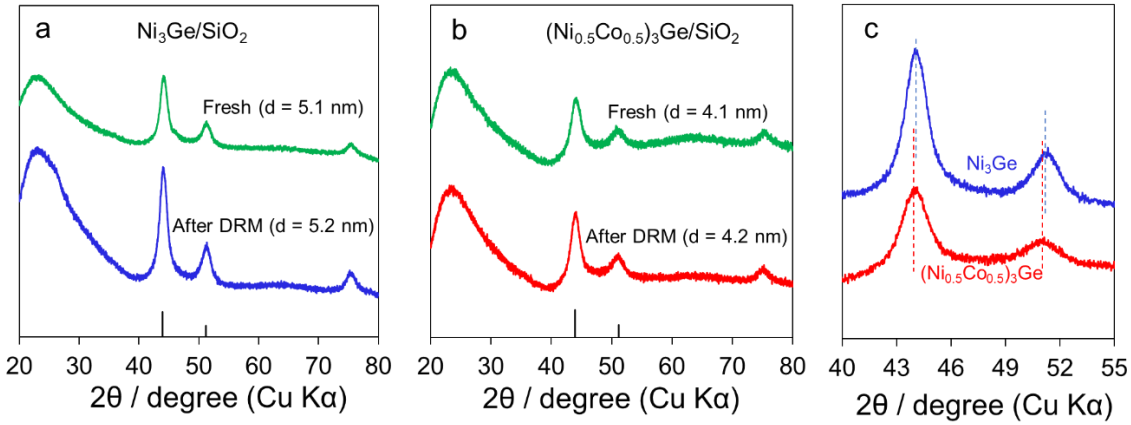

Figure 2.26. XRD patterns of the fresh and spent (700ºC, 75 h) over (a) Ni_3Ge/SiO_2, (b) $(Ni_{0.5}Co_{0.5})_3Ge/SiO_2$ catalyst and (c) the comparison of spent Ni_3Ge/SiO_2 and $(Ni_{0.5}Co_{0.5})_3Ge/SiO_2$ catalysts. The particles size was calculated by Scherrer formula.

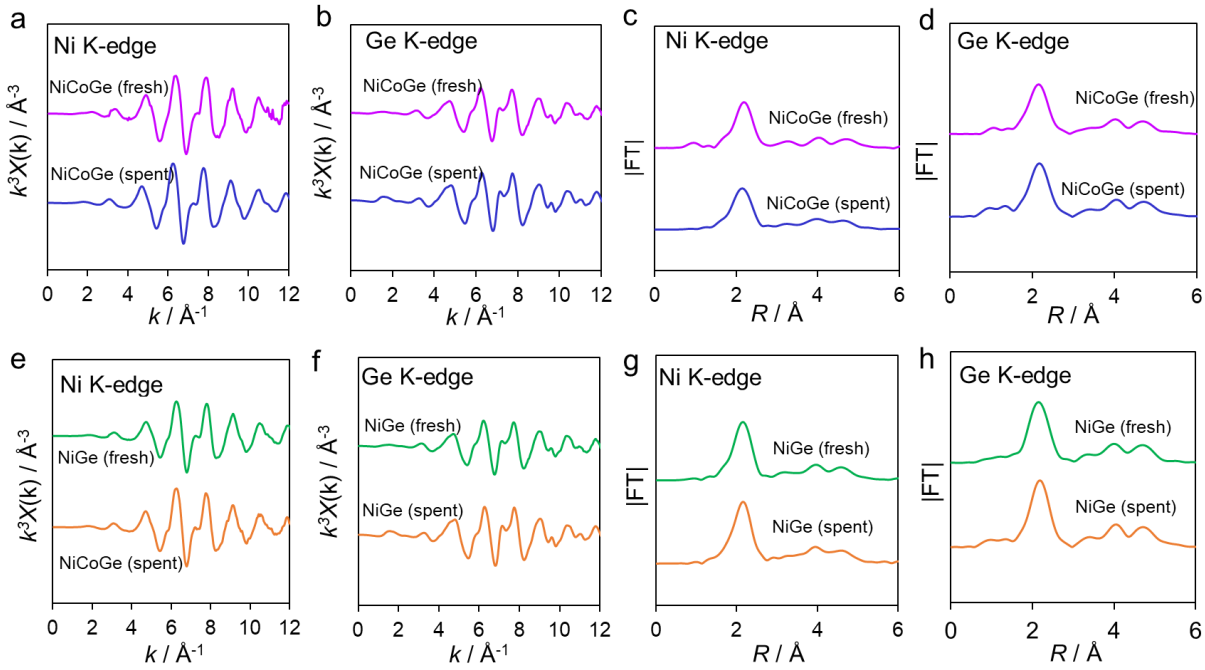

Figure 2.27. (a, e) Ni K- and (b, f) Ge K-edge k^3-weighted raw EXAFS oscillations for fresh and spent (a, b) $(Ni_{0.5}Co_{0.5})_3Ge/SiO_2$ and (e, f) Ni_3Ge/SiO_2 catalysts. Fourier transforms of the Ni (c, g) K- and (d, h) Ge K-edge k^3-weighted EXAFS spectra of fresh and spent (c, d) $(Ni_{0.5}Co_{0.5})_3Ge/SiO_2$ and (g, h) Ni_3Ge/SiO_2 catalysts.

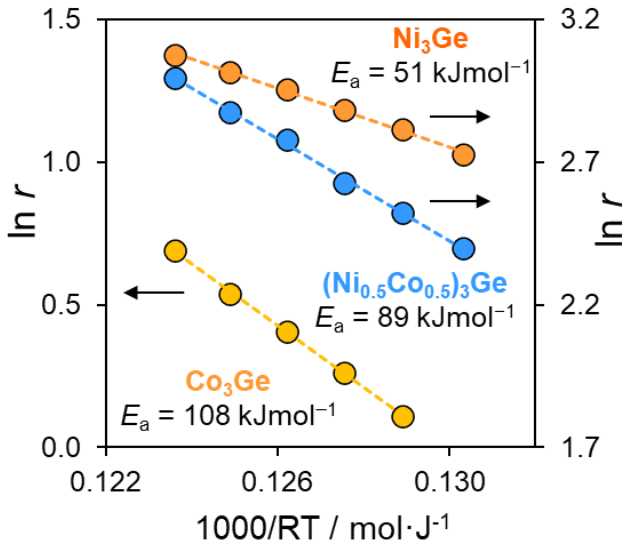

Figure 2.28. Arrhenius-type plots obtained in DRM over Ni_3Ge/SiO_2, Co_3Ge/SiO_2, and $(Ni_{0.5}Co_{0.5})_3Ge/SiO_2$.

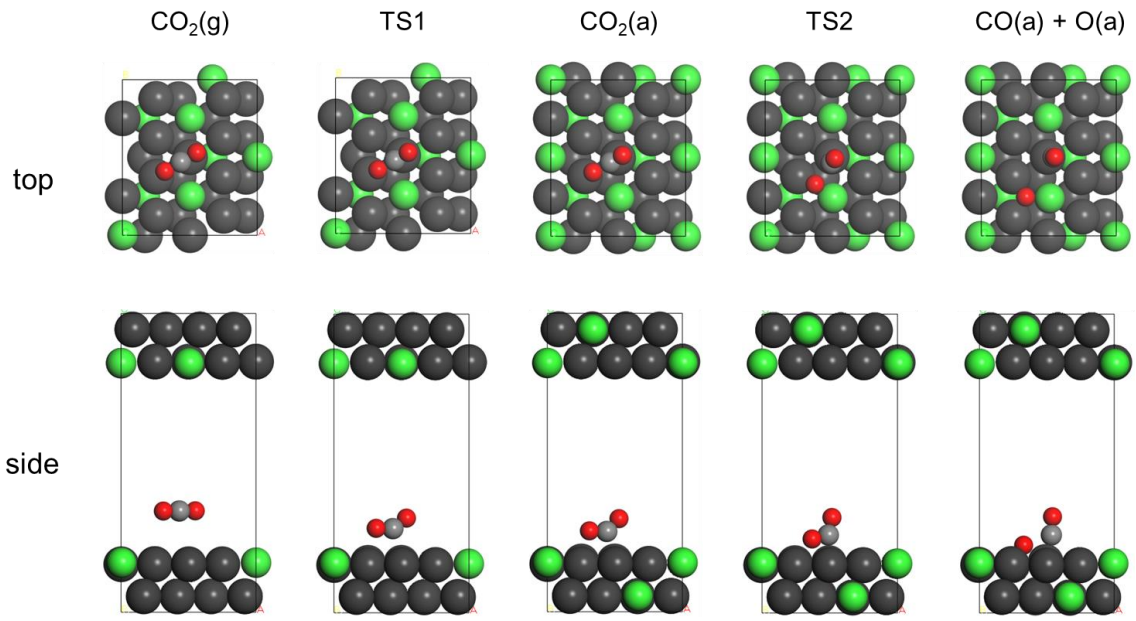

Figure 2.29. DFT-calculated structures for CO_2 adsorption and activation on $Ni_3Ge(111)$ surface.

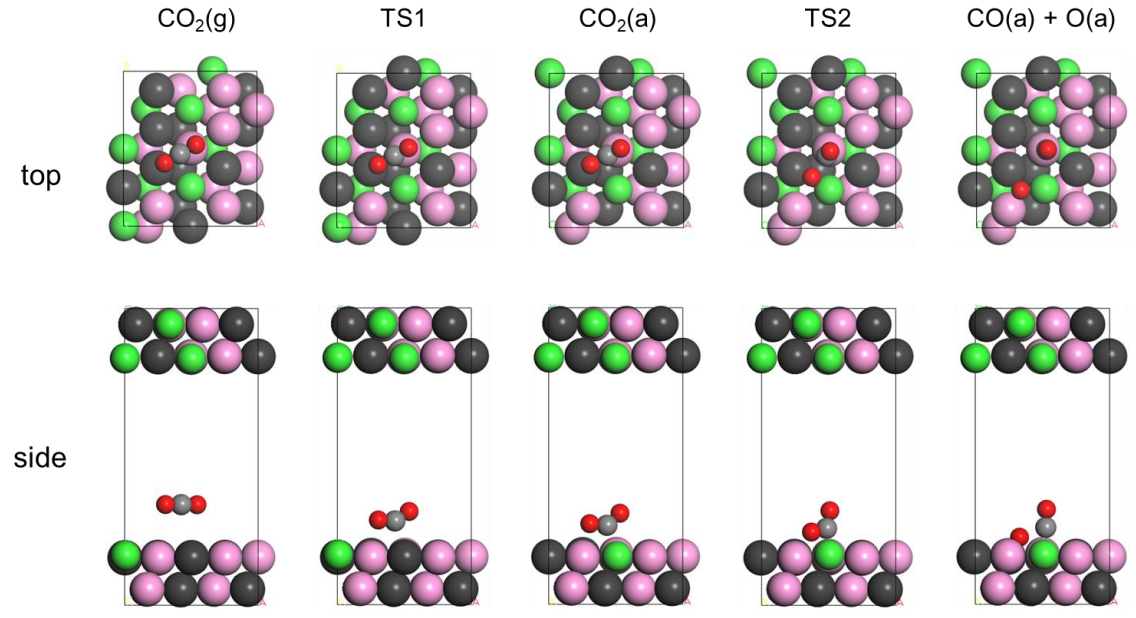

Figure 2.30. DFT-calculated structures for CO_2 adsorption and activation on $(Ni_{0.5}Co_{0.5})_3Ge(111)$ surface. Structures of configuration 3 shown in Fig. 3h are shown as representative.

2.4 Conclusion

In this study, we designed and synthesized a $(Ni_{0.5}Co_{0.5})_3Ge/SiO_2$ ternary catalyst highly efficient for DRM. Substituting a part of Ni in the intermetallic Ni_3Ge with Co formed a pseudo-binary alloy structure of $(Ni_{0.5}Co_{0.5})_3Ge$, which was confirmed by the combination of XRD, XAFS, and HAADF–STEM–EDX analyses. The $(Ni_{0.5}Co_{0.5})_3Ge/SiO_2$ catalyst exhibited a remarkably high coke resistance at 700°C and an outstandingly long catalyst life (operation: 1000 h, τ = 1300 h), as well as excellent renewability and reusability with almost full recovery of the initial catalytic performance. Notably, the outstandingly high catalytic performance can be achieved at conversions below the thermodynamic equilibrium for the first time. Alloying Ni with Ge not only inhibits carbon formation, i.e., the origin of coke accumulation, but also promotes CO formation via the CHO intermediate without forming carbon. The dopant Co acts as an efficient site for CO_2 adsorption and activation, which supplies more oxygen atoms to promote carbon combustion. The combination of Ge and Co allows to minimize the coke accumulation, thus achieving outstandingly high stability for long-term operation. The results obtained in this study provide a highly efficient catalyst for converting CO_2 and natural gas and propose an effective catalyst design concept for durable and coke-resistant catalysis for hydrocarbon chemistry.

Reference

1. Joo, S.; Kim, K.; Kwon, O.; Oh, J.; Kim, H. J.; Zhang, L.; Zhou, J.; Wang, J.-Q.; Jeong, H. Y.; Han, J. W.; Kim, G., Enhancing Thermocatalytic Activities by Upshifting the d-Band Center of Exsolved Co-Ni-Fe Ternary Alloy Nanoparticles for the Dry Reforming of Methane. *Angew. Chem., Int. Ed.* **2021,** *60*, 15912-15919.

2. Tian, S.; Yan, F.; Zhang, Z.; Jiang, J., Calcium-looping reforming of methane realizes in situ CO_2 utilization with improved energy efficiency. *Sci. Adv.* **2019,** *5*, eaav5077.

3. Davis Steven, J.; Lewis Nathan, S.; Shaner, M.; Aggarwal, S.; Arent, D.; Azevedo Inês, L.; Benson Sally, M.; Bradley, T.; Brouwer, J.; Chiang, Y.-M.; Clack Christopher, T. M.; Cohen, A.; Doig, S.; Edmonds, J.; Fennell, P.; Field Christopher, B.; Hannegan, B.; Hodge, B.-M.; Hoffert Martin, I.; Ingersoll, E.; Jaramillo, P.; Lackner Klaus, S.; Mach Katharine, J.; Mastrandrea, M.; Ogden, J.; Peterson Per, F.; Sanchez Daniel, L.; Sperling, D.; Stagner, J.; Trancik Jessika, E.; Yang, C.-J.; Caldeira, K., Net-zero emissions energy systems. *Science* **2018,** *360*, eaas9793.

4. Liu, Z.; Grinter, D. C.; Lustemberg, P. G.; Nguyen-Phan, T.-D.; Zhou, Y.; Luo, S.; Waluyo, I.; Crumlin, E. J.; Stacchiola, D. J.; Zhou, J.; Carrasco, J.; Busnengo, H. F.; Ganduglia-Pirovano, M. V.; Senanayake, S. D.; Rodriguez, J. A., Dry Reforming of Methane on a Highly-Active Ni-CeO_2 Catalyst: Effects of Metal-Support Interactions on C−H Bond Breaking. *Angew. Chem., Int. Ed.* **2016,** *55*, 7455-7459.

5. De, S.; Zhang, J.; Luque, R.; Yan, N., Ni-based bimetallic heterogeneous catalysts for energy and environmental applications. *Energy Environ. Sci.* **2016,** *9*, 3314-3347.

6. Akri, M.; Zhao, S.; Li, X.; Zang, K.; Lee, A. F.; Isaacs, M. A.; Xi, W.; Gangarajula, Y.; Luo, J.; Ren, Y.; Cui, Y. T.; Li, L.; Su, Y.; Pan, X.; Wen, W.; Pan, Y.; Wilson, K.; Li, L.; Qiao, B.; Ishii, H.; Liao, Y. F.; Wang, A.; Wang, X.; Zhang, T., Atomically dispersed nickel as coke-resistant active sites for methane dry reforming. *Nat. Commun.* **2019,** *10*, 5181.

7. Song, K.; Lu, M.; Xu, S.; Chen, C.; Zhan, Y.; Li, D.; Au, C.; Jiang, L.; Tomishige, K., Effect of alloy composition on catalytic performance and coke-resistance property of Ni-Cu/Mg(Al)O catalysts for dry reforming of methane. *Appl. Catal. B: Environ.* **2018,** *239*, 324-333.

8. Song, Y.; Ozdemir, E.; Ramesh, S.; Adishev, A.; Subramanian, S.; Harale, A.; Albuali, M.; Fadhel, B. A.; Jamal, A.; Moon, D.; Choi, S. H.; Yavuz, C. T., Dry reforming of methane by stable Ni–Mo nanocatalysts on single-crystalline MgO. *Science* **2020,** *367*, 777-781.

9. Yusuf, M.; Farooqi, A. S.; Keong, L. K.; Hellgardt, K.; Abdullah, B., Contemporary trends in composite Ni-based catalysts for CO_2 reforming of methane. *Chem. Eng. Sci.* **2021,** *229*. No. 116072.

10. Wang, J.; Fu, Y.; Kong, W.; Li, S.; Yuan, C.; Bai, J.; Chen, X.; Zhang, J.; Sun, Y., Investigation of Atom-Level Reaction Kinetics of Carbon-Resistant Bimetallic NiCo-Reforming Catalysts: Combining Microkinetic Modeling and Density Functional Theory. *ACS Catal.* **2022**, *12*, 4382-4393.

11. Paksoy, A. I.; Caglayan, B. S.; Aksoylu, A. E., A study on characterization and methane dry reforming performance of Co–Ce/ZrO_2 catalyst. *Appl. Catal. B: Environ.* **2015,** *168*, 164-174.

12. Cheng, F.; Duan, X.; Xie, K., Dry Reforming of CH_4/CO_2 by Stable Ni Nanocrystals on Porous Single-Crystalline MgO Monoliths at Reduced Temperature. *Angew. Chem., Int. Ed.* **2021,** *60*, 18792-18799.

13. Abdulrasheed, A.; Jalil, A. A.; Gambo, Y.; Ibrahim, M.; Hambali, H. U.; Hamill, M. Y. S., A review on catalyst development for dry reforming of methane to syngas: Recent advances. *Renew. Sustainable Energy Rev.* **2019,** *108*, 175-193.

14. Liu, W.; Li, L.; Lin, S.; Luo, Y.; Bao, Z.; Mao, Y.; Li, K.; Wu, D.; Peng, H., Confined Ni-In intermetallic alloy nanocatalyst with excellent coking resistance for methane dry reforming. *J. Energy Chem.* **2022,** *65*, 34-47.

15. Kim, K. Y.; Lee, J. H.; Lee, H.; Noh, W. Y.; Kim, E. H.; Ra, E. C.; Kim, S. K.; An, K.; Lee, J. S., Layered Double Hydroxide-Derived Intermetallic $Ni_3GaC_{0.25}$ Catalysts for Dry Reforming of Methane. *ACS Catal.* **2021,** *11*, 11091-11102.

16. Al-Fatesh, A. S.; Ibrahim, A. A.; Abu-Dahrieh, J. K.; Al-Awadi, A. S.; El-Toni, A. M.; Fakeeha, A. H.; Abasaeed, A. E., Gallium-Promoted Ni Catalyst Supported on MCM-41 for Dry Reforming of Methane. *Catalysts* **2018,** *8*, 229.

17. Furukawa, S.; Komatsu, T.; Shimizu, K.-i., Catalyst design concept based on a variety of alloy materials: a personal account and relevant studies. *J. Mater. Chem. A* **2020,** *8*, 15620-15645.

18. Xing, F. L.; Nakaya, Y.; Yasumura, S.; Shimizu, K.; Furukawa, S., Ternary platinum-cobalt-indium nanoalloy on ceria as a highly efficient catalyst for the oxidative dehydrogenation of propane using CO_2. *Nat. Catal.* **2022,** *5*, 55-65.

19. Nakaya, Y.; Miyazaki, M.; Yamazoe, S.; Shimizu, K.-i.; Furukawa, S., Active, Selective, and Durable Catalyst for Alkane Dehydrogenation Based on a Well-Designed Trimetallic Alloy. *ACS Catal.* **2020,** *10*, 5163-5172.

20. Kitchin, J. R.; Nørskov, J. K.; Barteau, M. A.; Chen, J. G., Role of Strain and Ligand Effects in the Modification of the Electronic and Chemical Properties of Bimetallic Surfaces. *Phys. Rev. Lett.* **2004,** *93*, No.156801.

21. Ankudinov, A. L.; Ravel, B.; Rehr, J. J.; Conradson, S. D., Real-space multiple-scattering calculation and interpretation of x-ray-absorption near-edge structure. *Phys. Rev. B* **1998,** *58*, 7565-7576.

22. Segall, M. D.; Lindan, P. J. D.; Probert, M. J.; Pickard, C. J.; Hasnip, P. J.; Clark, S. J.; Payne, M. C., First-principles simulation: ideas, illustrations and the CASTEP code. *Journal of Physics: Condensed Matter* **2002,** *14*, 2717-2744.

23. Hammer, B.; Hansen, L. B.; Nørskov, J. K., Improved adsorption energetics within density-functional theory using revised Perdew-Burke-Ernzerhof functionals. *Phys. Rev. B,* **1999,** *59*, 7413-7421.

24. Tkatchenko, A.; Scheffler, M., Accurate Molecular Van Der Waals Interactions from Ground-State Electron Density and Free-Atom Reference Data. *Phys. Rev. Lett.,* **2009,** *102*, 073005.

25. Hu, K.; Wu, M.; Hinokuma, S.; Ohto, T.; Wakisaka, M.; Fujita, J.-i.; Ito, Y., Boosting electrochemical water splitting via ternary NiMoCo hybrid nanowire arrays. *J. Mater. Chem. A* **2019,** *7*, 2156-2164.

26. Govind, N.; Petersen, M.; Fitzgerald, G.; King-Smith, D.; Andzelm, J., A generalized synchronous transit method for transition state location. *Comput. Mater. Sci.,* **2003,** *28*, 250-258.

27. Halgren, T. A.; Lipscomb, W. N., The synchronous-transit method for determining reaction pathways and locating molecular transition states. *Chem. Phys. Lett.* **1977,** *49*, 225-232.

28. Wang, Y. L.; Hu, P.; Yang, J.; Zhu, Y. A.; Chen, C., C-H bond activation in light alkanes: a theoretical perspective. *Chem. Soc. Rev.,* **2021,** *50*, 4299-4358.

29. Jin, S.; Leinenbach, C.; Wang, J.; Duarte, L. I.; Delsante, S.; Borzone, G.; Scott, A.; Watson, A., Thermodynamic study and re-assessment of the Ge-Ni system. *Calphad-Computer Coupling of Phase Diagrams and Thermochemistry* **2012,** *38*, 23-34.

30. He, L.; Li, M.; Li, W.-C.; Xu, W.; Wang, Y.; Wang, Y.-B.; Shen, W.; Lu, A.-H., Robust and Coke-free Ni Catalyst Stabilized by 1–2 nm-Thick Multielement Oxide for Methane Dry Reforming. *ACS Catal.* **2021,** *11*, 12409-12416.

31. Horlyck, J.; Lawrey, C.; Lovell, E. C.; Amal, R.; Scott, J., Elucidating the impact of Ni and Co loading on the selectivity of bimetallic NiCo catalysts for dry reforming of methane. *Chem. Eng. J.* **2018,** *352*, 572-580.

32. Németh, M.; Srankó, D.; Károlyi, J.; Somodi, F.; Schay, Z.; Sáfrán, G.; Sajó, I.; Horváth, A., Na-promoted Ni/ZrO_2 dry reforming catalyst with high efficiency: details of Na_2O–ZrO_2–Ni interaction controlling activity and coke formation. *Catal. Sci. Technol.* **2017,** *7* , 5386-5401.

33. Wang, Y.; Zhang, R.; Yan, B., Ni/$Ce_{0.9}Eu_{0.1}O_{1.95}$ with enhanced coke resistance for dry reforming of methane. *J. Catal.* **2022,** *407*, 77-89.

34. Li, K.; Chang, X.; Pei, C.; Li, X.; Chen, S.; Zhang, X.; Assabumrungrat, S.; Zhao, Z.-J.; Zeng, L.; Gong, J., Ordered mesoporous Ni/La_2O_3 catalysts with interfacial synergism towards CO_2 activation in dry reforming of methane. *Applied Catalysis B: Environmental* **2019,** *259*.

35. Jin, F. K.; Fu, Y.; Kong, W. B.; Wang, J. Y.; Cai, F. F.; Zhang, J.; Xu, J. Q., Dry reforming of methane over trimetallic NiFeCu alloy catalysts. *Chem. Phys. Lett.* **2020,** *750*.

36. Daoura, O.; Fornasieri, G.; Boutros, M.; El Hassan, N.; Beaunier, P.; Thomas, C.; Selmane, M.; Miche, A.; Sassoye, C.; Ersen, O.; Baaziz, W.; Massiani, P.; Bleuzen, A.; Launay, F., One-pot prepared mesoporous silica SBA-15-like monoliths with embedded Ni particles as selective and stable catalysts for methane dry reforming. *Appl. Catal. B: Environ.* **2021,** *280*.

37. Franz, R.; Pinto, D.; Uslamin, E. A.; Urakawa, A.; Pidko, E. A., Impact of Promoter Addition on the Regeneration of Ni/Al_2O_3 Dry Reforming Catalysts. *Chemcatchem* **2021,** *13*, 5034-5046.

38. Wang, N.; Shen, K.; Huang, L. H.; Yu, X. P.; Qian, W. Z.; Chu, W., Facile Route for Synthesizing Ordered Mesoporous Ni-Ce-Al Oxide Materials and Their Catalytic Performance for Methane Dry Reforming to Hydrogen and Syngas. *ACS Catal.* **2013,** *3*, 1638-1651.

39. Zhang, S.; Muratsugu, S.; Ishiguro, N.; Tada, M., Ceria-Doped Ni/SBA-16 Catalysts for Dry Reforming of Methane. *ACS Catal.* **2013,** *3*, 1855-1864.

40. Yan, X.; Hu, T.; Liu, P.; Li, S.; Zhao, B.; Zhang, Q.; Jiao, W.; Chen, S.; Wang, P.; Lu, J.; Fan, L.; Deng, X.; Pan, Y.-X., Highly efficient and stable Ni/CeO_2-SiO_2 catalyst for dry

reforming of methane: Effect of interfacial structure of Ni/CeO_2 on SiO_2. *Appl. Catal. B: Environ.* **2019,** *246*, 221-231.

41. Li, X. Y.; Li, D.; Tian, H.; Zeng, L.; Zhao, Z. J.; Gong, J. L., Dry reforming of methane over Ni/La_2O_3 nanorod catalysts with stabilized Ni nanoparticles. *Appl. Catal. B: Environ.* **2017,** *202*, 683-694.

42. Ramezani, Y.; Meshkani, F.; Rezaei, M., Promotional effect of Mg in trimetallic nickel-manganese-magnesium nanocrystalline catalysts in CO_2 reforming of methane. *Int. J. Hydrogen Energ.* **2018,** *43*, 22347-22356.

43. Yang, E.; Nam, E.; Lee, J.; Lee, H.; Park, E. D.; Lim, H.; An, K., Al_2O_3-Coated Ni/CeO_2 nanoparticles as coke-resistant catalyst for dry reforming of methane. *Catal. Sci. Technol.* **2020,** *10*, 8283-8294.

44. Kambolis, A.; Matralis, H.; Trovarelli, A.; Papadopoulou, C., Ni/CeO_2-ZrO_2 catalysts for the dry reforming of methane. *Applied Catalysis A: General* **2010,** *377*, 16-26.

45. Chotirach, M.; Tungasmita, S.; Nuntasri Tungasmita, D.; Tantayanon, S., Titanium nitride promoted Ni-based SBA-15 catalyst for dry reforming of methane. *Int. J. Hydrogen Energ.* **2018,** *43*, 21322-21332.

46. Guharoy, U.; Le Saché, E.; Cai, Q.; Reina, T. R.; Gu, S., Understanding the role of Ni-Sn interaction to design highly effective CO_2 conversion catalysts for dry reforming of methane. *J. CO2 Util.,* **2018,** *27*, 1-10.

47. Liu, A.; Praserthdam, S.; Phatanasri, S., Investigation on the increased stability of the Ni–Co bi-metallic catalysts for the carbon dioxide reforming of methane. *Catal. Today* **2020,** *358*, 37-44.

48. Zhang, M.; Zhang, J.; Zhou, Z.; Chen, S.; Zhang, T.; Song, F.; Zhang, Q.; Tsubaki, N.; Tan, Y.; Han, Y., Effects of the surface adsorbed oxygen species tuned by rare-earth metal doping on dry reforming of methane over Ni/ZrO_2 catalyst. *Appl. Catal. B: Environ.* **2020,** *264*.

49. Ay, H.; Üner, D., Dry reforming of methane over CeO_2 supported Ni, Co and Ni–Co catalysts. *Appl. Catal. B: Environ.,* **2015,** *179*, 128-138.

50. Rego de Vasconcelos, B.; Pham Minh, D.; Sharrock, P.; Nzihou, A., Regeneration study of Ni/hydroxyapatite spent catalyst from dry reforming. *Catal. Today* **2018,** *310*, 107-115.

51. Dong, J.; Fu, Q.; Li, H.; Xiao, J.; Yang, B.; Zhang, B.; Bai, Y.; Song, T.; Zhang, R.; Gao, L.; Cai, J.; Zhang, H.; Liu, Z.; Bao, X., Reaction-Induced Strong Metal-Support Interactions between Metals and Inert Boron Nitride Nanosheets. *J. Am. Chem. Soc.* **2020,** *142*, 17167-17174.

52. Feng, X.; Liu, J.; Zhang, P.; Zhang, Q.; Xu, L.; Zhao, L.; Song, X.; Gao, L., Highly coke resistant Mg–Ni/Al_2O_3 catalyst prepared via a novel magnesiothermic reduction for methane reforming catalysis with CO_2: the unique role of Al–Ni intermetallics. *Nanoscale,* **2019,** *11*, 1262-1272.

53. Aseel G.S. Hussien a, b., 1, Constantinos M. Damaskinos c,1, Aasif A. Dabbawala a,b, Dalaver H. Anjum b,d, Michalis A. Vasiliades c, Maryam T.A. Khaleel b,e, Nimer Wehbe f, Angelos M. Efstathiou c,*, Kyriaki Polychronopoulou, Elucidating the role of La^{3+}/Sm^{3+} in the carbon paths of dry reforming of methane over Ni/Ce-La(Sm)-Cu-O using transient kinetics and isotopic techniques. *Appl. Catal. B: Environ.* **2022**.

54. Dan Guo, M. L., Yao Lu, Yifan Zhao, Mianjing Li, Yujun Zhao, Shengping Wang,* and Xinbin Ma, Enhanced Thermocatalytic Stability by Coupling Nickel Step Sites with Nitrogen Heteroatoms for Dry Reforming of Methane. *ACS Catal.* **2022**.

55. Zhang, J.; Li, F., Coke-resistant Ni@SiO_2 catalyst for dry reforming of methane. *Appl. Catal. B: Environ.,* **2015,** *176-177*, 513-521.

56. Wang, H.; Srinath, N. V.; Poelman, H.; Detavernier, C.; Li, P.; Marin, G. B.; Galvita, V. V., Hierarchical Fe-modified $MgAl_{(2)}O_{(4)}$ as a Ni-catalyst support for methane dry reforming. *Catal. Sci. Technol.* **2020,** *10*, 6987-7001.

57. Alenazey, F. S., Utilizing carbon dioxide as a regenerative agent in methane dry reforming to improve hydrogen production and catalyst activity and longevity. *Int. J. Hydrogen Energ.* **2014,** *39*, 18632-18641.

58. Zhang, X. P.; Wang, F.; Song, Z. W.; Zhang, S. J., Comparison of carbon deposition features between Ni/ZrO_2 and Ni/SBA-15 for the dry reforming of methane. *Reaction Kinetics Mechanisms and Catalysis* **2020,** *129*, 457-470.

59. Marinho, A. L. A.; Toniolo, F. S.; Noronha, F. B.; Epron, F.; Duprez, D.; Bion, N., Highly active and stable Ni dispersed on mesoporous CeO_2-Al_2O_3 catalysts for production of syngas by dry reforming of methane. *Appl. Catal. B: Environ.,* **2021,** *281*.

60. Wu, P.; Tao, Y.; Ling, H.; Chen, Z.; Ding, J.; Zeng, X.; Liao, X.; Stampfl, C.; Huang, J., Cooperation of Ni and CaO at Interface for CO_2 Reforming of CH_4: A Combined Theoretical and Experimental Study. *ACS Catal.* **2019,** *9*, 10060-10069.

61. Zhang, S.; Shi, C.; Chen, B.; Zhang, Y.; Qiu, J., An active and coke-resistant dry reforming catalyst comprising nickel–tungsten alloy nanoparticles. *Catal. Commun.* **2015,** *69*, 123-128.

62. Farooqi, A. S.; Al-Swai, B. M.; Ruslan, F. H.; Mohd Zabidi, N. A.; Saidur, R.; Syed Muhammad, S. A. F. a.; Abdullah, B., Catalytic conversion of greenhouse gases (CO_2 and CH_4) to syngas over Ni-based catalyst: Effects of Ce-La promoters. *Arab. J. Chem.* **2020,** *13*, 5740-5749.

63. Dudder, H.; Kahler, K.; Krause, B.; Mette, K.; Kuhl, S.; Behrens, M.; Scherer, V.; Muhler, M., The role of carbonaceous deposits in the activity and stability of Ni-based catalysts applied in the dry reforming of methane. *Catal. Sci. Technol.* **2014,** *4*, 3317-3328.

64. Pegios, N.; Schroer, G.; Rahimi, K.; Palkovits, R.; Simeonov, K., Design of modular Ni-foam based catalysts for dry reforming of methane. *Catal. Sci. Technol.* **2016,** *6* , 6372-6380.

65. Naidu, B. N.; Kumar, K. D. P. L.; Saini, H.; Kumar, M.; Kumar, T. N.; Prasad, V. V. D. N., Coke deposition over Ni-based catalysts for dry reforming of methane: effects of MgO-Al_2O_3

support and ceria, lanthana promoters. *Journal of Environmental Chemical Engineering* **2022,** *10*, 106980.

66. Das, S.; Jangam, A.; Xi, S.; Borgna, A.; Hidajat, K.; Kawi, S., Highly Dispersed Ni/Silica by Carbonization–Calcination of a Chelated Precursor for Coke-Free Dry Reforming of Methane. *ACS Applied Energy Materials* **2020,** *3*, 7719-7735.

67. Sutthiumporn, K.; Maneerung, T.; Kathiraser, Y.; Kawi, S., CO_2 dry-reforming of methane over $La_{0.8}Sr_{0.2}Ni_{0.8}M_{0.2}O_3$ perovskite (M = Bi, Co, Cr, Cu, Fe): Roles of lattice oxygen on C-H activation and carbon suppression. *Int. J. Hydrogen Energ.,* **2012,** *37*, 11195-11207.

68. Cao, K.; Gong, M.; Yang, J.; Cai, J.; Chu, S.; Chen, Z.; Shan, B.; Chen, R., Nickel catalyst with atomically-thin meshed cobalt coating for improved durability in dry reforming of methane. *J. Catal.* **2019,** *373*, 351-360.

69. Dai, Y.-M.; Lu, C.-Y.; Chang, C.-J., Catalytic activity of mesoporous Ni/CNT, Ni/SBA-15 and (Cu, Ca, Mg, Mn, Co)–Ni/SBA-15 catalysts for CO_2 reforming of CH_4. *RSC Adv.* **2016,** *6* , 73887-73896.

70. Tian, J.; Li, H.; Zeng, X.; Wang, Z.; Huang, J.; Zhao, C., Facile immobilization of Ni nanoparticles into mesoporous MCM-41 channels for efficient methane dry reforming. *Chinese J. Catal.* **2019,** *40*, 1395-1404.

71. Al-Fatesh, A., Suppression of carbon formation in CH_4 –CO_2 reforming by addition of Sr into bimetallic Ni–Co/γ-Al_2O_3 catalyst. *J. King Saud Univ. Eng. Sci.* **2015,** *27*, 101-107.

72. Wang, N.; Chu, W.; Zhang, T.; Zhao, X. S., Synthesis, characterization and catalytic performances of Ce-SBA-15 supported nickel catalysts for methane dry reforming to hydrogen and syngas. *Int. J. Hydrog. Energy* **2012,** *37*, 19-30.

73. Al-Fatesh, A. S.; Arafat, Y.; Kasim, S. O.; Ibrahim, A. A.; Abasaeed, A. E.; Fakeeha, A. H., In situ auto-gasification of coke deposits over a novel Ni-Ce/W-Zr catalyst by sequential

generation of oxygen vacancies for remarkably stable syngas production via CO_2-reforming of methane. *Appl. Catal. B: Environ.,* **2021,** *280*, 119445.

74. Cao, Y.; Li, H.; Zhang, J.; Shi, L.; Zhang, D., Promotional effects of rare earth elements (Sc, Y, Ce, and Pr) on NiMgAl catalysts for dry reforming of methane. *RSC Adv.* **2016,** *6*, 112215-112225.

75. Turap, Y.; Wang, I.; Fu, T.; Wu, Y.; Wang, Y.; Wang, W., Co–Ni alloy supported on CeO_2 as a bimetallic catalyst for dry reforming of methane. *Int. J. Hydrog. Enery.,* **2020,** *45*, 6538-6548.

76. Zhu, J.; Peng, X.; Yao, L.; Deng, X.; Dong, H.; Tong, D.; Hu, C., Synthesis gas production from CO_2 reforming of methane over Ni–Ce/SiO_2 catalyst: The effect of calcination ambience. *Int. J. Hydrog. Energy,* **2013,** *38* (1), 117-126.

77. Li, Z. W.; Mo, L. Y.; Kathiraser, Y.; Kawi, S., Yolk-Satellite-Shell Structured Ni-Yolk@Ni@SiO_2 Nanocomposite: Superb Catalyst toward Methane CO_2 Reforming Reaction. *ACS Catal.* **2014,** *4* (5), 1526-1536.

78. Ewbank, J. L.; Kovarik, L.; Diallo, F. Z.; Sievers, C., Effect of metal–support interactions in Ni/Al_2O_3 catalysts with low metal loading for methane dry reforming. *Appl. Catal. A: Gen.* **2015,** *494*, 57-67.

79. Ghanbarabadi, H.; Khoshandam, B., Dry reforming of methane over gamma-Al_2O_3 supported NiCo and NiCoCu nano-catalysts. *Int. J. Hydrogen Energ.* **2021**

80. Zhang, X.; Deng, J.; Pupucevski, M.; Impeng, S.; Yang, B.; Chen, G.; Kuboon, S.; Zhong, Q.; Faungnawakij, K.; Zheng, L.; Wu, G.; Zhang, D., High-Performance Binary Mo–Ni Catalysts for Efficient Carbon Removal during Carbon Dioxide Reforming of Methane. *ACS Catal.* **2021**, 12087-12095.

81. Cooperatively enhanced coking resistance via boron nitride coating over Ni-based catalysts for dry reforming of methane. *Appl. Catal. B: Environ.,* **2022**.

82. Bian, Z.; Kawi, S., Highly carbon-resistant Ni–Co/SiO 2 catalysts derived from phyllosilicates for dry reforming of methane. *Journal of CO_2 Utilization* **2017,** *18*, 345-352.

83. Lin, X.; Li, R.; Lu, M.; Chen, C.; Li, D.; Zhan, Y.; Jiang, L., Carbon dioxide reforming of methane over Ni catalysts prepared from Ni–Mg–Al layered double hydroxides: Influence of Ni loadings. *Fuel* **2015,** *162*, 271-280.

84. Zhang, J.; Wang, H.; Dalai, A., Development of stable bimetallic catalysts for carbon dioxide reforming of methane. *J. Catal.* **2007,** *249*, 300-310.

85. Fan, M.-S.; Abdullah, A. Z.; Bhatia, S., Utilization of greenhouse gases through carbon dioxide reforming of methane over Ni–Co/MgO–ZrO_2: Preparation, characterization and activity studies. *Appl. Catal. B: Environ.,* **2010,** *100*, 365-377.

86. Feng, J.; Ding, Y.; Guo, Y.; Li, X.; Li, W., Calcination temperature effect on the adsorption and hydrogenated dissociation of CO_2 over the NiO/MgO catalyst. *Fuel* **2013,** *109*, 110-115.

87. Song, Y.; Ozdemir, E.; Ramesh, S.; Adishev, A.; Subramanian, S.; Harale, A.; Albuali, M.; Fadhel, B. A.; Jamal, A.; Moon, D.; Choi, S. H.; Yavuz, C. T., Dry reforming of methane by stable Ni-Mo nanocatalysts on single-crystalline MgO. *Science* **2020,** *367*, 777-+.

88. Huang, T.; Huang, W.; Huang, J.; Ji, P., Methane reforming reaction with carbon dioxide over SBA-15 supported Ni–Mo bimetallic catalysts. *Fuel Process. Technol.* **2011,** *92*, 1868-1875.

89. Bhavani, A. G.; Kim, W. Y.; Kim, J. Y.; Lee, J. S., Improved activity and coke resistance by promoters of nanosized trimetallic catalysts for autothermal carbon dioxide reforming of methane. *Appl. Catal. A: Gen.* **2013,** *450*, 63-72.

90. Tanios, C.; Gennequin, C.; Labaki, M.; Tidahy, H. L.; Aboukais, A.; Abi-Aad, E., Evaluation of a Catalyst Durability in Absence and Presence of Toluene Impurity: Case of the Material $Co_2Ni_2Mg_2Al_2$ Mixed Oxide Prepared by Hydrotalcite Route in Methane Dry Reforming to Produce Energy. *Materials (Basel)* **2019,** *12*.

91. Kim, W. Y.; Jang, J. S.; Ra, E. C.; Kim, K. Y.; Kim, E. H.; Lee, J. S., Reduced perovskite $LaNiO_3$ catalysts modified with Co and Mn for low coke formation in dry reforming of methane. *Appl. Catal. A: Gen.* **2019,** *575*, 198-203.

92. Xing, F.; Ma, J.; Shimizu, K.-i.; Furukawa, S., High-entropy intermetallics on ceria as efficient catalysts for the oxidative dehydrogenation of propane using CO_2. *Nat. Commun.* **2022,** *13*, 5065.

Chapter 3

Enhanced CO_2 Utilization in Dry reforming of Benzene over Intermetallic Ni_3Ga Catalyst

3. Enhanced CO_2 Utilization in Dry reforming of Benzene over Intermetallic Ni_3Ga Catalyst

3.1 Introduction

The environmental problems caused by carbon dioxide (CO_2) emissions are a major concern in the scientific and industrial fields. The chemical utilization of CO_2 as an abundant and nontoxic C1 block can contribute to the control of excess CO_2 emissions while generating valuable feedstocks to alleviate the problem of fossil fuel depletion.[1-3] A promising method for large-scale CO_2 utilization is dry reforming with hydrocarbons owing to the relatively energy-favorable requirement.[4] Dry reforming of methane (DRM) has been regarded as a representative route among dry reforming reactions, however, the stoichiometric ratio of CH_4 and CO_2 makes the consumption of CO_2 very limited.

The dry reforming of benzene (DRB; $C_6H_6 + 6CO_2 \rightarrow 3H_2 + 12CO$) has significant potential for reducing CO_2 to the barest minimum. This process uses up to 6 mol of CO_2 per mol of benzene according to the stoichiometric ratio. Aromatic compounds including benzene can be obtained from the degradation of bioderived lignin. Therefore, DRB has a huge potential for carbon neutralization. A reaction temperature above 700°C is required because of the high endothermicity of DRB.[5-7] However, there are certain drawbacks at high temperatures, such as side reactions (benzene cracking: e.g., $C_6H_6 \rightarrow 6C + 6H$ and reverse water gas reaction: $CO_2 + H_2 \rightarrow CO + H_2O$) and poor stability due to coke formation and metal sintering, which hamper the practical application of DRB. In addition, a high-temperature process is energy-intensive.[8] Therefore, an appropriate catalyst for DRB reactions that functions in a relatively low-temperature region is highly attractive.

Supported Ni catalysts are promising for the reforming reactions of hydrocarbons owing to their strong ability to break C–C or C–H bonds and their relatively low price.[9-11] Nevertheless,

it is well-known that coke deposition on Ni catalysts severely hinders their catalytic performance. Many strategies have been employed to improve their coke resistance, among which alloying is considered one of the most effective routes.[12-14] Ni-based intermetallic compounds have been widely utilized for DRM and the steam reforming of benzene reactions, in which Ni–Ni ensembles were normally diluted by catalytically inactive metals, such as early transition and typical metals, to form the intermetallic phase.[15-16] Moreover, the specific ordered atomic arrangement of Ni intermetallic compounds can alter the electronic and geometric structure of Ni and the adsorption behaviors of the reactants, leading to high catalytic activity and selectivity.[15, 17]

Herein, we report a binary Ni_3Ga intermetallic compound that functions as an effective catalyst for the DRB at 500°C. The Ni_3Ga/CeO_2 catalyst exhibited significantly enhanced CO_2 utilization and long-term stability compared with the corresponding monometallic Ni catalyst (Scheme 3.1). Moreover, alloying with Ga modified the CO_2 activation ability and improved the carbon deposition resistance, resulting in high stability. This study provides insight into Ni-based catalysts for CO_2 utilization.

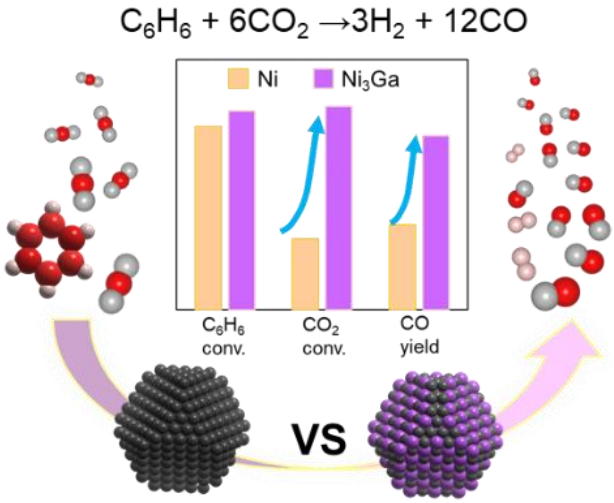

Scheme 3.1 The catalyst design concept for the Ni_3Ga/CeO_2.

3.2 Experimental Methods

3.2.1 Catalyst preparation

Ni_3Ga/CeO_2 and Ni/CeO_2 (Ni = 3 wt%) were prepared using a conventional impregnation method with $Ni(NO_3)_2 \cdot 6H_2O$ (Kanto Chemical, 98.0%) and $Ga(NO_3)_2 \cdot nH_2O$ (n = 7–9, Wako, 99.9%) as metal precursors (Ni:Ga = 3:1). The CeO_2 support (JRC-CEO-2, SBET = 123.1 m^2g^{-1}) was added to a vigorously stirred aqueous solution (50 mL of H_2O per gram of CeO_2) containing Ni and Ga followed by stirring for 3 h at 30°C. The mixture was dried under a reduced pressure at 40°C using a rotary evaporator, then the sample was calcined under flowing air at 500°C for 1 h and reduced under flowing H_2 (50 mL/min) at 500°C for 1 h at a ramping rate of 10°C min^{-1}. Different Ni/Ga ratios and a monometallic Ga catalyst (a Ga content of 1.19 wt% to ensure the same loading as that in Ni_3Ga) supported on CeO_2 and Ni_3Ga/Al_2O_3 catalysts (the Al_2O_3 was prepared through the calcination of boehmite (γ-AlOOH, supplied by Sasol chemicals) at 900°C for 3 h, γ-phase) were prepared using the aforementioned method. In addition, Ni_3Ga/SiO_2 was prepared using a pore-filling co-impregnation method. A mixture of an aqueous solution of metal precursors with a known amount of water was added dropwise to dried SiO_2 (CARiACT G-6, Fuji Silysia, S_{BET} = 673 $m^2 \cdot g^{-1}$). The mixture was sealed and under static overnight at room temperature so that the solutions flowed into the SiO_2 pores. Subsequently, the mixture was transferred to a round-bottom flask and rapidly frozen with liquid nitrogen. The frozen sample was dried in a vacuum at −5°C. The resulting powder was dried overnight in an oven at 90°C, under the same aforementioned calcination and reduction conditions.

3.2.2 Characterization

The crystallite phases of the prepared catalysts were determined by XRD using a Rigaku MiniFlex II/AP diffractometer with Cu Kα radiation. The XAFS spectra of the prepared

catalysts were recorded at the BL01B1 and BL14B2 beamlines of SPring-8, The Japan Synchrotron Radiation Research Institute (JASRI), using Si (111) double crystals as monochromators at room temperature. The catalyst was pelletized and pretreated with H_2 at 700°C for 0.5 h in a quartz tube to prepare the XAFS specimen. Afterward, it was transferred into an Ar glove box (O_2 < 0.01 ppm) without exposure to air after cooling to room temperature with N_2 purge. The pellet and an oxygen absorber (ISO A500-HS: Fe powder) were sealed in a plastic film bag (Barrier Nylon) to prevent air leakage. The obtained XAFS spectra were fitted using the Athena and Artemis software (version 0.9.25) implemented in the Demeter package. FEFF8 was applied for the calculation of the back-scattering amplitude and phase shift functions. A JEOL JEM-ARM200 M microscope equipped with an energy-dispersive X-ray analyzer was used for the HAADF-STEM analysis. The coke amount on the spent catalysts was analyzed by TPO using a BELCAT II (Microtrac BEL) instrument. First, the spent catalysts (0.5 g of catalyst and quartz sand) in a quartz tube were treated at 150°C for 30 min under a flow of He (30 mL·min^{-1}). After cooling to 50°C, 2% O_2/He (50 mL·min^{-1}) was passed through for baseline stabilization. Thereafter, the catalyst was heated from 50°C to 900°C (ramping rate of 5°C·min^{-1}). An online mass spectrometer equipped downstream recorded the CO_2 amount (m/z = 44) in the outlet gas.

3.2.3 Catalytic test

DRB was conducted in a fixed-bed quartz reactor with an internal diameter of 6 mm under atmospheric pressure. The fresh catalyst (0.1 g) diluted with quartz sand (0.9 g) was firmly fixed in the reactor tube using quartz wool. Prior to the DRB test, the sample was pretreated under flowing H_2 (10 mL·min^{-1}, 500°C) for 0.5 h, followed by residual H_2 gas purged with He gas (20 mL·min^{-1}) for 0.5 h. Subsequently, the reactant gas comprising C_6H_6:CO_2:He = 2.4:14.4:20 with a total gas flow rate of 36.8 mL·min^{-1} was introduced into the reactor at 500°C.

Benzene was supplied using a bubbler at 35°C with He as a carrier gas (10 mL·min^{-1}). The flow rate of benzene was calculated based on the saturated vapor pressure at 35°C. The flow rate of CO_2 was determined to be 6 times higher than that of benzene for stoichiometric conversion. CO_2 was supplied with He carrier gas (10 mL·min^{-1}). The detailed setup of the reactor is shown in Figure 3.1. The compositional analysis of the effluent gas was conducted using an online gas chromatograph (Shimadzu GC-2014s), equipped with a Porapak Q column and thermal conductivity detector. For all the catalysts, the C_6H_6 and CO_2 conversions were defined using the following equations:

$$C_6H_6\ conversion: X_{C_6H_6}\ (\%) = \frac{F^{in}_{C_6H_6} - F^{out}_{C_6H_6}}{F^{in}_{C_6H_6}} \times 100$$

$$CO_2\ conversion: X_{CO_2}\ (\%) = \frac{F^{in}_{CO_2} - F^{out}_{CO_2}}{F^{in}_{CO_2}} \times 100$$

$$CO\ Yield: = \frac{F^{out}_{CO}}{6F^{in}_{C_6H_6} + F^{in}_{CO_2}} \times 100$$

$$Carbon\ balance: C_b = \frac{F^{out}_{CO} + 6F^{out}_{C_6H_6} + F^{out}_{CO_2}}{6F^{in}_{C_6H_6} + F^{in}_{CO_2}} \times 100$$

where, $F^{in}_{C_6H_6}$ $F^{in}_{CO_2}$ and $F^{out}_{C_6H_6}$ $F^{out}_{CO_2}$, F^{out}_{CO}, indicate the inlet flow rate of C_6H_6, CO_2, and outlet flow rates of C_6H_6, CO_2 and CO_2 respectively.

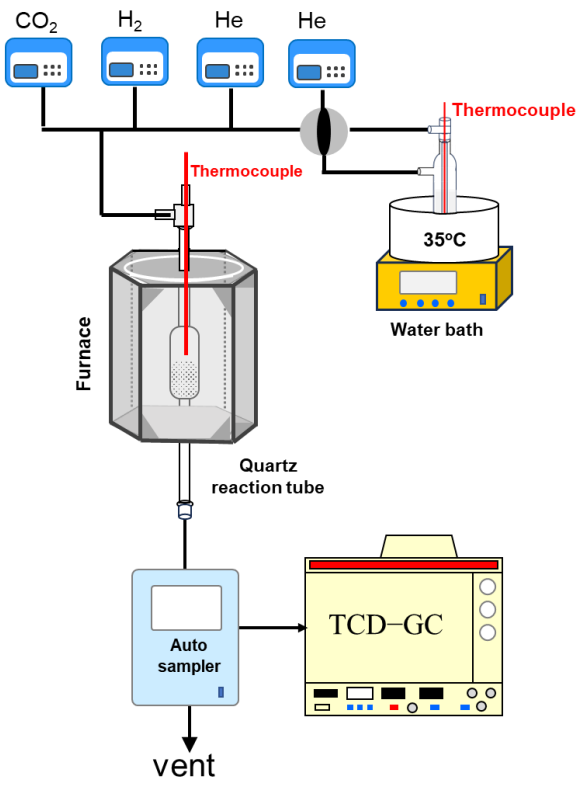

Figure 3.1. The detailed setup of the reactor for dry reforming of benzene. The thermocouple for the water bath was the actual temperature of benzene. The flow rate of benzene was calculated based on the saturated vapor pressure at 35°C using the bubble system.

3.3 Results and Discussion

3.3.1 Structure Characterization of the catalysts

The Ni_3Ga/CeO_2 catalyst was prepared using a conventional co-impregnation method. CeO_2 was used as a catalyst support suitable for CO_2 adsorption and the subsequent activation.[18-19] The crystal structure of the Ni_3Ga catalyst was examined by X-ray diffraction (XRD). When SiO_2 was used as a support for Ni_3Ga, two intense peaks were observed at 43.7° and 50.9°, corresponding to the 111 and 200 diffractions of intermetallic Ni_3Ga, respectively (Figure 3.2a). However, no corresponding diffraction peaks were observed for Ni_3Ga/CeO_2. A similar phenomenon is frequently observed for CeO_2-supported metallic catalysts, mainly due to the strong X-ray scattering by Ce that has a larger atomic weight and scattering coefficient than Si, significantly weakening the X-ray reflection from the Ni_3Ga nanoparticles.[18-19] Therefore, X-ray adsorption fine structure (XAFS) analysis was performed to further investigate the structure of Ni_3Ga/CeO_2. The Ni K- and Ga K-edge X-ray absorption near-edge structure (XANES) spectra of Ni_3Ga/CeO_2 were similar to those of the corresponding reference foils, indicating that these metals were reduced to zero-valent states (Figures. 3.2b and 3.2c). Curve-fitting analysis was performed on the extended XAFS (EXAFS; Table 3.1, Figs. 3.3–3.5 and Table 3.2) oscillations and revealed that the Ni–Ga and Ni–Ni scatterings of Ni_3Ga can be distinguished by EXAFS. The ratio of the coordination numbers was approximately 2.0 ($CN_{Ni–Ni}$ = 7.9, $CN_{Ni–Ga}$ = 4.0), which correlated with the theoretical value of intermetallic Ni_3Ga (2.0, $CN_{Ni–Ni}$ = 8.0, $CN_{Ni–Ga}$ = 4.0). Therefore, these results supported the formation of intermetallic Ni_3Ga on the CeO_2 support. We also performed high-angle annular dark-field scanning transmission microscopy (HAADF-STEM) analysis on Ni_3Ga/CeO_2. As shown in Figure 3.6, metallic nanoparticles were not visible in the HAADF-STEM image. This is most likely due to insufficient Z-contrast between Ce and the other metals. However, the elemental maps of Ni and Ga clearly indicated the presence of small (2~3 nm) bimetallic nanoparticles on the CeO_2

support. The atomic ratio of Ni:Ga in these nanoparticles were approximately 3:1 (Figure 3.7), which was consistent finely with the formation of nanoparticulate intermetallic Ni_3Ga.

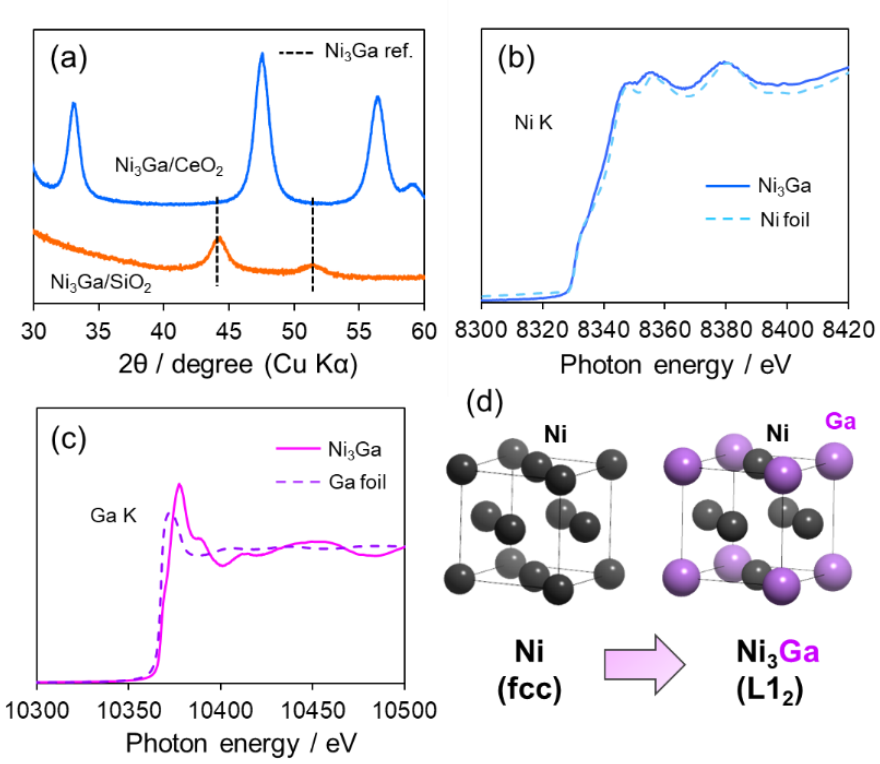

Figure 3.2. (a) XRD patterns of Ni_3Ga supported by SiO_2 and CeO_2. (b), (c) Ni K- and Ga K-edge XANES spectra of the in situ reduced catalysts (solid lines) and reference foils (dashed lines). (d) Model of the Ni_3Ga intermetallic structure with the crystal structure unit.

Table 3.1. Results of EXAFS curve fitting analysis of the Ni_3Ga/CeO_2 catalyst.

Shell	CN	r (Å)	ΔE_o (eV)	σ^2 (Å^2)	R-factor
Ni–Ni	12 (fix)	2.48±0.00	6.5±0.2	0.006	0.000
Ni–Ni	7.9±0.4	2.48±0.00	7.5±0.8	0.006	0.001
Ni–Ga	4.0±0.4	2.57±0.04		0.015	
Ga–Ni	5.4±1.0	2.51±0.01	6.4±1.9	0.009	0.018
Ga–O	1.4±0.9	1.86±0.02		0.004	

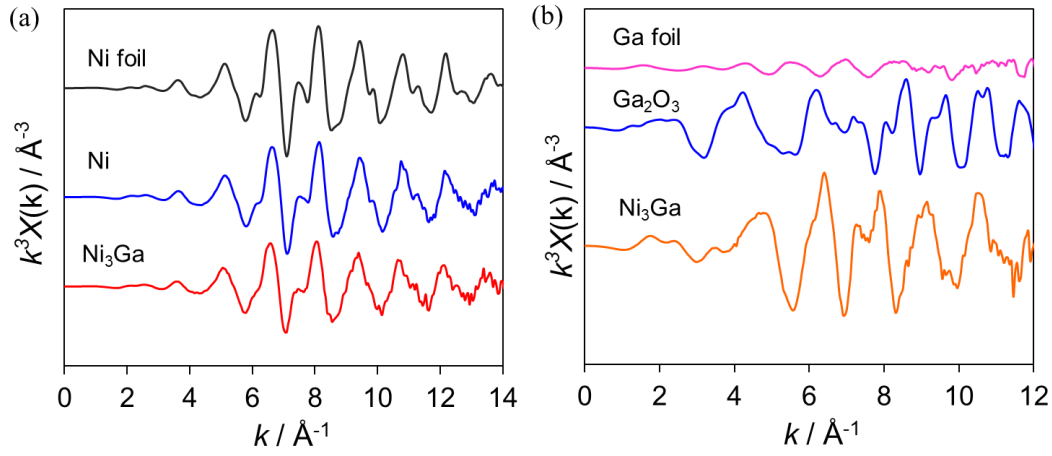

Figure 3.3. (a) Ni and (b) Ga K-edge extended X-ray absorption fine structure (EXAFS) spectra of the Ni_3Ga/CeO_2 and Ni / CeO_2 catalysts and reference compound.

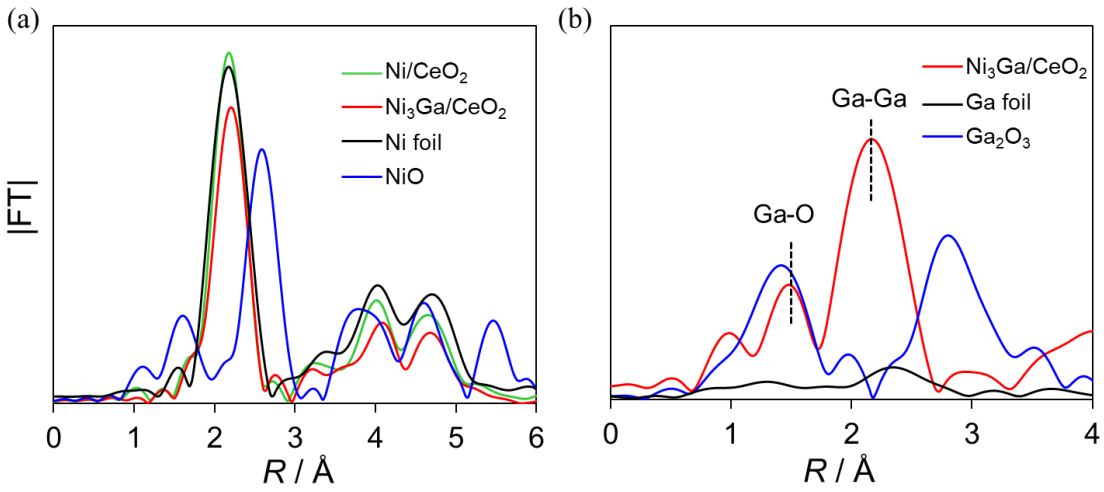

Figure 3.4. Fourier-transforms of EXAFS in (a) Ni, (b) Ga K-edge of the Ni_3Ga/CeO_2 and Ni/CeO_2 catalysts and reference compounds.

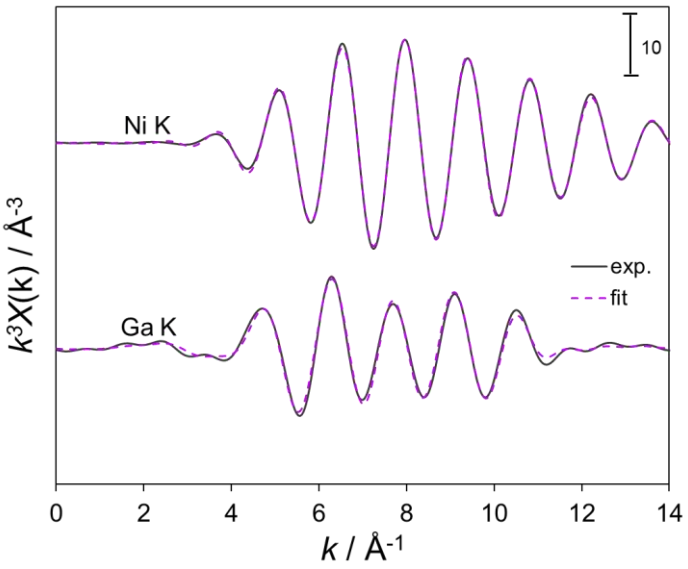

Figure 3.5. Curve-fitting results of Ni K and Ga K-edge k^3-weighted EXAFS of Ni_3Ga/CeO_2. Solid and dashed lines indicate the results of simulation and experiment, respectively.

Table 3.2. Results of EXAFS curve-fitting analysis for Ni_3Ga /CeO_2 catalyst.

Sample	Edge	Shell	S_o^2	CN	r (Å)	ΔE_o (eV)	σ^2 (Å^2)	R-factor
Ni foil	Ni K	Ni–Ni	0.81	12 (fix)	2.48 ± 0.00	6.5±0.2	0.006	0.000
		Ga-O		3 (fix)	1.91 ± 0.02		0.002	
Ga_2O_3	Ga K	Ga-O	1.13	1 (fix)	2.10 ± 0.03	9.3±2.6	0.002	0.014
		Ga-Ga		2 (fix)	3.06 ± 0.01		0.001	
Ni_3Ga/ CeO_2	Ni K	Ni-Ni	0.81	7.9 ± 0.4	2.48 ± 0.00	7.5±0.8	0.006	0.001
		Ni-Ga		4.0 ± 0.4	2.57 ± 0.04		0.015	
	Ga K	Ga-Ni	1.13	5.4 ± 1.0	2.51 ± 0.01	6.4±1.9	0.009	0.018
		Ga-O		1.4 ±0.9	1.86 ± 0.02		0.004	

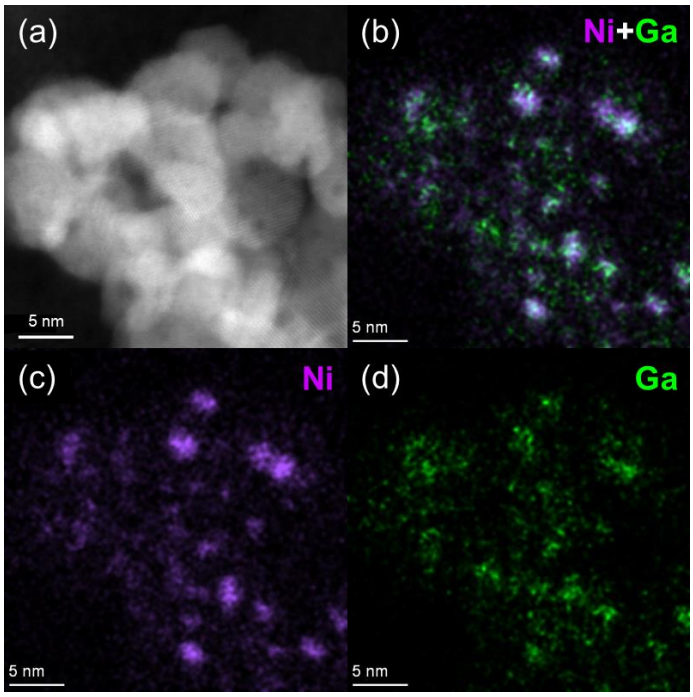

Figure 3.6. (a) HAADF-STEM image and the corresponding elemental maps of Ni_3Ga/CeO_2: (b) Ni+Ga, (c) Ni, and (d) Ga.

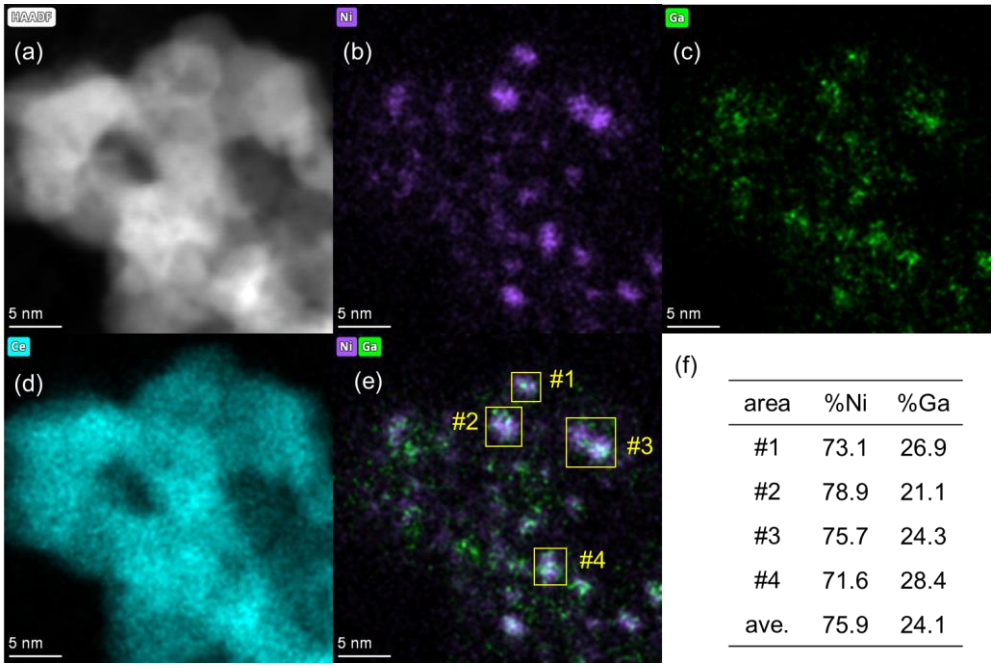

area	%Ni	%Ga
#1	73.1	26.9
#2	78.9	21.1
#3	75.7	24.3
#4	71.6	28.4
ave.	75.9	24.1

Figure 3.7. (a) HAADF-STEM image and the corresponding elemental maps of Ni_3Ga/CeO_2: (b) Ni, (c) Ga, (d) Ce, (e) Ni+Ga. (f) Atomic ratios of Ni and Ga in the regions designated by yellow squares in (e), which agreed roughly with 3:1 (75:25).

3.3.2 Catalytic performance in DRB

Next, the catalytic performance of Ni_3Ga was tested in a DRB reaction at 500°C and compared with that of the monometallic Ni catalyst. Although the Ni_3Ga and Ni catalysts exhibited similar benzene conversions, a large difference was observed in the CO_2 conversion and CO yield, which were markedly enhanced by alloying Ni with Ga (Figure 3.8 and Figure 3.9 for the time course). Moreover, the carbon balance was close to unity (Figure 3.9d), indicating that the selectivity of Ni_3Ga toward undetected products was negligible. Notably, benzene and CO_2 were stoichiometrically converted over intermetallic Ni_3Ga. This reflected the considerably higher selectivity of the intermetallic Ni_3Ga catalyst for dry reforming and CO_2 utilization in contrast with the monometallic Ni catalyst. The stoichiometric conversion of benzene and CO_2 is necessary for effective CO_2 utilization and for preventing coke accumulation due to excess benzene cracking. For Ni/CeO_2, the CO yield was slightly higher than the CO_2 conversion, probably because a part of the accumulated carbon derived from the benzene cracking was oxidized to CO by the lattice oxygen of CeO_2. We also performed control experiments using physical mixtures of Ni/CeO_2 and Ga/CeO_2 and the latter alone (Figure 3.10), which demonstrated a considerably low performance and negligible activity, respectively. This indicates that alloying Ni with Ga is essential for an enhanced catalytic performance. Subsequently, we examined a series of catalysts $Ni_{1-x}Ga_x/CeO_2$ with different Ni:Ga molar ratio (x=0.25, 0.5, 0.6) in DRB reactions in a similar manner as previously conducted (Figure 3.11a and Figure 3.12). The Ga content of the Ni:Ga alloy drastically affected the catalytic performance. The catalyst with a Ni:Ga ratio of 1:1 exhibited a benzene conversion of 10%, whereas its CO_2 conversion was extremely low (<2%). This might have been because excess Ga largely weakened the CO_2 activation ability of Ni. The CO yield was also slightly higher than the CO_2 conversion, probably because the lattice oxygen of CeO_2 may contribute to a part of CO production as we explained earlier.[18] A further increase in the Ga content (Ni:Ga = 2:3)

resulted in a lower benzene conversion, indicating that an appropriate size of Ni–Ni ensembles was necessary for the adsorption/activation of benzene. Next, the support effect was studied using Al_2O_3 and SiO_2 instead of CeO_2 (Figure 3.11b and Figure 3.13 for the time course). The catalytic performance of Ni_3Ga/CeO_2 was significantly higher than that using other supports. Notably, the CO_2 conversion of Ni_3Ga/Al_2O_3 was only half of that of Ni_3Ga/CeO_2, whereas that of Ni_3Ga/SiO_2 was even close to zero. This is probably because the basicity and the oxygen-releasing ability of CeO_2 facilitated CO_2 adsorption (activity) and coke combustion (stability) respectively.[18-19] We also performed a long-term stability test using the Ni_3Ga/CeO_2 catalyst, in which no significant deactivation was observed at least for 20 h (Figure 3.14).

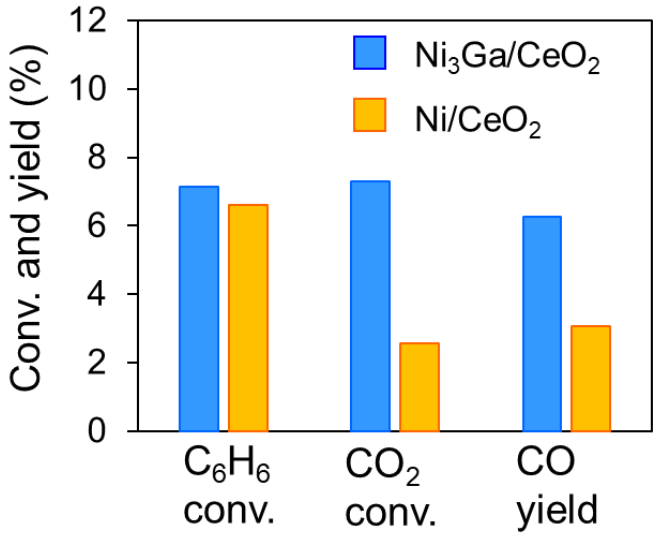

Figure 3.8. Catalytic performance of Ni_3Ga/CeO_2 and Ni/CeO_2 in the DRB. Reaction conditions: catalyst amount, 100 mg; flow rate, C_6H_6:CO_2:He = 2.4:14.4:20 mLmin^{-1}; temperature, 500°C. Values at a time-on-stream of 125 min are shown.

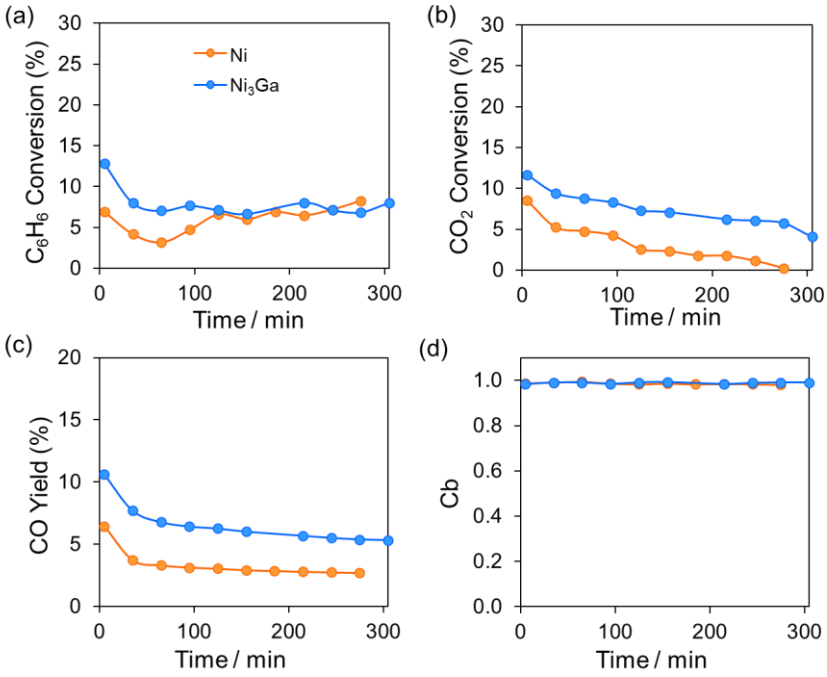

Figure 3.9. (a) C_6H_6 conversion, (b) CO_2 conversion (c) Product CO yield, (d) Carbon balance of Ni_3Ga/CeO_2 and Ni/CeO_2.

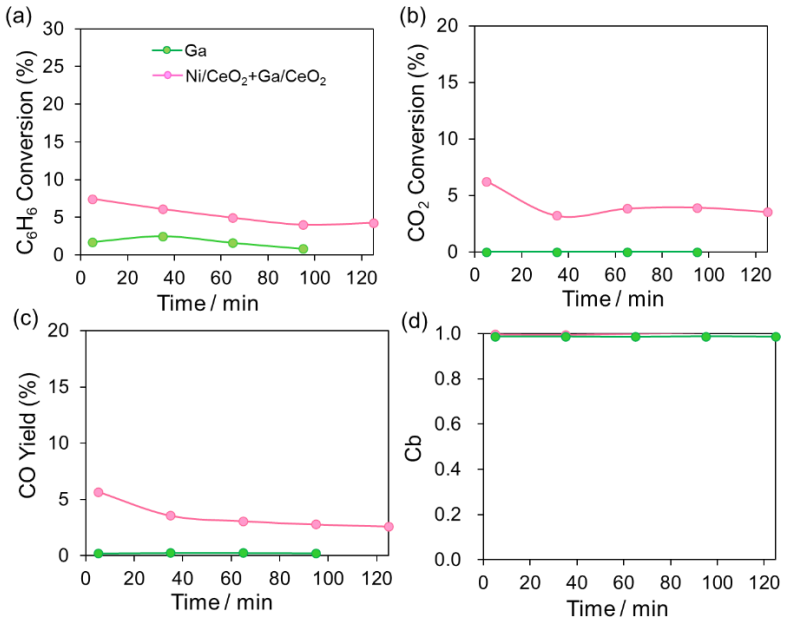

Figure 3.10. Catalytic performance of physical mixtures of Ni/CeO_2 + Ga/CeO_2 and monometallic Ga/CeO_2 in DRB. (a) C_6H_6 conversion, (b) CO_2 conversion (c) CO yield and (d) carbon balance.

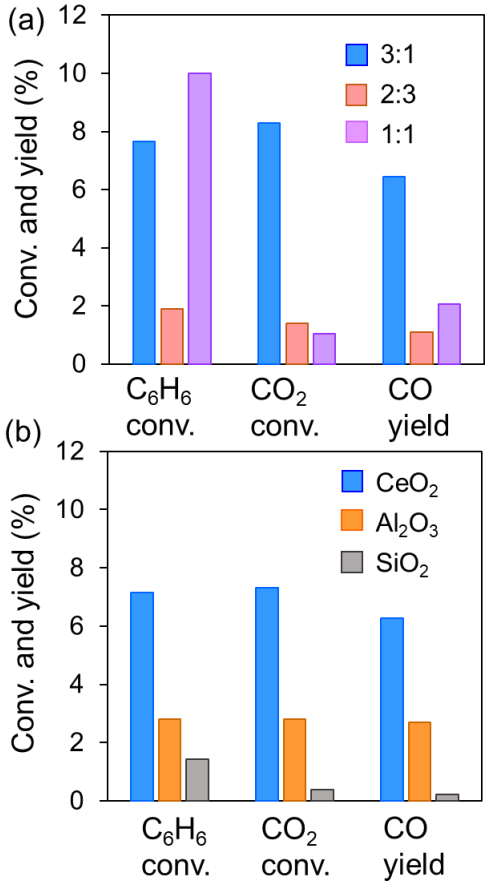

Figure 3.11. Catalytic performance of (a) $Ni_{1-x}Ga_x/CeO_2$ with different Ni:Ga ratios and (b) Ni_3Ga on different supports (CeO_2, Al_2O_3, and SiO_2) in the DRB (values at a time-on-stream of 95 min and 125 min are shown, respectively).

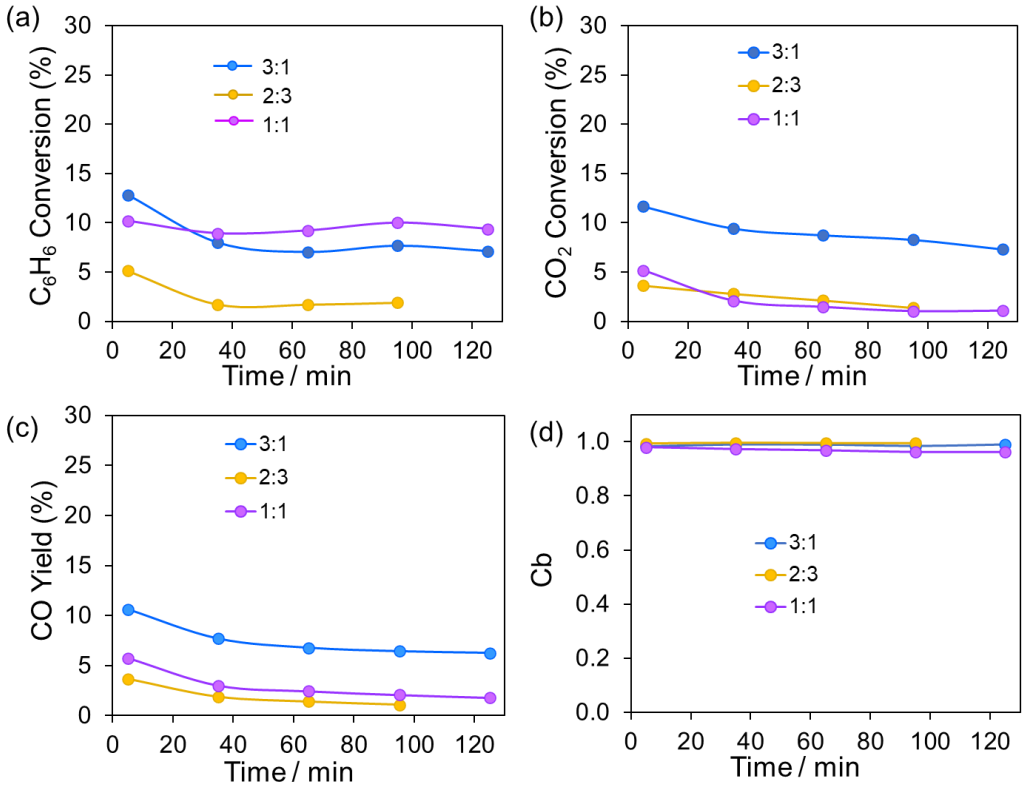

Figure 3.12. Catalytic activity of different Ni/Ga molar ratio in $Ni_{1-x}Ga_x/CeO_2$ (x = 0.25, 0.5, 0.6). (a) C_6H_6 conversion, (b) CO_2 conversion (c) CO yield and (d) carbon balance.

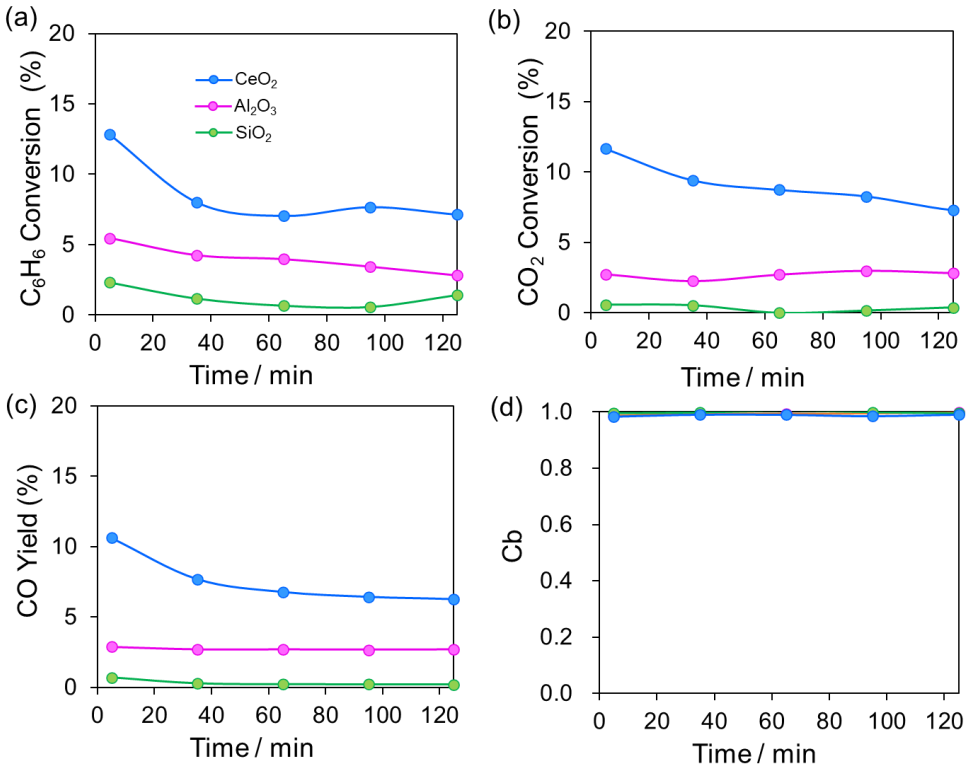

Figure 3.13. (a) C_6H_6 conversion, (b) CO_2 conversion (c) CO yield and (d) carbon balance in DRB on the Ni_3Ga catalysts using various support.

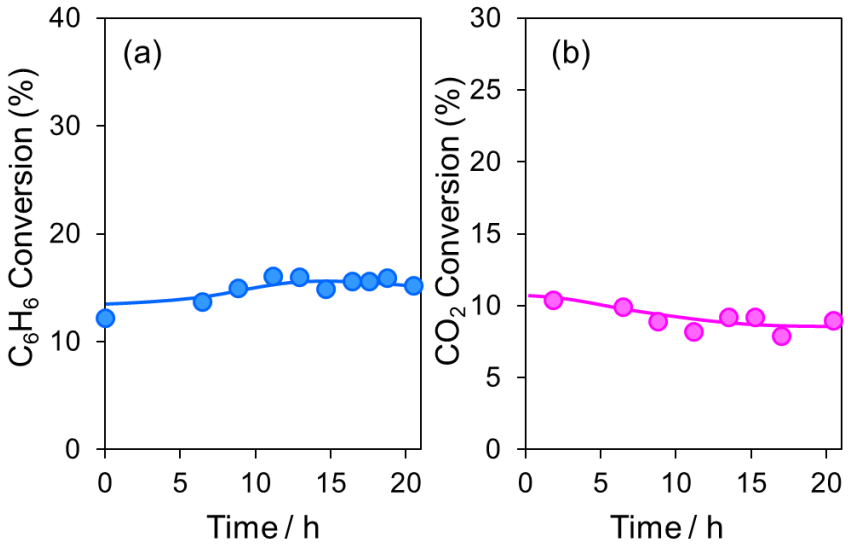

Figure 3.14. Stability test using Ni_3Ga/CeO_2 in benzene dry reforming: (a) benzene and (b) CO_2 conversion. Reaction condition: catalyst amount, 200 mg; flow rate, C_6H_6:CO_2:He = 2.4:14.4:20 mLmin^{-1}; temperature, 500°C.

To clarify the role of Ga, the coke behavior of spent catalysts was analyzed by temperature-programmed oxidation (O_2-TPO; Fig. 3.15). The spent Ni/CeO_2 catalyst exhibited an intense evolution of CO_2 at approximately 600°C, which was assignable to the combustion of graphitic carbon.[20] Contrarily, the Ni_3Ga/CeO_2 catalyst exhibited minimal coke combustion around 350°C, which was ascribed to the facile combustion of amorphous carbon and/or the partial oxidation of Ga species in Ni_3Ga. Overall, these findings indicated that the formation of the intermetallic Ni_3Ga phase significantly inhibited coke formation and accumulation, which was consistent with the high stability of the DRB (Figure 3.14).

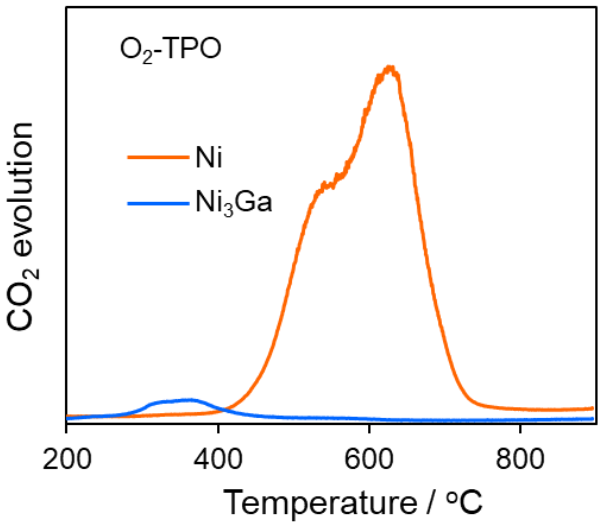

Figure 3.15. O_2-TPO profiles of spent Ni_3Ga/CeO_2 and Ni/CeO_2 in the DRB.

3.4 Conclusion

In summary, we prepared a Ni_3Ga/CeO_2 catalyst that is effective for the DRB. The XAFS analysis revealed that the intermetallic Ni_3Ga phase was formed on the CeO_2 support. Alloying Ni with Ga inhibited coke accumulation and significantly enhanced CO_2 utilization. Notably, the CO_2 conversion of Ni_3Ga was two-fold that of the monometallic Ni catalyst, which might be attributed to the synergetic effect of higher CO_2 adsorption or activation of Ni–Ga alloy and CeO_2 support. The study findings provide insight into material design in the CO_2 utilization of hydrocarbon conversion.

Reference

1. Velty, A.; Corma, A., Advanced zeolite and ordered mesoporous silica-based catalysts for the conversion of CO_2 to chemicals and fuels. *Chem. Soc. Rev.,* **2023**,*52*, 1773-1946.

2. Aresta, M.; Dibenedetto, A.; Angelini, A., The changing paradigm in CO_2 utilization. *J. CO_2 Util.,* **2013**, *3-4*, 65-73.

3. Xing, F.; Furukawa, S., Metallic Catalysts for Oxidative Dehydrogenation of Propane Using CO_2. *Chem. Eur. J.,* **2023**, *29*, e202202173.

4. Zhu, Q.; Zhou, H.; Wang, L.; Wang, L.; Wang, C.; Wang, H.; Fang, W.; He, M.; Wu, Q.; Xiao, F.-S., Enhanced CO_2 utilization in dry reforming of methane achieved through nickel-mediated hydrogen spillover in zeolite crystals. *Nat. Catal.,* **2022**, *5*, 1030-1037.

5. Nam, H.; Wang, Z.; Shanmugam, S. R.; Adhikari, S.; Abdoulmoumine, N., Chemical looping dry reforming of benzene as a gasification tar model compound with Ni- and Fe-based oxygen carriers in a fluidized bed reactor. *Int. J. Hydro. Energy,* **2018**, *43*, 18790-18800.

6. **2014**. De Caprariis, B., Bassano, C., Deiana, P., Palma, V., Petrullo, A., Scarsella, M., & De Filippis, P. Carbon dioxide reforming of Tar during biomass gasification. *Chem. Eng. Trans.,* **2014**, *37*, 97-102.

7. Simell, P. A.; Hakala, N. A. K.; Haario, H. E.; Krause, A. O. I., Catalytic Decomposition of Gasification Gas Tar with Benzene as the Model Compound. *Ind. Eng. Chem.,* **1997**, *36*, 42-51.

8. Wang, Y.; Yao, L.; Wang, Y.; Wang, S.; Zhao, Q.; Mao, D.; Hu, C., Low-Temperature Catalytic CO_2 Dry Reforming of Methane on Ni-Si/ZrO_2 Catalyst. *ACS Catal.* **2018,** 8, 6495-6506.

9. Wang, Y. L.; Hu, P.; Yang, J.; Zhu, Y. A.; Chen, C., C-H bond activation in light alkanes: a theoretical perspective. *Chem. Soc. Rev.* **2021,** *50*, 4299-4358.

10. Torrez-Herrera, J. J.; Korili, S. A.; Gil, A., Recent progress in the application of Ni-based catalysts for the dry reforming of methane. *Catal. Rev.* **2021**, 1-58.

11. Kawi, S.; Kathiraser, Y.; Ni, J.; Oemar, U.; Li, Z. W.; Saw, E. T., Progress in Synthesis of Highly Active and Stable Nickel-Based Catalysts for Carbon Dioxide Reforming of Methane. *Chemsuschem* **2015,** *8*, 3556-3575.

12. Liu, K.; Xing, F.; Xiao, Y.; Yan, N.; Shimizu, K.-i.; Furukawa, S., Development of a Highly Stable Ternary Alloy Catalyst for Dry Reforming of Methane. *ACS Catal.* **2023**, 3541-3548.

13. Liu, W.; Li, L.; Lin, S.; Luo, Y.; Bao, Z.; Mao, Y.; Li, K.; Wu, D.; Peng, H., Confined Ni-In intermetallic alloy nanocatalyst with excellent coking resistance for methane dry reforming. *J. Energy Chem.* **2022,** *65*, 34-47.

14. Joo, S.; Kim, K.; Kwon, O.; Oh, J.; Kim, H. J.; Zhang, L.; Zhou, J.; Wang, J. Q.; Jeong, H. Y.; Han, J. W.; Kim, G., Enhancing Thermocatalytic Activities by Upshifting the d-Band Center of Exsolved Co-Ni-Fe Ternary Alloy Nanoparticles for the Dry Reforming of Methane. *Angew. Chem. Int. Ed.,* **2021**, *60*, 15912.

15. Nakaya, Y.; Furukawa, S., Catalysis of Alloys: Classification, Principles, and Design for a Variety of Materials and Reactions. *Chem. Rev.* **2023**, *123, 9*, 5859–5947.

16. Furukawa, S.; Komatsu, T.; Shimizu, K.-i., Catalyst design concept based on a variety of alloy materials: a personal account and relevant studies. *J. Mater. Chem. A,* **2020**, *8*, 15620-15645.

17. Furukawa, S.; Komatsu, T., Intermetallic Compounds: Promising Inorganic Materials for Well-Structured and Electronically Modified Reaction Environments for Efficient Catalysis. *ACS Catal.* **2016,** *7*, 735-765.

18. Xing, F. L.; Nakaya, Y.; Yasumura, S.; Shimizu, K.; Furukawa, S., Ternary platinum-cobalt-indium nanoalloy on ceria as a highly efficient catalyst for the oxidative dehydrogenation of propane using CO_2. *Nature Catal.* **2022,** *5*, 55-65.

19. Xing, F.; Ma, J.; Shimizu, K.-i.; Furukawa, S., High-entropy intermetallics on ceria as efficient catalysts for the oxidative dehydrogenation of propane using CO_2. *Nature Commun.* **2022,** *13*, 5065.

20. Argyle, M.; Bartholomew, C., Heterogeneous Catalyst Deactivation and Regeneration: A Review. *Catalysts,* **2015,** *5*, 145-269.

Chapter 4

General Conclusions

4 General Conclusions

In this research, I targeted the effective utilization of CO_2 by dry reforming of hydrocarbons based on multimetallic catalysts. Alloying Ni and other metals remarkably enhanced the reactant conversion and stability in various dry reforming reactions, such as dry reforming of methane and dry reforming of benzene. Moreover, the structure of catalysts and mechanism study were further explored by characterization technique and experimental analysis.

Chapter 2 concludes that an innovative catalyst design concept based on a pseudo-binary alloy structure enables the development of a highly efficient and outstandingly stable catalyst for CO_2 reforming of methane. $(Ni_{0.5}Co_{0.5})_3Ge/SiO_2$, in which a part of Ni atoms of intermetallic Ni_3Ge was substituted with Co without changing the parent Ni_3Ge structure, exhibited a remarkably high coke resistance, an outstandingly long catalyst life (1000 h) at 700 °C even below the equilibrium conversion (many previous studies were done at equilibrium conversions; therefore, there remains a possibility that deactivation may have not appeared in conversion due to excess activity). Additionally, the used catalyst could be easily regenerated by a simple and soft oxidation procedure and the initial conversion in the second run was completely recovered in the third run. Alloying Ni with Ge not only inhibits carbon formation, but also promotes CO formation via the CHO intermediate pathway that involves no carbon formation. The dopant Co acts as an efficient site for CO_2 adsorption and activation, which supplies more oxygen atoms to promote carbon combustion. The combination of Ge and Co allows to minimize the coke accumulation, thus achieving outstandingly high stability for long-term operation. Therefore, $(Ni_{0.5}Co_{0.5})_3Ge/SiO_2$ catalyst showed a sufficiently high catalytic activity, coke resistance, and renewability in CO_2 reforming of methane reaction.

Chapter 3 summarizes a binary intermetallic Ni_3Ga supported on CeO_2 works as an effective catalyst for CO_2-assisted dry reforming of benzene (DRB: $C_6H_6 + 6CO_2 \rightarrow 3H_2 +$

12CO), which has great potential for the purpose of reducing as much CO_2 as possible. The CO_2 reforming of methane consumes a limited amount of CO_2 because of its stoichiometric ratio, whereas the CO_2 reforming of benzene could consume up to 6 mol of CO_2 with only 1 mol of benzene. Moreover, aromatic compounds including benzene can be supplied from the degradation of bio-derived lignin. The Ni_3Ga/CeO_2 catalyst exhibited significantly enhanced CO_2 utilization ability and product yield. Notably, the CO_2 conversion was two-fold that of the corresponding monometallic catalyst, which might be attributed to the synergetic effect of higher CO_2 adsorption or activation of Ni–Ga alloy and CeO_2 support. The combination of high-angle annular dark-field scanning transmission microscopy and X-ray absorption fine structure analysis confirmed the formation of the Ni_3Ga intermetallic structure. Moreover, Ga plays a crucial role in improving catalytic activity and minimizing coke formation.

In conclusion, our research not only demonstrates excellent catalytic performance of multi-metallic Ni-based catalysts in CO_2 conversion, but also offers a new perspective to prolong their lifespan. The findings of this study contribute to advancing the goal of carbon-neutralization in current industrial processes.

Acknowledgments

This wonderful opportunity as PhD candidate to study in Institute for Catalysis, Hokkaido University and the completion of the works presented in this thesis would not have been possible without countless contributions from my excellent supervisors, fellow lab mates, friends and my family during these three years.

As the very first heartfelt expression, I sincerely want to express my gratitude to my supervisor Professor Shinya Furukawa. His excellent knowledge of catalysis and his attitude and spirit towards scientific exploration have deeply affected me. Under his patient guidance, I've not only gained knowledge about metallic alloy catalysts, but also developed the ability to think independently and analyze problems critically. Moreover, he has also provided me with immense encouragement in daily matters, particularly during the period of two surgeries and recovery. His comforting words and care deeply moved me. I could say that he is the best supervisor I have encountered thus far.

Then I would like to express my deep appreciation to my master's supervisors Prof. Fengyu Zhao and Prof. Masahiko Arai in Changchun Institute of Applied Chemistry Chinese Academy of Science. I wouldn't have been able to get the study opportunity so smoothly in Hokkaido University without their guidance and recommendation. Furthermore, I am also very appreciative of Prof. Ken-ichi Shimizu for giving me the chance to study in his lab, and my DX program's mentor Professor Takashi Toyao for his helping in daily experiments. Besides, I would also like to be thankful for the Advance Graduate School and DX Doctoral Fellowship of Hokkaido University for providing the precious opportunity and financial support during the doctoral period.

Moreover, I've never forgot the wonderful memories and help from these guys: Jianshuo Zhang, Feilong Xing, Ham-san, Mengwen Huang, Chenxi He, Nakaya, Fangyi Yao and

Xiangyang Wu....Thank you so much for your understanding and companionship to get through all the ups and downs in these three years.

Last, but not least, nothing can express my deepest gratitude to my beloved family. They always give me full emotional and financial support, always allowing me to pursue my dreams and passions without any worries. Thank you so much!

Finally, Thanks for every amazing landscape (sea and snow) and each person I've encountered in Hokkaido, letting me have so many wonderful memories and colorful life for three years. I love Hokkaido!

Liu Ke

刘 可